

行政院國家科學委員會補助專題研究計畫 ☒ 成果報告  
☐ 期中進度報告

部分稜形網格時域電磁分析法

FDTD Method with Partial Prism-Grid

計畫類別：☒ 個別型計畫 ☐ 整合型計畫

計畫編號：NSC 89-2213-E-002-025-

NSC 89-2213-E-002-197-

✓ NSC 90-2213-E-002-037-

執行期間： 88 年 8 月 1 日至 91 年 7 月 31 日

計畫主持人：吳瑞北

計畫參與人員：龐一心、吳俊德、林聖謀、林庭輝、宋永企、黃定彝、  
蔡俊任、季君炎、張恆嘉、薛光華、劉禮尚、王士瑋、劉建宏

成果報告類型(依經費核定清單規定繳交)：☐ 精簡報告 ☒ 完整報告

本成果報告包括以下應繳交之附件：

☐ 赴國外出差或研習心得報告一份

☐ 赴大陸地區出差或研習心得報告一份

☒ 出席國際學術會議心得報告及發表之論文各一份

☐ 國際合作研究計畫國外研究報告書一份

處理方式：除產學合作研究計畫、提升產業技術及人才培育研究計畫、  
列管計畫及下列情形者外，得立即公開查詢

☐ 涉及專利或其他智慧財產權，☐ 一年☐ 二年後可公開查詢

執行單位：國立台灣大學電信工程學研究所

中 華 民 國 九 十 二 年 一 月 十 四 日

# Contents

<b>Chapter 1</b>	<b>Introduction</b>	<b>1</b>
1.1	Research Motives and Literature Survey .....	1
1.2	Chapter Outlines.....	3
<b>Chapter 2</b>	<b>FDTD Method with Partially Prism-Gridded FEM</b>	<b>5</b>
2.1	Introduction .....	5
2.2	Prism-Gridded FEM.....	7
2.3	Computational Aspects.....	10
2.4	Numerical Results .....	13
2.5	Summary .....	15
<b>Chapter 3</b>	<b>A Novel Finite Element Basis Capable of Eliminating Late-Time Instability</b>	<b>25</b>
3.1	Introduction .....	25
3.2	A Novel Finite-Element Basis.....	26
3.3	Numerical Results .....	28
3.4	Summary .....	28
<b>Chapter 4</b>	<b>Thin-Slot Formalism</b>	<b>33</b>

4.1	Introduction .....	33
4.2	Unified Thin-Slot Formalism .....	34
4.3	Field Distribution by Conformal Mapping .....	35
4.4	Numerical Results .....	37
4.5	Summary .....	39

## **Chapter 5 Composite Effects of Reflections and Ground Bounce**

### **for Signal Line through a Split Power Plane 46**

5.1	Introduction .....	46
5.2	Theory and Circuit Modeling.....	47
5.3	Numerical Simulation .....	49
5.4	Experimental Validation.....	49
5.5	Summary .....	52

## **Chapter 6 Hybrid TIE/FDTD Method for Open Boundary**

### **Coupling between Isolation Islands 64**

6.1	Introduction .....	64
6.2	Hybrid TIE/FDTD Method .....	65
6.3	Numerical Example.....	71
6.4	Experimental Validation.....	72
6.5	Summary .....	73

<b>Chapter 7</b>	<b>Visualization for Simulation Results</b>	<b>82</b>
7.1	Introduction .....	82
7.2	Web-Based Visualization System.....	82
7.3	Visualization with Commercial Software .....	84
7.4	Summary .....	84
<b>Chapter 8</b>	<b>Conclusions</b>	<b>101</b>
	<b>References</b>	<b>103</b>
<b>Appendix A.</b>	<b>Publications Supported under this Project</b>	<b>A-1</b>
<b>Appendix B.</b>	<b>Conference Paper</b>	<b>B-1</b>
<b>Appendix C.</b>	<b>Conference Report</b>	<b>C-1</b>



## List of Figures

Fig. 2.1	(a) Geometry of microstrip with grounded via and (b) the mesh division near and under the grounded via. ....	17
Fig. 2.2	The prism element and the assignment of unknown fields. ....	18
Fig. 2.3	Transmission coefficient along a microstrip with grounded via. Comparison between present method and other numerical methods. The microstrip is of width 2.3 mm and height 0.8 mm, the via diameter is 0.6 mm, and the substrate is of dielectric constant 2.32. The solution region is basically divided into $110 \times 70 \times 30$ cells ( $\Delta_x = 0.1$ mm, $\Delta_t = 0.167$ ps) with 8 perfectly matched layers.....	19
Fig. 2.4	Scattering parameters of a through hole via. Comparison between the simulated results with the measured data. The microstrip is of width 1.6 mm and height 3.3 mm, the diameters of the rod and the clearance hole are 1.5 and 3.9 mm respectively, and the substrate is of dielectric constant 3.4. The simulation region is basically divided into $70 \times 80 \times 48$ cells with $\Delta_x = \Delta_y = 0.206$ mm, $\Delta_z = 0.4$ mm, and $\Delta_t = 0.333$ ps.....	20
Fig. 2.5	Calculated scattering parameters of a through hole via with connecting angle $\theta = 0^\circ$ , $90^\circ$ , and $180^\circ$ as a parameter. The microstrip is of width 0.254 mm and height 0.239 mm, the diameters of the via and clearance hole are 0.254 mm and 0.508 mm, respectively, and the substrate is of dielectric constant 4.3. The solution region is basically	

	divided into $86 \times 56 \times 48$ cells with $\Delta_x = \Delta_y = 0.02117$ mm, $\Delta_z = 0.05959$ mm, and $\Delta_t = 0.0353$ ps.....	21
Fig. 2.6	Scattering parameters versus the connecting angle $\theta$ with the frequency= 20 GHz and 60 GHz. All other structural parameters are the same as those in Fig. 2.5.....	22
Fig. 2.7	Scattering parameters versus the diameter ratio of via to hole at frequency= 20 GHz. All other structural parameters are the same as those in Fig. 2.5.....	23
Fig. 2.8	(a) Layout of a CPW to CPS transition (b) Comparison of the calculated $ S_{11} $ and $ S_{21} $ with measured data. The substrate is of height 25 mil and dielectric constant 9.8.....	24
Fig. 3.1	A novel finite element basis for hybrid FE/FDTD method. (a) pulse basis for electric field, and (b) vector basis $\vec{W}_1(\vec{r})$ for magnetic field....	30
Fig. 3.2	(a) Applying Ampere's law for the electric field at node $\vec{r}_i$ and (b) the integral inside an element.....	30
Fig. 3.3	Mesh in the interface region.....	31
Fig. 3.4	The total field at the cylinder center due to a Gaussian TM wave incident from $-x$ direction.....	31
Fig. 3.5	Comparison of the late-time response by conventional FEM linear basis and the present basis.....	32
Fig. 4.1	A typical FDTD mesh with cell size larger than the width of slot.....	41
Fig. 4.2	Conformal mapping of a slot-line into semi-infinite parallel planes. ....	41
Fig. 4.3	Effective permittivity $\epsilon_r(k)$ of different methods verses the $s/\Delta$ ratio.....	42

Fig. 4.4	Calculated results for the characteristic impedance of CPS versus $s/\Delta$ for the slotline shown in the inset. ....	43
Fig. 4.5	Calculated results for the real and imaginary parts of $Z_0$ versus frequency by the present TSF for the case of $s = 0.5\Delta$ . Also shown for comparison are the results obtained by traditional FDTD with the slot divided into 2, 4, and 6 cells, respectively. ....	44
Fig. 4.6	Calculated results for the characteristic impedance $Z_0$ versus $s/w$ for the coplanar waveguide shown in the inset. ....	45
Fig. 5.1	A simple multi-layered structure with split power plane. ....	53
Fig. 5.2	Equivalent circuits at cross-junction for (a) microstrip line and (b) slotline. ....	54
Fig. 5.3	FDTD mesh inclusive of slotline. Here, $E_z(i, j)$ is a short-hand notation for $E_z(i\Delta_x, i\Delta_y, t)$ and similarly for $H_x, H_y$ , and $H_z$ . ....	55
Fig. 5.4	Top view of Fig. 5.1. ....	56
Fig. 5.5	Voltages at A, B on microstrip line (upper figure), and voltages at a, b, c on slotline (middle figure), and ground bounce near slotline (lower figure). ....	57
Fig. 5.6	Comparison of voltage at A with different separation of power/ground planes as a parameter. ....	58
Fig. 5.7	A test PCB used for experiment and simulation to depict the slot-induced ground bounce: (a) top view and (b) side view. ....	59
Fig. 5.8	Measured and simulated waveforms of the TDR signal on port 1 and TDT signals on port 2 for the test setup in Fig. 5.7. ....	60
Fig. 5.9	Power spectral of the input signal, and the simulated and measured output signals. ....	61

Fig. 5.10	$S_{21}$ of the simulation and measurement. The measurement is done by HP8510C. ....	62
Fig. 5.11	Simulation results of TDT signals on port 2 versus the different widths of slot. ....	63
Fig. 6.1	A typical PCB structures with separated poser islands. (a) Original problem, (b) interior open-circuit problem, and (c) exterior-short circuit problem. ....	74
Fig. 6.2	Equivalent LC network for interior problem. ....	75
Fig. 6.3	Equivalent magnetic current source and resultant electromagnetic field for exterior problem. ....	75
Fig. 6.4	(a) Grid meshing for the structure and node voltage $V(\bar{s}_j)$ , (b) roof-top basis for magnetic current, and (c) pulse basis for magnetic flux across the aperture. ....	76
Fig. 6.5	Equivalent circuit for updating the node voltage at boundary. ....	77
Fig. 6.6	A patch antenna of infinite ground plane used for simulation. ....	77
Fig. 6.7	simulated results for $S_{11}$ by the present method and a frequency domain full wave solver IE3D. ....	78
Fig. 6.8	A test PCB of isolation power plane used for experiment and simulation. (a) Top view, (b) side view, and (c) thickness of the substrate and metal plane. ....	79
Fig. 6.9	Measured and simulated waveforms of (a) TDR signal at port 1 and (b) TDT signal at port 2. ....	80
Fig. 6.10	Power spectrum density of TDT signal. Comparisons among measurement, the present method, and IE3D. ....	81
Fig. 7.1	The web-based visualization system. ....	85

Fig. 7.2	The visualization region for dielectric circular cylinder. ....	86
Fig. 7.3	(a) The $E_z$ field surface plot and (b) the H field vector plot at time step 100. ....	87
Fig. 7.4	(a) The $E_z$ field surface plot and (b) the H field vector plot at time step 160. ....	88
Fig. 7.5	(a) The $E_z$ field surface plot and (b) the H field vector plot at time step 200. ....	89
Fig. 7.6	(a) The $E_z$ field surface plot and (b) the H field vector plot at time step 240. ....	90
Fig. 7.7	(a) The $E_z$ field surface plot and (b) the H field vector plot at time step 280. ....	91
Fig. 7.8	(a) The $E_z$ field surface plot and (b) the H field vector plot at time step 320. ....	92
Fig. 7.9	(a) The $E_z$ field surface plot and (b) the H field vector plot at time step 360. ....	93
Fig. 7.10	Isolation islands used for visualization. ....	94
Fig. 7.11	(a) The $E_z$ field surface plot and (b) contour plot at time step 100. ....	95
Fig. 7.12	(a) The $E_z$ field surface plot and (b) contour plot at time step 150. ....	96
Fig. 7.13	(a) The $E_z$ field surface plot and (b) contour plot at time step 200. ....	97
Fig. 7.14	(a) The $E_z$ field surface plot and (b) contour plot at time step 250. ....	98
Fig. 7.15	(a) The $E_z$ field surface plot and (b) contour plot at time step 300. ....	99
Fig. 7.16	(a) The $E_z$ field surface plot and (b) contour plot at time step 500. ....	100

## List of Tables

Table 2.1	Comparison of the computation time and memory between present method and conventional FDTD method.....	16
Table 4.1	The effective permittivity $\epsilon_r(k)$ for capacitive TSF [15], uniform TSF [16], enhanced TSF [18], and the present TSF, where $K[\cdot]$ is the complete elliptic integr defined as $K[m] = \int_0^1 \frac{1}{(1-t^2)(1-mt^2)} dt$ .....	40

## 計畫中文摘要：

關鍵詞：時域有限差分法、有限元素法、平面電路、遲時不穩定、訊號完整度

本計畫旨在開發新穎的時域電磁分析方法，可以處理微波積體電路常用的平面結構。首先結合有限元素法與有限時域差分法，建立部分稜形網格的時域電磁分析，其應用包括含有柱狀貫孔接地的微帶線結構，以及共面波導和共面帶線間的轉接結構。另外也發展出新的有限元素法基底函數來處理數值穩定度的問題，以及將建立以網際網路為基礎的時域電磁計算環境。

本計畫也探討時域有限差分法於高速電子電路之全波效應的應用。針對多層印刷電路板常見的槽線結構，首先發展出槽線公式來降低時域分析法中所須切割的網格數量。新的槽線公式運用了保角映像的技術，解出槽線附近的電磁場分佈，再以等效的介電係數與導磁係數代入時域有限差分法中。運用此公式可以模擬含有細微槽線的問題，即使網格尺寸大於槽線寬度，也不須再加以細分，報告中以槽線結構作為分析的例子，顯示此法的有效性與正確性。接著建立開槽的等效電路公式，可以結合二維時域有限差分法，快速且有效分析含有開槽電磁效應的訊號完整度問題。應用此法模擬多層電路板間開槽激發的彈地雜訊，並與實驗結果做驗證。最後結合二維時域有限差分法和時域積分方程，分析兩孤立平面電路間的電磁輻射耦合效應，並以視覺化方式呈現其耦合機制。

## ***Abstract***

Keywords: Finite-Difference Time-Domain Method, Finite Element Method, Planar Circuits, Late-Time Instability, Signal Integrity

This project aims at developing a novel time domain electromagnetic simulation technique which is very suitable for planar circuits commonly used in microwave integrated circuits. A finite-difference time-domain (FDTD) method with partial prism-grid is proposed. In this method, the prism grid is employed to model irregular regions and is handled by the finite element method (FEM), while the rectangular grid is employed to model regular regions and is solved by the conventional FDTD method. The applications include via interconnections, and the transition between coplanar waveguide and coplanar strip. We also develop a new FEM basis to deal with the late-time stability problems usually happened in the hybrid time domain methods. In addition, a web-based electromagnetic problems solving environment has been established, in which remote supercomputers as the computing engine and local personal computer as the graphical client are incorporated.

The application of FDTD method on solving the full-wave effects of high-speed circuits is also investigated. Focusing on the slot/aperture structures usually encountered in the multi-layered printed circuit board, we first derived an improved thin-slot formalism to alleviate the gridding of the FDTD solution for electromagnetic problems involving narrow slots. By applying the conformal mapping technique, the varying field distribution near the slots is analytically derived and fully cast into a unit FDTD cell with effective permittivity and permeability. As a result, this formalism permits narrow slots to be modeled without reducing spatial grid size, even when the slot gap width is much smaller than one space grid. Typical examples, such as slotlines and coplanar waveguides, are analyzed as illustrations. Hybridization of equivalent circuit equations with two-dimensional FDTD method is then proposed to effectively deal with signal integrity problems due to the electromagnetic effects of slots. The ground bounce for signal line through a split power plane is simulated by this approach and compared with the measure results. Finally, a method that combines two-dimensional FDTD and time-domain integral equation formulation is developed to analyze the radiation coupling between two isolation islands. Visualization of the coupling mechanism has also been demonstrated.



# Chapter 1

## Introduction

### 1.1 Research Motives and Literature Survey

The finite-difference time-domain (FDTD) method was proposed by Yee in 1966 [1]. It has been widely applied in various electromagnetic problems and has become one of the most popular numerical methods in electromagnetic applications [2]. In addition to the large memory storage, one major difficulty of the FDTD method is its inefficiency in modeling the structures with arbitrarily curved boundary. To obtain numerical results with second order accuracy, structures are modeled with the uniformly rectangular mesh, and the central difference approximation is applied [1]. Therefore the FDTD method works excellently only for structures which can fit well into Cartesian coordinates in its original form. Even if the structures are basically of rectangular shape, the various geometric dimensions for design make it difficult to model the whole structures with a uniformly rectangular mesh.

Several schemes have been proposed to improve the modeling of structures for FDTD method since 1983 [3], such as curvilinear coordinate system [3], contour path method [4], [5], subgridded method [6], [7], and local nonorthogonal grid method [8]. However, they may suffer from the massive iteration loops or the degradation of accuracy. Besides, the hexahedral mesh adopted is inefficient in modeling some practical structures, such as sharp corners. Recently, we have proposed an extended FDTD method to solve the electromagnetic scattering of two or three-dimensional arbitrarily shaped dielectric objects [9], [10]. It successfully employs the conventional FDTD method for most of the rectangular region but introduces the tetrahedral edge-based finite-element time-domain (FETD) scheme to model the region near the curved boundaries. This hybrid finite-element/finite-difference time-domain (FE/FDTD) method preserves the second order of numerical accuracy without much computational complexity, and can be theoretically applied to deal with arbitrarily shaped electromagnetic structures with great flexibility.

For most microwave circuits, the structures can be longitudinally divided into several building layers inside which the material and conductors can be of arbitrary shape in the transverse directions. It is reasonable that we only need to call for triangular mesh near the curved boundary in the transverse directions while remaining

rectangular grid in the longitudinal direction. The integral form of Maxwell's equations can then be adopted in the numerical computation [11]. The hybrid FE/FDTD method can also be used to deal with this kind of electromagnetic problems for better numerical accuracy. It has been successfully employed in two-dimensional scattering problems [9], but need to be improved for planar circuits problems.

Several hybrid methods in time domain suffer from the numerical instability [8]. It makes the numerical results divergent in the late-time simulation and needs to be carefully dealt with. The late-time instability is usually alleviated by some average schemes in time or in space domain along with the degradation of the resultant accuracy [8], [12]-[14]. The reason and mechanism of the instability should be identified and some better remedy should be exploited to suppress it.

The other difficulty encountered in FDTD method is in modeling thin structures, such as narrow slots. The increase in gridding for better simulation accuracy will exhaust the computer memory and consume intolerable CPU time. An efficient way to circumvent this problem is to specially approximate the field around the slot and incorporate it into FDTD algorithm elsewhere. Depending on how the field distribution near the slot is assumed, several thin-slot formalisms (TSF) have been proposed, such as the capacitive TST [15], the uniform TSF [16], the hybrid TSF [17], and the enhanced TSF [18]. These methods, however, are either too simple to obtain sufficient accuracy, or too complicated to formulate. A simpler and more accurate approach must be developed.

The presence of narrow slots is common to modern printed circuit boards (PCBs). For example, cutting a power plane into several areas provides multiple power distribution. Another is isolated power or ground plane areas, called voltage islands, to isolate a noisy or sensitive circuit from others [19]. However, signal lines have to cross the slots in order to communicate between different areas. The presence of slots significantly disturbs the return current path [20]. Simple equivalent circuit model was proposed to simulate the mode conversion mechanism between microstrip line mode and the slot line mode [21]. In multi-layer structures, the signal crossing the slot will excite the parallel plate modes which exhibit as ground bounce between the power and ground planes. Mode conversion happens among microstrip mode, slotline mode, and the parallel plate mode. However, it cannot be accurately modeled by circuit simulators.

In reality, the power and ground planes in PCBs must be finite in size. The edges of the finite-size plate will not only cause signal reflection but also radiation. It can serve as a source of electromagnetic interference (EMI) as well as a receptor. For structures with isolated power islands, the coupling among the edges may become a major source of noise and should be taken into account.

The complicated mechanism of mode conversion among discontinuities of vias, slots in split plane, and edges of the finite-size plates, has been investigated using the three-dimensional FDTD method [22]-[24]. However, the packaging structures usually include elements of drastically different scales, say, the microstrip and slotline are usually very narrow as compared with the parallel plate. The FDTD method is usually incapable of accurately modeling the structure details and if so, will need long computation time and large computer memory. To accurately analyze the mode conversion mechanism, a more efficient approach should be exploited.

## 1.2 Chapter Outlines

Following this introductory chapter, in Chapter 2, the novel hybrid FE/FDTD for layered structures with arbitrarily curved boundary in the transverse direction is mentioned. The present scheme is applied to deal with problems of via interconnections and planar circuit transition, demonstrating its flexibility and efficiency. The accuracy is also verified by comparing the calculated results with those by other methods or experiments.

The numerical instability in late-time simulation encountered in hybrid FE/FDTD method is studied in Chapter 3. A detailed check reveals that this instability may be due to the non-perfect match between the bases employed in the FEM and FDTD methods. A novel finite-element basis function compatible with the uniform basis in FDTD is therefore devised and successfully applied to a two-dimensional scattering problem of a dielectric cylinder.

In Chapter 4, an improved expression of the thin-slot formalism by conformal mapping technique is proposed to alleviate the gridding of the FDTD solution for electromagnetic problems involving narrow slots. The characteristic impedance of the coplanar strip and coplanar waveguide are calculated by this formalism. The numerical results will demonstrate that this formalism is superior to other methods in dealing with structures including thin slots.

An experimental setup is devised in Chapter 5 to demonstrate the significant coupling between signal lines due to the slots cut on the power/ground planes in a planar circuit board. In addition, a two-dimensional FDTD method combined with transmission lines model is developed to solve this problem.

To take into account radiation effects due to the edges of the finite-size power/ground planes, a novel method that combines two-dimensional FDTD and integral equation formulation is proposed in Chapter 6. The coupling effects of two isolation power islands are analyzed and measured for the verification of this hybrid method.

In Chapter 7, the employment of visualization systems for numerical results is introduced. Then, the real time visualization of electromagnetic fields is demonstrated for some simulation results.

Finally, some conclusions are drawn in Chapter 8.

## Chapter 2

### FDTD Method with Partially Prism-Gridded FEM

#### 2.1 Introduction

Several attempts have been proposed for FDTD method to deal with the structures with arbitrarily curved surfaces, such as curvilinear coordinate system [3], contour path method [4], [5], subgridded method [6], [7], and local nonorthogonal grid method [8]. Curvilinear coordinate system globally models the structure of interest [3]. As compared with the original FDTD, the scheme requires additional memory to store the coordinates and spends significant computation time in updating the field, even in most of the required region. An improved scheme is to employ the locally conformed scheme so as to preserve the advantages of conventional FDTD as much as possible [4], [5]. Relying on the integral form of Maxwell's equations, both schemes suffer from worse accuracy due to a larger discretization error of first order. In addition, special attention should be paid so as not to make the algorithm unstable. Following the same approach, a generalized Yee algorithm is recently proposed to deal with planar circuits [11], but suffering from similar discrepancy.

The subgridding method which divides the whole solution region into several orthogonal-gridded regions with different cell sizes has the advantages of improved accuracy without sacrificing computational efficiency [6], [7]. In these schemes, fields are calculated with central finite-difference formulas and interpolated on the boundaries between different regions. Basically relying on rectangular grid, the approach may require massive small cubic cells to model arbitrary boundary or else, suffer from staircasing approximation. The small cells call for a proportionally short time division for the stability consideration. In addition, the interpolation along region boundary may degrade the accuracy of the results.

To have a closer fit to the curved boundary, some define local nonorthogonal grid near the curved surfaces and transfer the fields back and forth in the overlapping region by interpolation [8], [25]. Based on the volume integral equation in nonorthogonal regions, a better approximation for surface integration of fields is also incorporated to improve the accuracy of the results. Another special approach is to carefully choose a nonuniform rectangular mesh such that the curved boundary either coincides the mesh or intersects the mesh across the diagonal [26]. In case of metallic

boundary, it is possible to derive a modified formula for updating the magnetic field at the resultant triangular cell along the boundary. Usually, this approach involves several graded meshes and in which, shorter time step is required in order to comply with the stability criterion.

Recently, a very versatile and accurate extended FDTD method is proposed which employs the conventional FDTD method for most of the regular region and introduces the tetrahedral edge-based finite element method (FEM) to model the region near the curved surfaces [9], [10]. Numerical results of simulation validate that the method has the advantages of accuracy, flexibility, and computational efficiency.

For most microwave devices, such as planar circuits, waveguides with step transitions, and packaging interconnections, the structures can be longitudinally divided into several building layers inside which the material and conductors can be of arbitrary shape in the transverse directions. In the simplest case, such as microstrip or stripline structures with thin substrate, the problem can be approximated by a two-dimensional one. Some time domain methods capable of modeling the curved boundary have been proposed, e.g., [27], [28]. These methods employ conformal mesh near the curved boundary and derive special formulas for updating the field in the irregularly shaped cells. The solution schemes are explicit, but special care should be taken in mesh arrangement so as not to make algorithm unstable.

For most general multilayer cases, Righi et al. has proposed an approach which hybridizes TLM with the mode matching method for the enclosed region due to the housing [29]. Capable of modeling the housing region semi-analytically, the approach can be very efficient for some-layered structures, but fails to deal with curved boundary accurately and efficiently.

A novel FDTD method with partial prism-grid is proposed for the analysis of practical microwave and millimeter wave planar circuits. The method is featured by hybridizing the flexible prism-based finite element method to handle the region near the curved metallization boundary and the efficient rectangular-gridded FDTD method for most of the regular region. It can be used to deal with shielded or unshielded planar components such as patch antennas, filters, resonators, couplers, dividers, vias, and various transitions between planar transmission lines. Although only representative structures, e.g.; grounded via, and CPW to CPS transition, are analyzed in this chapter, the underlined formulation is applicable to layered structures with arbitrarily curved boundary in the transverse direction. The accuracy of this method is verified by comparing the calculated results with those by other methods. Also, by the analysis of computational complexity, the present method is shown to be as efficient as the conventional FDTD method, with negligible overhead in memory and computation time for handling the curved boundary.

## 2.2 Prism-Gridded FEM

### 2.2.1 Mesh division

Consider an illustrative example of a microstrip line with cylinder grounded via shown in Fig. 2.1(a). For conventional FDTD method, it is natural to employ a uniform grid in the  $z$ -direction, but the staircasing approximation involved in modeling the curved via boundary in the  $x, y$  plane may cause a significant error. A better remedy is to model the region near the via with triangular cells, while the regular FDTD grid elsewhere as shown in Fig. 2.1(b). Consequently, along the curved boundary there are four to five layers of prism cells formed by the triangular elements in the transverse plane together with the uniform grid in the  $z$  direction. Note that the region directly above the microstrip can be modeled by conventional FDTD with regular grid. The tangential electrical field at the surface of microstrip is zero and consequently the conflict of cell shape below and above the microstrip line causes no problems.

Fig. 2.2 shows the field discretization in a prism cell. The transverse components  $\vec{E}_\rho$  are located in the layers with integer  $\Delta_z$  coordinates while the longitudinal components  $E_z$  in the layers with half integer of  $\Delta_z$ . As a result, the electric field unknowns near the interface between the FEM and FDTD regions may coincide with each other exactly. No interpolation scheme need be employed when communicating between the FEM and FDTD solutions in the overlapping region.

### 2.2.2. Weak-form formulation in FEM region

Starting from the source-free Maxwell's two curl equations in a linear and isotropic region, the vector wave equation can be obtained as

$$\nabla \times \left( \frac{1}{\mu} \nabla \times \vec{E} \right) + \epsilon \frac{\partial^2 \vec{E}}{\partial t^2} = 0 \quad (2.1)$$

Applying the variational reaction theory [30], this equation can be cast into the weak form by taking inner product with an arbitrary testing field  $\vec{E}^a$  on one layer of the FEM region. To be more specific, choose a transversely polarized field  $\vec{E}_\rho^a$  in the  $z = k\Delta_z$  plane as the testing field. By performing integration by part and some algebraic simplifications, one may obtain

$$\int_A \left\{ \frac{1}{\mu} \nabla_\rho \times \vec{E}_\rho^a \cdot \nabla_\rho \times \vec{E}_\rho + \varepsilon \vec{E}_\rho^a \cdot \frac{\partial^2 \vec{E}_\rho}{\partial t^2} + \vec{E}_\rho^a \cdot \left[ \frac{\partial}{\partial z} \left( \frac{1}{\mu} \nabla_\rho E_z \right) - \frac{\partial}{\partial z} \left( \frac{1}{\mu} \frac{\partial \vec{E}_\rho}{\partial z} \right) \right] \right\} dS = 0 \quad (2.2a)$$

Here,  $\nabla_\rho \equiv \hat{x} \frac{\partial}{\partial x} + \hat{y} \frac{\partial}{\partial y}$  denotes the transverse del operator,  $\vec{E}_\rho$  the transverse components of the electric field, and  $E_z$  the z-component. Similarly, in the  $z = (k + \frac{1}{2})\Delta_z$  plane, one assures that the desired field should satisfy

$$\int_A \left\{ \frac{1}{\mu} \nabla_\rho E_z^a \cdot \nabla_\rho E_z + \varepsilon E_z^a \cdot \frac{\partial^2 E_z}{\partial t^2} - \frac{1}{\mu} \nabla_\rho E_z^a \cdot \frac{\partial \vec{E}_\rho}{\partial z} \right\} dS = 0 \quad (2.2b)$$

for arbitrary testing field  $E_z^a$ .

Note that (2.2a) calls for the derivative of  $E_z$  with respect to  $z$  in the  $k\Delta_z$  plane. This can be accurately approximated by using the central difference scheme which in the present case requires the  $E_z$  unknowns in the  $(k + \frac{1}{2})\Delta_z$  and  $(k - \frac{1}{2})\Delta_z$  planes.

Similarly, the term  $\frac{\partial \vec{E}_\rho}{\partial z}$  in (2.2b) requires the transverse unknowns  $\vec{E}_\rho$  in the  $k\Delta_z$  and  $(k + 1)\Delta_z$  planes.

### 2.2.3 Basis functions

The weak form (2.2) can be discretized into matrix forms by choosing suitable basis functions. Here, the cross-sectional area is subdivided into small triangular elements. The longitudinal component  $E_z$  inside an element is expressed by node-based interpolation functions, i.e.,

$$E_z(\vec{\rho})|_{z=(k+\frac{1}{2})\Delta_z} = \sum_{i=1}^3 \lambda_i(\vec{\rho}) e_{zi} = \{\lambda\}^T \{e_z\}_{k+\frac{1}{2}} \quad (2.3)$$

where  $\lambda_i(\vec{\rho})$ 's,  $i = 1, 2, 3$ , denote the three natural coordinates of the element, and

$e_{zi}$ 's the nodal unknowns. On the other hand, the transverse component  $\vec{E}_\rho$  is

expanded by



$$\vec{E}_\rho(\vec{\rho})\Big|_{z=k\Delta_z} = \sum_{i=1}^3 \vec{W}_i(\vec{\rho}) e_{\rho i} = \{\vec{W}\}^T \{e_\rho\}_k \quad (2.4)$$

where  $\vec{W}_i(\vec{\rho})$ 's are the edge-based Whitney functions [31] and  $e_{\rho i}$ 's the edge unknowns.

Taking integration with respect to the basis functions and applying the Ritz procedure, one may reduce (2.2) to two systems of coupled differential equations for transverse and longitudinal components. This is a normal FEM solution approach and can be referred to typical textbooks, e.g. [31].

#### 2.2.4 Matrix equations

The remaining term need to be discretized in (2.2) is the differentiation with respect to time. Based on the Crank-Nicolson scheme, we apply central finite difference method with respect to  $t$  variable and in addition take timing average for the first term in (2.2) to achieve unconditional stability [10]. The final time marching equations in the FEM region are

$$\begin{aligned} [G_{\rho\rho}^+] \{e_\rho\}_k^{n+1} &= 2[G_{\rho\rho}^-] \{e_\rho\}_k^n - [G_{\rho\rho}^+] \{e_\rho\}_k^{n-1} \\ &\quad - [C_{\rho z}] (\{e_z\}_{k+\frac{1}{2}}^n - \{e_z\}_{k-\frac{1}{2}}^n) \\ &\quad + [D_{\rho\rho}] (\{e_\rho\}_{k+1}^n - 2\{e_\rho\}_k^n + \{e_\rho\}_{k-1}^n) \end{aligned} \quad (2.5a)$$

and

$$\begin{aligned} [G_{zz}^+] \{e_z\}_{k+\frac{1}{2}}^{n+1} &= 2[G_{zz}^-] \{e_z\}_{k+\frac{1}{2}}^n - [G_{zz}^+] \{e_z\}_{k+\frac{1}{2}}^{n-1} \\ &\quad + [C_{\rho z}]^T (\{e_\rho\}_{k+1}^n - \{e_\rho\}_k^n) \end{aligned} \quad (2.5b)$$

in which

$$[G_{\rho\rho}^\pm] = \int_A \varepsilon_r \{\vec{W}\} \{\vec{W}\}^T dS \pm \frac{\kappa^2}{4} \int_A \frac{1}{\mu_r} \{\nabla_\rho \times \vec{W}\} \{\nabla_\rho \times \vec{W}\}^T dS \quad (2.6a)$$

$$[C_{\rho z}] = \kappa^2 \int_A \frac{1}{\mu_r} \{\vec{W}\} \{\nabla_\rho \lambda\}^T dS \quad (2.6b)$$

$$[D_{\rho\rho}] = \kappa^2 \int_A \frac{1}{\mu_r} \{\vec{W}\} \{\vec{W}\}^T dS \quad (2.6c)$$

$$[G_{zz}^\pm] = \int_A \varepsilon_r \{\lambda\} \{\lambda\}^T dS \pm \frac{\kappa^2}{4} \int_A \frac{1}{\mu_r} \{\nabla_\rho \lambda\} \{\nabla_\rho \lambda\}^T dS \quad (2.6d)$$

Here,  $\kappa = \frac{\Delta_t}{\sqrt{\mu_0 \epsilon_0} \Delta}$  is the stability factor, the superscript of  $\{e_\rho\}$  and  $\{e_z\}$  stands

for the time step while the subscript denotes the layer index in the z direction.

### 2.2.5 Discussion on computational efficiency

It is interesting to compare the computational load between the present method and the extended FDTD methods proposed in [10], [32] when applying for layered structures. For simplicity, consider the structure shown in Fig. 2.1(a). The region around the via is discretized into prism grids as shown in Fig. 2.1(b) and solved by the FEM. Note that the cross section of each layer is identical, hence the matrices depicted in (2.5) need be stored and preprocessed for one layer only during numerical simulation. Even for more general structures with several different kinds of layers, the memory requirement for the present method is much smaller than that for the other two extended FDTD methods.

As to the computation time, the present method which is based on the LU decomposition method as employed in [9] for each layer is superior to the extended method in [10] which is based on the conjugate gradient method. At each time step, the present method involves an efficient forward substitution followed by backward substitution. The operation count for each substitution equals the number of unknowns multiplied by the bandwidth of the matrices, which is estimated to be about 10 for most structures [9]. On the contrary, the other two extended FDTD methods which call for matrix solution for a 3D problem are much more time consuming. At each time step, there usually are quite a few iterations of matrix vector multiplication until convergence. Also it deserves mentioning that the number of unknowns involved in the present prism gridded mesh is about half of that in the tetrahedral gridded mesh since tetrahedral mesh will introduce additional unknowns [10]. This contributes much to the advantage of the present method.

## 2.3 Computational Aspects

### 2.3.1 Time marching scheme

Separate time domain analyses are employed for solving the Maxwell's equations in the FDTD and FEM regions. However, some hand shaking process is required to transfer back and forth the computed data for the interface of the two regions. The time marching scheme for the present method is similar to that described in [10], except that the electric fields in FEM region are computed by (2.5) layer by layer at each time step.

For example, to obtain the transverse electric field on  $k$  layer  $\{e_\rho\}_k$  at time step  $n + 1$  by (2.5a), one calls for the values on neighboring layers in previous two time steps as initial conditions, or more specifically,  $\{e_\rho\}_{k-1}$ ,  $\{e_\rho\}_k$ ,  $\{e_\rho\}_{k+1}$ ,  $\{e_z\}_{k-\frac{1}{2}}$ ,  $\{e_z\}_{k+\frac{1}{2}}$  at time step  $n$  and  $\{e_\rho\}_k$  at time step  $n - 1$ . In addition, one require the given transverse electric fields along the boundary of FEM region on the same layer at time step  $n + 1$  as the boundary conditions. These boundary conditions should be provided by the FDTD simulation in the FDTD region. Similarly, solution for the longitudinal electric field on  $k + \frac{1}{2}$  layer  $\{e_z\}_{k+\frac{1}{2}}$  at time step  $n + 1$  by (2.5b) requires  $\{e_z\}_{k+\frac{1}{2}}$ ,  $\{e_\rho\}_k$ ,  $\{e_\rho\}_{k+1}$  at time step  $n$  and  $\{e_z\}_{k+\frac{1}{2}}$  at time step  $n - 1$  as well as the given nodal values on the same layer at time step  $n + 1$  along the boundary of FEM region.

Once the interior fields in the FEM region are solved, the values on the contour next to the exterior boundary of FEM region can be passed to the FDTD region for the updating of the magnetic field at the next half time step. The electric fields in the FDTD region at time step  $n + 2$  can then be obtained and the whole time marching procedure continues.

### 2.3.2 Matrix solution

The unknown fields,  $\{e_\rho\}$  and  $\{e_z\}$ , in the FEM region need be solved by (2.5) implicitly at each time step. The matrices  $[G_{\rho\rho}^+]$  and  $[G_{zz}^+]$  keep the same while right-hand-side (rhs) vectors change versus time step. The Gaussian elimination method based on Cholesky LU decomposition [33] is especially advantageous for the present case of multiple rhs vectors. In the pre-processing, the matrices  $[G_{\rho\rho}^+]$  and  $[G_{zz}^+]$  are decomposed into multiplication of a lower triangular and an upper triangular matrices. The matrix decomposition is time consuming but requires to be executed once. Then the unknown fields at each time step can be obtained by forward and backward substitution, which is an explicit updating scheme like FDTD. The operation count for each unknown by either the forward or backward substitution is proportional to the bandwidth of the matrices. For the storage of the matrices, the skyline scheme of variable bandwidth is employed. In addition, the unknowns are renumbered appropriately by the Collin's algorithm [34] so as to reduce the largest

bandwidth.

### 2.3.3 Absorbing boundary condition

The present method can be applied to deal with both shielded and unshielded problems. In the shielded cases, where the PEC planes coincide with the top and bottom surfaces of FEM region, the Dirichlet boundary condition is employed without difficulty.

In the unshielded cases, some sorts of absorbing boundary conditions should be employed to reduce the wave reflection resulted from the artificial lattice truncation. For some examples, e.g., the grounded via structure shown in Fig. 2.1, the FEM region is bounded to a finite size in not only the transverse but also the  $z$  directions. As a result, all the exterior space is modeled by the conventionally FDTD and all the available absorbing boundary conditions can be directly resorted to. For other examples, the FEM region may be required to extend to the top and bottom layers where (2.5) are not applicable for lack of the fields in the next layers. Some absorbing boundary conditions may fail for the present case that the cell is not rectangular in the transverse directions. Nonetheless, other absorbing boundary conditions, e.g., the first-order Mur's scheme [35], which rely on a uniform division in the direction normal to the boundary can be employed. Additionally, on the boundary of the FDTD region elsewhere, the super-absorbing method [36] can be incorporated to further absorb the undesired reflections from the lattice truncation boundary.

### 2.3.4 Computational complexity

It is interesting to investigate the computational complexity of the additional FEM processing as compared with the conventional FDTD method. This can be treated as the overhead required by FEM in improving the solution accuracy. Take this example as an illustration. Choosing a smaller FDTD division size  $\Delta$  will increase the number of division  $N_\Delta$  in each direction. The total number of variables  $N$  and thus the required memory for FDTD in the regular region is in the cubic order of  $N_\Delta$ , or written as  $N = O(N_\Delta^3)$ . The number of divisions required to model the curved surface is proportional to  $N_\Delta$ , while that in the normal direction remains nearly invariant. As a result, the number of unknowns in FEM region is  $N_{fem} = O(N_\Delta^2)$ .

Arguably, the memory required for storing the matrices in (2.5) is comparatively small. One needs to store the matrix elements for one layer only. The memory requirement is roughly  $B \cdot N_\Delta$  where  $B$  is the average bandwidth and in this case remains nearly the same as  $N_\Delta$  increases. Therefore, the dominant part is the storage for the additional unknowns and the FEM overhead in memory is

$$O(1/N_{\Delta}) = O(N^{\frac{-1}{3}}).$$

As for the computation time, the present analysis additionally requires FEM pre-processing for the matrix setup and the matrix solution at each time marching step. The FEM pre-processing includes the house keeping management for mesh, element integration, matrix assembly, and the last but usually the most time-consuming matrix decomposition into the LU form. Since it need only be done once and with the largest operation count proportional to  $B^2 \cdot N_{\Delta}$ , the required time is negligible as compared with the total simulation time. During the time marching, the unknowns in FEM region at each time step is solved by forward and backward substitution with operation count proportional to  $2B \cdot N_{\text{fem}}$ . Since B is almost independent of  $N_{\Delta}$ , the FEM overhead in computation time turns out to be  $O(2BN_{\text{fem}}/N_{\Delta}^3) = O(1/N_{\Delta}) = O(N^{\frac{-1}{3}})$ .

## 2.4 Numerical Results

### 2.4.1 Grounded via

The present method is employed to characterize the microstrip with cylindrical grounded via shown in Fig. 2.1(a). The region around and under the rod is modeled by prism-gridded FEM. Fig. 2.3 compares the calculated scattering parameters with those by two staircasing FDTD analyses [32], for which one staircases the via to the inner boundary while the other to the outer boundary. As expected, the results by the present method lie somewhere in between. The dashed curve also shown in the figure for comparison is redrawn from the literature that is based on mode matching method but assuming an outer shielding box [37]. Good agreement can be noticed.

### 2.4.2 Through hole via

The second example considered here is the signal transmission across the microstrip lines on different layers by a through hole via as shown in the inset of Fig. 2.4. The region near the curved boundary is discretized into prism cells and solved by FEM, with the fields in the top and lower layers approximated by first-order Mur's boundary condition [35]. The region elsewhere is handled by the conventional FDTD, with super-absorbing first-order Mur boundary condition for the lattice truncation [36]. Fig. 2.4 compares the calculated results with those by the measurement [38]. Good agreement verifies that the present method is capable of characterizing objects with curved boundary.

It is interesting to investigate the influence on scattering characteristics if the two connected lines are oriented along different directions. The structure is shown in the inset of Fig. 2.5. Note that the geometric parameters chosen here are typical for realistic applications in multichip modules. The characteristic impedance of the microstrip is about  $50 \Omega$ . The simulation approach is similar to the previous example. Fig. 2.5 shows the scattering parameters versus frequency with connecting angle  $\theta = 0^\circ$ ,  $90^\circ$ , and  $180^\circ$  as a parameter. It is found that the transmission remains good and almost independent of  $\theta$  at low frequencies, say  $f < 10$  GHz. This supports the formulation and conclusions in [39], which assumes a symmetric field distribution on the clearance hole. It is also noticed that the transmission characteristics of the through hole via degrade significantly at high frequencies, say  $f > 60$  GHz. The degradation is strongly dependent on the connecting angle  $\theta$ . In those cases, the diameter of the clearance hole can be as large as one quarter of the wavelength. The field distribution around the via becomes highly asymmetric and should be carefully modeled to yield accurate results.

In case of arbitrary connecting angle  $\theta$  other than  $0^\circ$ ,  $90^\circ$ , and  $180^\circ$ , no proper rectangular grid in the FDTD region can fit the two microstrip lines simultaneously. The problem is divided into two subregions. One is above the ground plane while the other is below the ground plane. In general, the FDTD grids for the two subregions are tilt from each other. Please notice that the two subregions overlap on the clearance around the via on the ground plane. By the present method, we can carefully arrange different buffer meshes in these two subregions so that the identical triangular mesh on the clearance area can match to their individual FDTD grid on the outer boundary. Hence, the communication between those two subregions can be established by transferring the values of the unknowns on the clearance area to each other at each time step. Fig. 2.6 shows the calculated scattering parameters versus the connecting angle  $\theta$  with the frequency  $f = 20$  GHz and  $f = 60$  GHz as a parameter.

Fig. 2.7 shows the calculated scattering parameters at 20 GHz with diameter of the via as a parameter while fixing  $b = 0.508$  mm. The conventional FDTD may find difficulties in modeling both the via and hole accurately with such an arbitrary aspect ratio. However, the present method can model planar structures of curved boundary and yield satisfactory resolution. It can be found that better transmission can be resulted by a thinner via, as depicted in [39]

#### 2.4.3 CPW to CPS transition

A coplanar waveguide-to-coplanar stripline transition is analyzed. The layout is shown in Fig. 2.8(a). This transition is proposed by [40], aiming at maximizing the bandwidth and minimizing the insertion loss. In this simulation, the spatial increment

is 0.01524 mm and time increment is 0.0254 ps. The prism-gridded FEM is applied to deal with the region near the taper boundary while the conventional FDTD is employed elsewhere including the staircase approximation for the bond wires. Two PEC planes are placed 30 cells away from the planar circuit on the upper and lower boundaries, which do not exist in the measurement [41]. Roughly speaking, the whole simulation region is divided into  $260 \times 80 \times 60$  cells with 8 perfectly matched layers imposed on all the other walls. For the measurement, the transition structure of interest is placed in a back-to-back configuration. Fig. 2.8(b) compares the calculated scattering parameters with the measured data. Good agreement is obtained.

#### 2.3.4 Numerical experiment for computational complexity

Finally to be addressed is the experiment on computational efficiency of the present method. Due to the incorporation of FEM, the method requires additional computation time and memory in mesh generation, matrix calculation, and matrix decomposition during the preprocessing as well as in matrix solution during the time marching. The grounded via problem described above is used as an example for numerical experiment by tuning the division number per direction. Table 2.1 compares the required CPU time and memory storage to those in conventional FDTD algorithm. It is clearly verified that the overhead in the memory and CPU time for the present method is relatively insignificant and becomes smaller for a finer mesh.

## 2.5 Summary

The prism-gridded FEM has been successfully incorporated with a conventional FDTD method to deal with planar circuits with transversely curved boundary. This approach has been applied to characterize problems such as vias in packaging interconnections and transition between different transmission lines. In essence, it can also be generalized to deal with various structures such as planar circuits, waveguides with step transition, and whatever can be longitudinally divided into several building layers. Owing to the flexibility provided by the FEM, the present scheme can easily model structures with objects of arbitrary aspect ratio in shape, which is hard to access by the conventional FDTD.

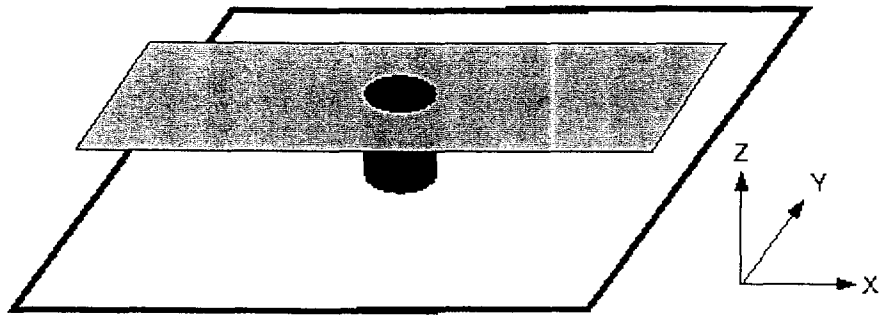
The additional computational load of the present method in comparison with the conventional FDTD method has been analyzed both theoretically and numerically. In theory, the overhead of the FEM in memory and the CPU time requirement is inversely proportional to the division number per direction and, thus, negligible for fine mesh. In practice, simulation results depict that the present method remains very efficient, with computational overhead 15% smaller for most applications.

$\Delta$	mesh $N_x \times N_y \times N_z$	method	pre-processing		time marching		FEM overhead	
			time	memory	time/steps	memory	time	memory
1.00	$110 \times 70 \times 30$	extended	0.34	92	43.63/80	6580	14.42%	8.51%
		FDTD	-	-	38.13/80	6064		
0.80	$138 \times 87 \times 38$	extended	0.41	112	99.63/100	12296	12.08%	6.59%
		FDTD	-	-	88.89/100	11536		
0.67	$165 \times 105 \times 45$	extended	0.63	142	196.72/120	20544	10.01%	5.33%
		FDTD	-	-	178.82/120	19504		
0.57	$193 \times 122 \times 53$	extended	0.78	164	353.69/140	32020	9.18%	4.20%
		FDTD	-	-	323.94/140	30728		
0.50	$220 \times 140 \times 60$	extended	0.92	180	575.76/160	47072	7.94%	3.77%
		FDTD	-	-	533.42/160	45364		

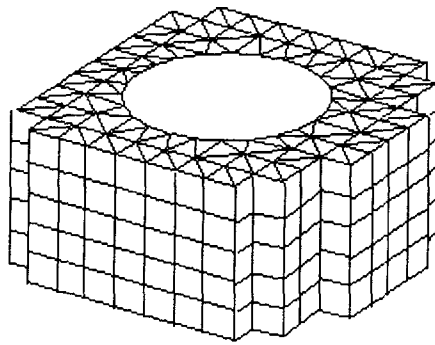
(Program is executed in IBM RS 6000/3BT. The units are of time sec and of memory kbytes.)

Table 2.1 Comparison of the computation time and memory between present method and conventional FDTD method.





(a)



(b)

Fig. 2.1 (a) Geometry of microstrip with grounded via and (b) the mesh division near and under the grounded via.

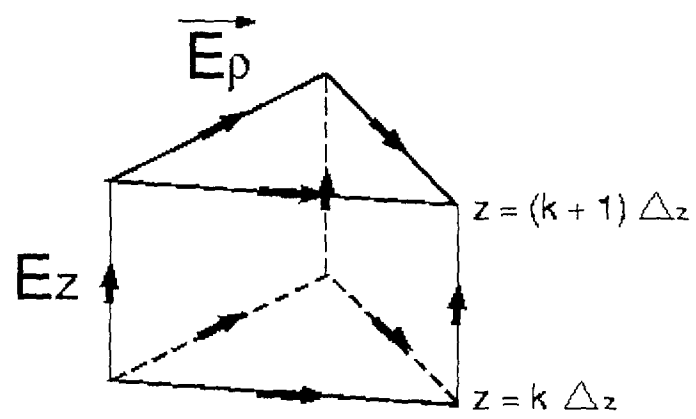


Fig. 2.2 The prism element and the assignment of unknown fields.

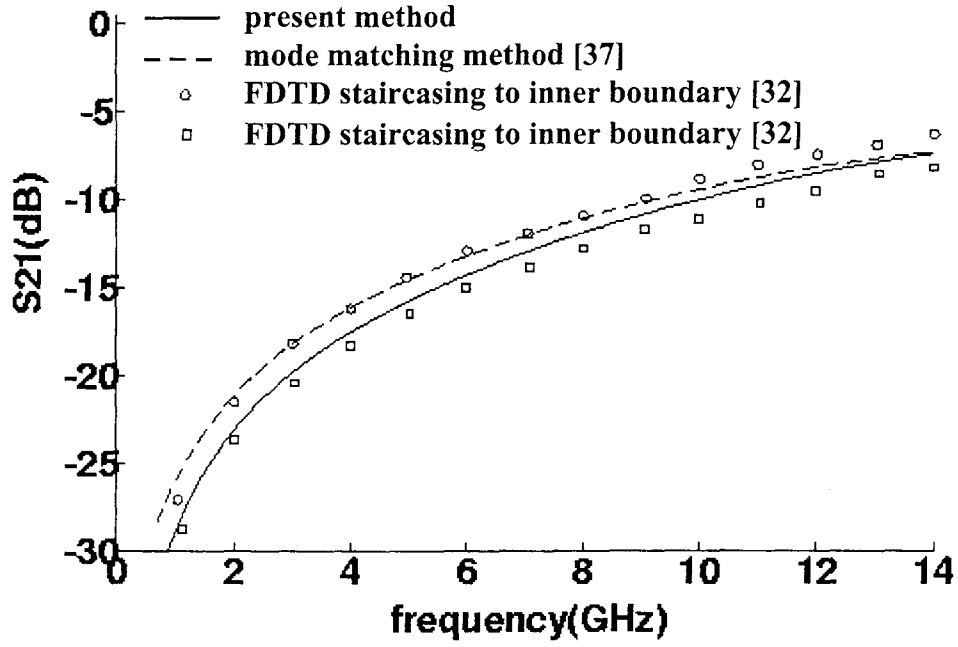


Fig. 2.3 Transmission coefficient along a microstrip with grounded via. Comparison between present method and other numerical methods. The microstrip is of width 2.3 mm and height 0.8 mm, the via diameter is 0.6 mm, and the substrate is of dielectric constant 2.32. The solution region is basically divided into  $110 \times 70 \times 30$  cells ( $\Delta = 0.1$  mm,  $\Delta_t = 0.167$  ps) with 8 perfectly matched layers.

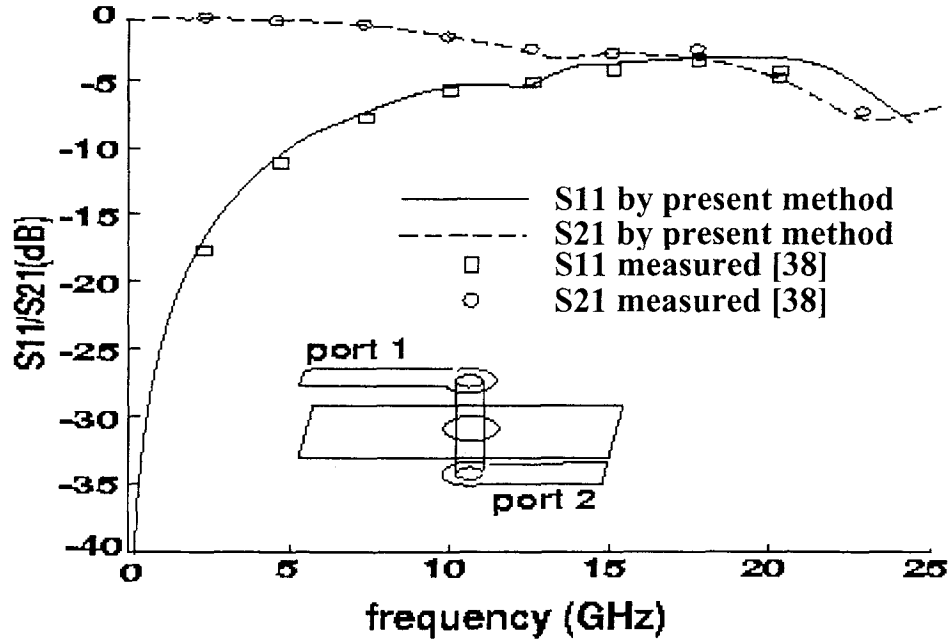


Fig. 2.4 Scattering parameters of a through hole via. Comparison between the simulated results with the measured data. The microstrip is of width 1.6 mm and height 3.3 mm, the diameters of the rod and the clearance hole are 1.5 and 3.9 mm respectively, and the substrate is of dielectric constant 3.4. The simulation region is basically divided into  $70 \times 80 \times 48$  cells with  $\Delta_x = \Delta_y = 0.206$  mm,  $\Delta_z = 0.4$  mm, and  $\Delta_t = 0.333$  ps.

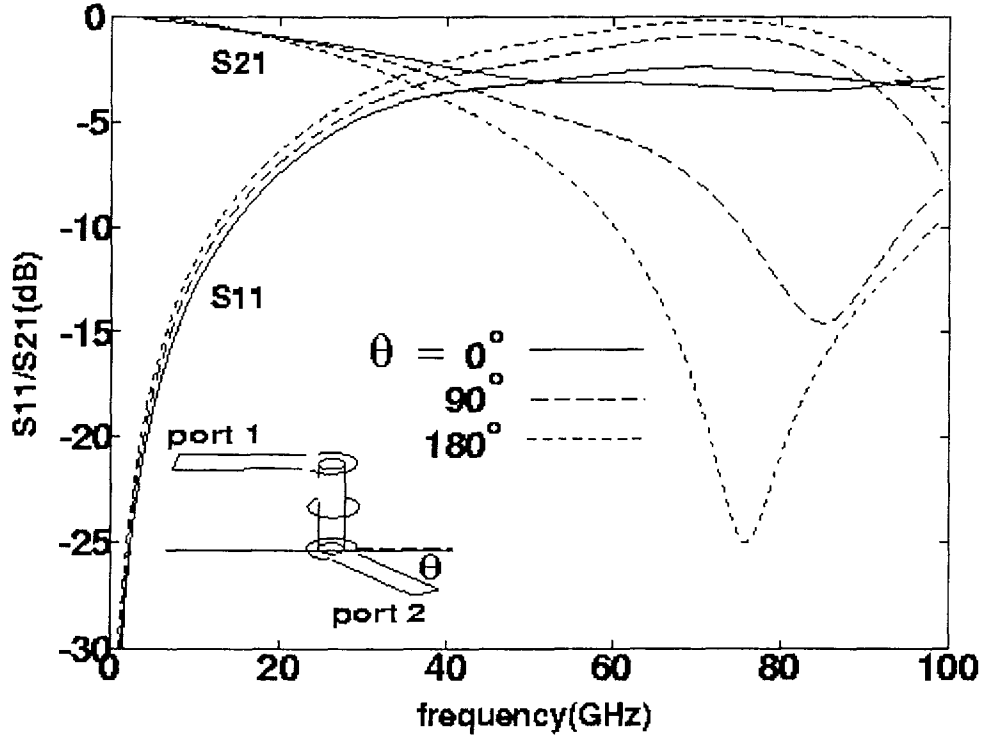


Fig. 2.5 Calculated scattering parameters of a through hole via with connecting angle  $\theta = 0^\circ$ ,  $90^\circ$ , and  $180^\circ$  as a parameter. The microstrip is of width 0.254 mm and height 0.239 mm, the diameters of the via and clearance hole are 0.254 mm and 0.508 mm, respectively, and the substrate is of dielectric constant 4.3. The solution region is basically divided into  $86 \times 56 \times 48$  cells with  $\Delta_x = \Delta_y = 0.02117$  mm,  $\Delta_z = 0.05959$  mm, and  $\Delta_t = 0.0353$  ps.

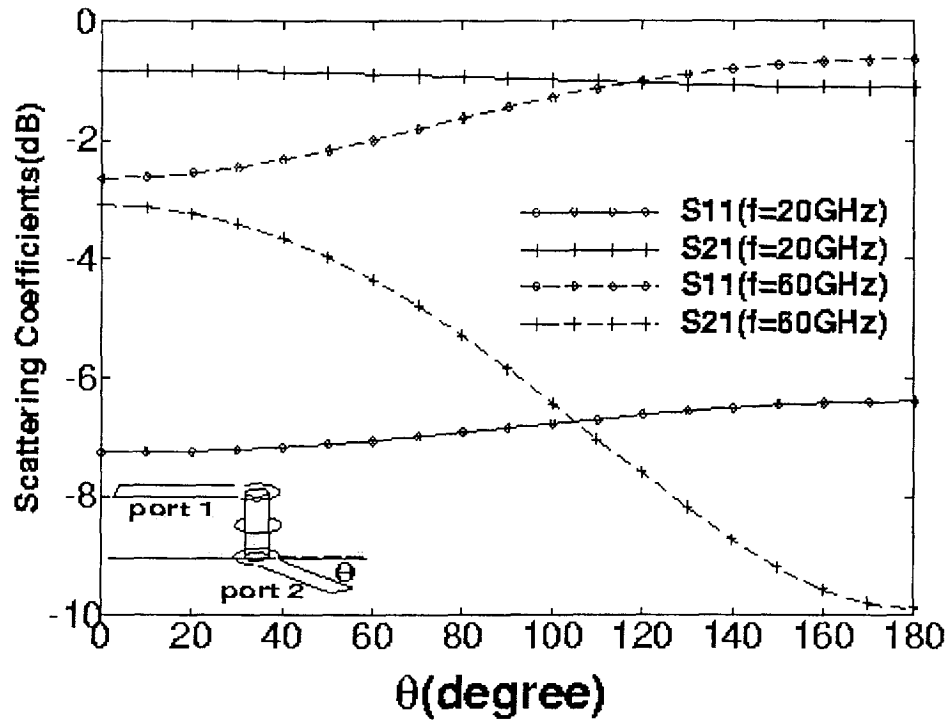


Fig. 2.6 Scattering parameters versus the connecting angle  $\theta$  with the frequency= 20 GHz and 60 GHz. All other structural parameters are the same as those in Fig. 2.5.

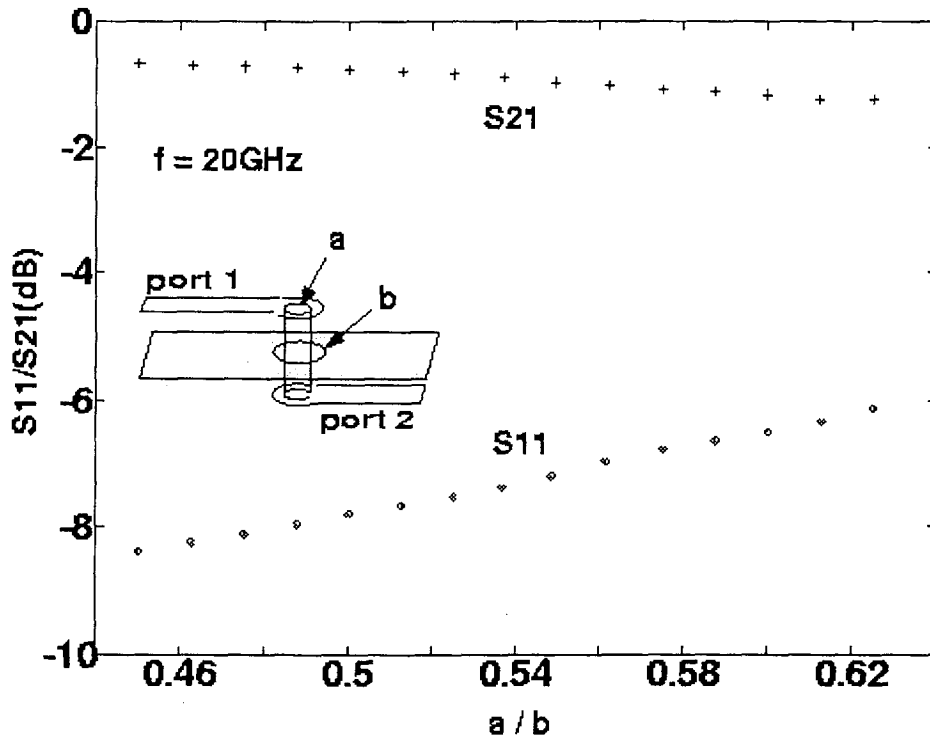


Fig. 2.7 Scattering parameters versus the diameter ratio of via to hole at frequency= 20 GHz. All other structural parameters are the same as those in Fig. 2.5.

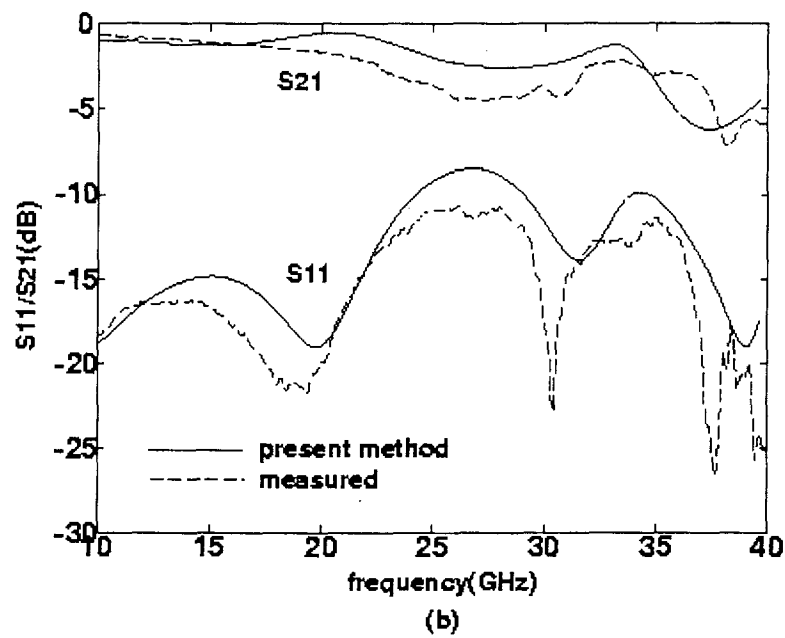
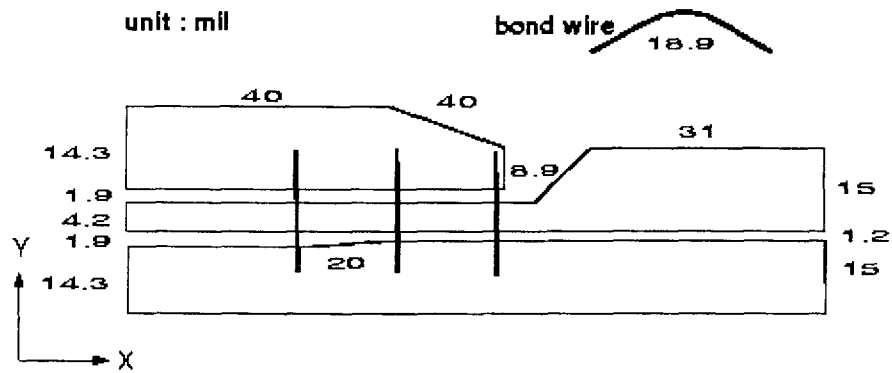


Fig. 2.8 (a) Layout of a CPW to CPS transition (b) Comparison of the calculated  $|S_{11}|$  and  $|S_{21}|$  with measured data. The substrate is of height 25 mil and dielectric constant 9.8.



## Chapter 3

# A Novel Finite Element Basis Capable of Eliminating Late-Time Instability

### 3.1 Introduction

The hybrid FE/FDTD method has been proposed to solve electromagnetic scattering of arbitrarily shaped dielectric objects. The full flexibility of finite-element method can be fully exploited to alleviate FDTD in modeling curved geometries. Practices include the triangular node elements for two-dimensional problems [9], tetrahedral edge elements for three-dimensional problems [10], and prism elements for two and half dimensional planar structures, as described in the previous chapter. Numerical results of early time simulation validate that the method has the advantage of accuracy, flexibility, stability, and computational efficiency. However, the simulation is noticed to exhibit numerical instability in the very late time although both the FETD and FDTD are found to be numerical stable if employed separately.

The late-time instability happens not only in FE/FDTD but also in most of the afore-mentioned modified FDTD schemes. Yee *et al.* noticed that the computation error grows up in the additional local coordinate system near the curved surfaces and suggested a spatial average scheme to resolve this instability [8]. Since the spatial average may become more complicated for non-rectangular grids, some researchers prefer a similar idea by taking average in time, e.g., [12], [13], [42]. Taking sufficient average in time or space can filter out the high frequency numerical noise, but sacrifice accuracy as a tradeoff [42]. Railton *et al.* believes that the late-time instability can be contributed to the non-reciprocity in the time marching scheme and proposed modified equations based on a passive equivalent circuit [43], [44].

The finite-element mesh in FE/FDTD exactly matches with the finite-difference grid. It is not clear why the numerical errors will be accumulated to exhibit late-time instability. A detailed check reveals the non-perfect match between the bases employed in the two methods: FDTD assumes a uniform field distribution inside one cell; while FEM interpolates the field inside an element by linear bases. When updating the electric fields solved by the two methods at the overlapping boundary, error might be generated due to the differences of field distribution. To circumvent

this problem, we devise a novel finite-element basis function, which can match with the uniform basis in FDTD.

### 3.2 A Novel Finite-Element Basis

For sake of simplicity, consider the wave scattering of an arbitrarily shaped two-dimensional cylinder. To suitably model the curved boundary, the region near the boundary is divided into triangular mesh, same as that in FE/FDTD of [9]. As opposed to the conventional linear basis, the electrical field inside a triangular element is expressed by

$$E_z(\vec{r}, t)\hat{z} = \sum_{j=1}^3 E_j(t) f_j(\vec{r}) \hat{z} \quad (3.1)$$

where

$$f_j(\vec{r}) = \begin{cases} 1, & \vec{r} \text{ in region } \Omega_j \\ 0, & \vec{r} \text{ elsewhere} \end{cases}$$

is a pulse basis extended from the vertex node  $\vec{r}_j$  to circum-center O of the triangular element as shown in Fig. 3.1(a). The magnetic flux density in the element is expressed by

$$\vec{B}(\vec{r}, t) = \sum_{j=1}^3 \varphi_j(t) \vec{W}_j(\vec{r}) \quad (3.2)$$

where

$$\vec{W}_j(\vec{r}) \equiv \frac{\vec{r} - \vec{r}_j}{2A^{(e)}}$$

and  $A^{(e)}$  is the area of this element. Fig. 3.1(b) plots the vector basis  $\vec{W}_1(\vec{r})$ . Note that the element is subdivided into three regions and inside each of which, the electric field is a constant by this basis assignment. Also, it can be verified that  $\varphi_j(t)$  equals the total magnetic flux flowing out of the j'th side of the element.

Applying Faraday's law over the j'th side of this element yields

$$\frac{d\varphi_j(t)}{dt} = E_{j+1}(t) - E_{j+2}(t) \quad (3.3)$$

Here, j, j+1, and j+2 follow the conventional index order in a triangular element, say if j denotes node 2, then j+1 denotes node 3 and j+2 denotes node 1. On the other

hand, the application of Ampere's law over all the elements containing the node  $\vec{r}_i$  as shown in Fig. 3.2 yields

$$\begin{aligned} \sum_e \varepsilon^{(e)} A_i^{(e)} \frac{dE_i(t)}{dt} &= \sum_e \frac{1}{\mu^{(e)}} \sum_{j=1}^3 \int_{\vec{r}_{i+2}}^{\vec{r}_{i+1}} \vec{W}_j(\vec{r}) \cdot d\vec{r} \varphi_j(t) \\ &= \sum_e \frac{1}{2\mu^{(e)} A^{(e)}} \sum_{j=1}^3 \left( |\vec{r}_{i+1}' - \vec{r}_j|^2 - |\vec{r}_{i+2}' - \vec{r}_j|^2 \right) \varphi_j(t) \end{aligned} \quad (3.4)$$

Here,  $\varepsilon^{(e)}, \mu^{(e)}$  are the permittivity and permeability of the material,  $\vec{r}_j'$  denotes the center point on the  $j$ 'th side of the element, and  $A_i^{(e)}$  is the counterclockwise area of  $\Omega_i$  formed by  $\vec{r}_i, \vec{r}_{i+2}', \vec{r}_{i+1}'$ .

Substitution (3.3) to (3.4), the electrical field in the finite element region satisfies

$$\sum_e [C^{(e)}] \cdot \frac{d^2}{dt^2} [E^{(e)}(t)] = \sum_e [D^{(e)}] \cdot [E^{(e)}(t)] \quad (3.5)$$

Here,  $[E^{(e)}(t)]$  is a column vector formed by the electric fields at the three vertices of a particular element. The two matrices in (3.5) are

$$[C^{(e)}] = \varepsilon^{(e)} \begin{bmatrix} A_1^{(e)} & 0 & 0 \\ 0 & A_2^{(e)} & 0 \\ 0 & 0 & A_3^{(e)} \end{bmatrix}; \quad [D^{(e)}] = \frac{1}{2\mu^{(e)} A^{(e)}} \begin{bmatrix} d_{12} + d_{13} & -d_{12} & -d_{13} \\ -d_{12} & d_{12} + d_{23} & -d_{23} \\ -d_{13} & -d_{23} & d_{13} + d_{23} \end{bmatrix} \quad (3.6)$$

in which

$$d_{12} = |\vec{r}_3 - \vec{r}_3'|^2 - \frac{1}{4} |\vec{r}_2 - \vec{r}_1|^2$$

and similarly for  $d_{13}$  and  $d_{23}$ . This equation (3.5) can be solved by applying the Crank- Nicholson scheme in the way already described in [9].

In the interface between FEM and FDTD, the region is divided into right triangles. Consider a node in the interface region shown in Fig. 3.3, the constant electric field assumed in the present basis exactly match with that in the FDTD method. Moreover, we can employ (3.4) to obtain the equation for the electric field at node 0. Due to the choice of the basis function, it can be found that the term  $d_{05} = 0$  when applying (3.5) to either triangle  $\Delta 015$  or triangle  $\Delta 025$ . As a result, the wave equation becomes

$$\Delta_x \Delta_y \varepsilon \frac{d^2 E_0(t)}{dt^2} = \frac{1}{\mu \Delta_x \Delta_y} \left[ -2(\Delta_x^2 + \Delta_y^2) E_0(t) + \Delta_y^2 (E_1(t) + E_3(t)) + \Delta_x^2 (E_2(t) + E_4(t)) \right] \quad (3.7)$$

which is exactly the same as that derived by taking FD discretization to Maxwell's equations in rectangular grid.

### 3.3 Numerical Results

The present method has been applied to deal with a two-dimensional TM scattering off a circular dielectric cylinder. As given in [9, Fig. 3], a TM pulse of Gaussian waveform is incident from  $-x$  direction onto a cylinder of radius  $r = 10\text{cm}$  and dielectric constant  $\varepsilon_r = 4$ . The Gaussian pulse is chosen such that 90% of energy is confined in a time interval of  $0.667\text{nsec}$  or equivalently, in the frequency range from dc to about  $1\text{GHz}$ . In the numerical simulation, the division parameter is chosen as  $\rho = c\Delta t / \Delta x = 0.5$  and the center of the cylinder is chosen as the observation point.

Fig. 3.4 shows the calculated waveforms of the total electric field at the observation point with different division sizes  $\Delta x = \Delta y = 2, 1, 0.5$ , and  $0.25\text{cm}$  as a parameter. It is worthy mentioning that the wavelength corresponding to the frequency component of  $1\text{GHz}$  is about  $15\text{cm}$  in the material. The division of  $\Delta x = \Delta y = 2\text{cm}$  do not satisfy the common rule of at least ten divisions per wavelength. Nonetheless, the present method can correctly model the non-regular shape of the scatterer and is found to exhibit good accuracy even in the very rough division size. The numerical convergency is satisfactory as the division becomes finer.

Fig. 3.5 shows the late-time response for the case of  $\Delta x = \Delta y = 1\text{cm}$ . Both the results by conventional FEM linear basis [9] and the present basis are presented for comparison. It can be found that the conventional FEM results in a significant numerical instability after 6000 time steps, or  $6000 \cdot c\Delta t = 3000\text{cm}$ , in the figure. To the contrary, there is not late-time instability if we employ the present basis. Actually, we have tried other division sizes and up to much longer time. No late-time instability can be noticed.

### 3.4 Summary

A novel finite element basis to circumvent the late-time instability problem encountered in the hybrid finite-element /finite-difference time-domain method is proposed. In the conventional hybrid FE/FDTD, the electric field is interpolated by

linear function in FEM region while assumed to be piecewise constant in FDTD region. Although the FEM mesh can ideally match with the FDTD grid, the small field imbalance can accumulate to develop instability in the very late time. In the newly proposed approach, the electric field in the FEM region is assumed to be piecewise constant. The assignment of the electric field in the interface region of FDTD and FEM is identical to each other. Specially, the governing discretized equations for FEM in the interface region where all the elements are right triangles can be reduced to exactly the same as those for FDTD. It is the perfect match in not only the mesh but also the field basis that totally eliminate the numerical instability due to the interface of the two time-domain analyses.

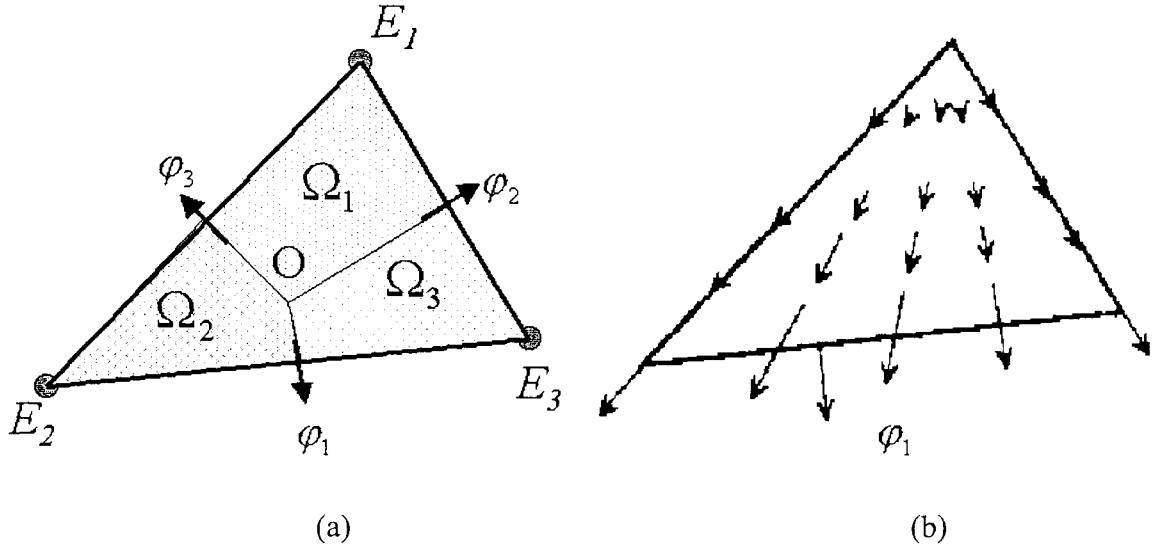


Fig. 3.1 A novel finite element basis for hybrid FE/FDTD method. (a) pulse basis for electric field, and (b) vector basis  $\vec{W}_1(\vec{r})$  for magnetic field.

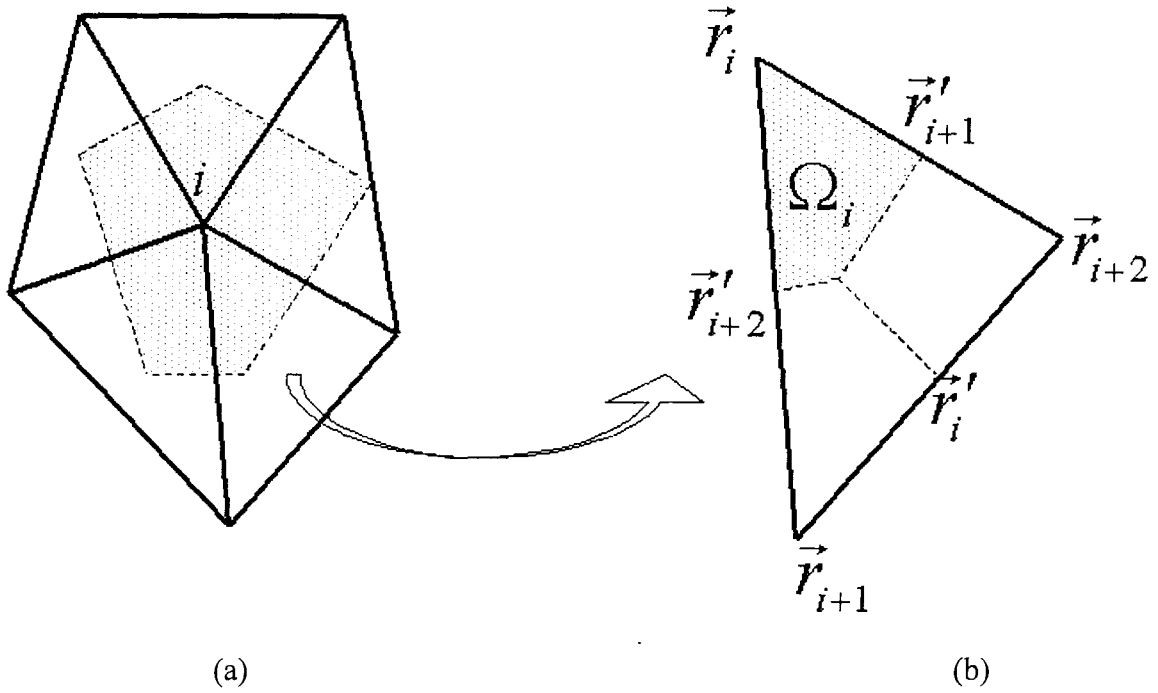


Fig. 3.2 (a) Applying Ampere's law for the electric field at node  $\vec{r}_i$  and (b) the integral inside an element.

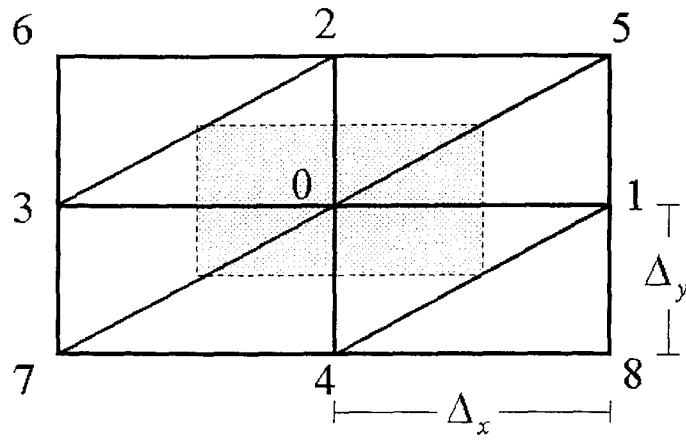


Fig. 3.3 Mesh in the interface region

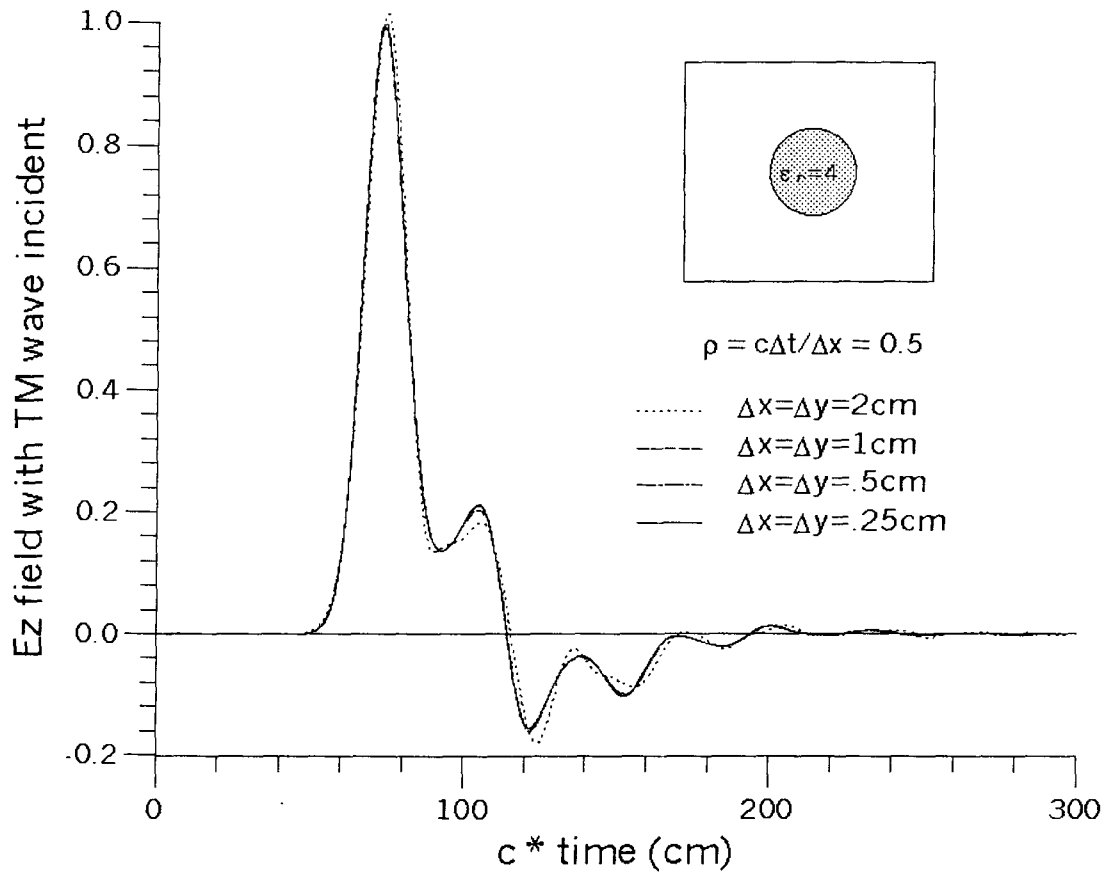


Fig. 3.4 The total field at the cylinder center due to a Gaussian TM wave incident from  $-x$  direction.

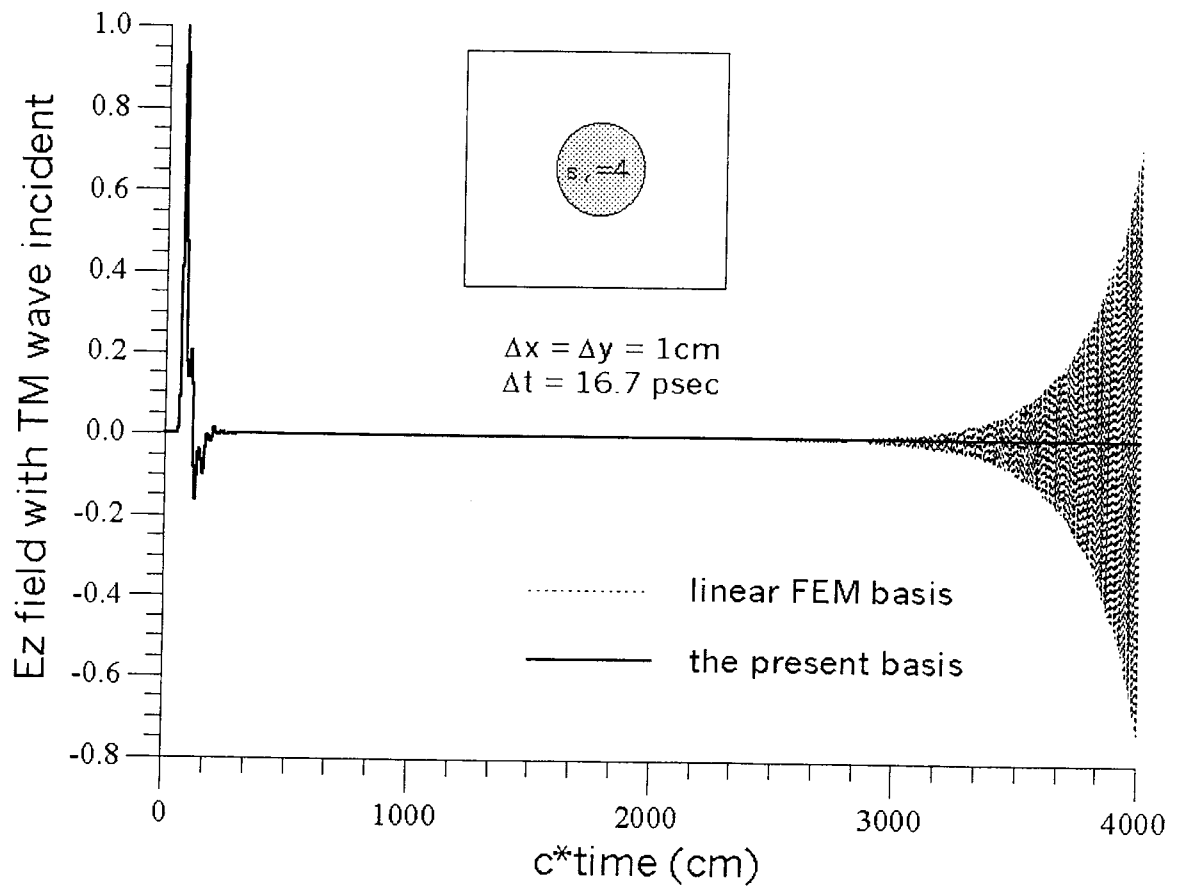


Fig. 3.5 Comparison of the late-time response by conventional FEM linear basis and the present basis.



## Chapter 4

### Thin-Slot Formalism

#### 4.1 Introduction

One of the major drawbacks of FDTD is in modeling structures involving gaps or thin slots. A fine FDTD mesh to fit the structures will dramatically increase the memory storage and CPU time required in the numerical simulation. Several thin-slot formalism (TSF) based on the assumption of fields around the slot are proposed to alleviate this difficulty [15]-[18].

The simplest uniform TSF assumes a constant electric field distribution across the slot [16]. This derivation is straightforward but the accuracy is not satisfactory. In capacitive TSF [15], the field on the sidewalls of the unit FDTD cell containing the slot is assumed to be negligible as compared to the field near the slot. By considering canonical problems of two- and three-dimensional slots in infinitesimally thin walls, the accuracy has been evaluated and the results indicate that up to 10 % error may be present in the total electric and magnetic fields both near and far from the gap [45].

Later, a hybrid TSF was proposed by treating the slot field as unknown and applying the integral equation approach to solve it [17]. The accuracy of hybrid TSF and capacitive TSF was compared for structures with shielding enclosures [46]. Hybrid TSF has better accuracy, but the algorithm is much more complicated. Besides, the late-time instability will occur for hybrid TSF method. An easier approach is to revisit the assumptions made in deriving the capacitive TSF. An enhanced thin-slot formalism was thus proposed by assuming a  $\frac{1}{r}$ -decay field behavior away from the slot center [18]

In this chapter, an improved expression of the thin-slot formalism is proposed to alleviate the gridding of the FDTD solution for electromagnetic problems involving narrow slots. By applying the conformal mapping technique, the varying field distribution near the slots is analytically derived and fully cast into a unit FDTD cell with effective permittivity and permeability. As a result, this formalism permits narrow slots to be modeled without reducing spatial grid size, even when the slot gap width is much smaller than one space grid. The method has been applied to several transmission line problems and the results are compared with conventional FDTD

method and other thin-slot formalisms. It is verified that the proposed method is easy to implement, numerically efficient, and accurate.

## 4.2 Unified Thin-Slot Formalism

To simplify the analysis, consider a slotline with the slot along the  $z$ -direction and the metallization plane on the  $x$ - $y$  plane. Fig. 4.1 shows a typical FDTD mesh in which the cell size is  $\Delta x$ ,  $\Delta y$ , and  $\Delta z$  in  $x$ ,  $y$ , and  $z$  directions, respectively, and  $\Delta x$  is much larger than the width of the slot. The FDTD scheme calls for repeatedly updating the  $\vec{E}$  and  $\vec{H}$  field sequentially. As shown in Fig. 4.1,  $E_x(i - \frac{1}{2}, j, k)$  can be updated using Ampere's law by

$$\begin{aligned} & [H_z(i - \frac{1}{2}, j + \frac{1}{2}, k) - H_z(i - \frac{1}{2}, j - \frac{1}{2}, k)]\Delta_z + \\ & \int_{j-\frac{1}{2}}^{j+\frac{1}{2}} [H_y(i - \frac{1}{2}, y, k - \frac{1}{2}) - H_y(i - \frac{1}{2}, y, k + \frac{1}{2})] dy \\ & = \epsilon_0 \frac{d}{dt} \int_{j-\frac{1}{2}}^{j+\frac{1}{2}} E_x(i - \frac{1}{2}, y, k) dy \cdot \Delta_z \end{aligned} \quad (4.1)$$

where all the field components are arguably assumed to be slowly varying along  $z$ . However, the variations of  $E_x$  and  $H_y$  along  $x$  and  $y$  directions are significant and deserve special consideration.

Define the average field along the edge of a unit cell

$$\begin{aligned} \tilde{H}_y(i - \frac{1}{2}, j, k \pm \frac{1}{2}) &= \frac{1}{\Delta_y} \int_{j-\frac{1}{2}}^{j+\frac{1}{2}} H_y(i - \frac{1}{2}, y, k \pm \frac{1}{2}) dy \\ \tilde{E}_x(i - \frac{1}{2}, j, k) &= \frac{1}{\Delta_x} \int_{i-1}^i E_x(x, j, k) dx \end{aligned} \quad (4.2)$$

then (4.1) becomes

$$\begin{aligned} & \Delta_z [H_z(i - \frac{1}{2}, j + \frac{1}{2}, k) - H_z(i - \frac{1}{2}, j - \frac{1}{2}, k)] - \\ & \Delta_y [\tilde{H}_y(i - \frac{1}{2}, j, k + \frac{1}{2}) - \tilde{H}_y(i - \frac{1}{2}, j, k - \frac{1}{2})] \\ & = \epsilon_0 \epsilon_r(k) \Delta_z \Delta_y \frac{d}{dt} \tilde{E}_x(i - \frac{1}{2}, j, k) \end{aligned} \quad (4.3)$$

where

$$\epsilon_r(k) = \frac{[\int_{j-\frac{1}{2}}^{j+\frac{1}{2}} E_x(i - \frac{1}{2}, y, k) dy] / \Delta_y}{\tilde{E}_x(i - \frac{1}{2}, j, k)} = \frac{[\int_{j-\frac{1}{2}}^{j+\frac{1}{2}} E_x(i - \frac{1}{2}, y, k) dy] / \Delta_y}{[\int_{i-1}^i E_x(x, j, k) dx] / \Delta_x} \quad (4.4)$$

It is worth noting that the constant  $\varepsilon_r(k)$  is determined by the field distribution near the slot but independent of the field amplitude.

Similarly,  $H_y$  field along the slot can be updated using Faraday's law by

$$\begin{aligned} & \Delta_x [\tilde{E}_x(i - \frac{1}{2}, j, k + 1) - \tilde{E}_x(i - \frac{1}{2}, j, k)] \\ &= -\mu_0 \mu_r(k + \frac{1}{2}) \Delta_x \Delta_z \frac{d}{dt} \tilde{H}_y(i - \frac{1}{2}, j, k + \frac{1}{2}) \end{aligned} \quad (4.5)$$

where

$$\mu_r(k + \frac{1}{2}) = \frac{[\int_{i-1}^i H_y(x, j, k + \frac{1}{2}) dx] / \Delta_x}{[\int_{j-\frac{1}{2}}^{j+\frac{1}{2}} H_y(i - \frac{1}{2}, y, k + \frac{1}{2}) dy] / \Delta_y} \quad (4.6)$$

Under the thin-slot approximation, the field near the slot is very close to that of a transmission line, so that  $E_x$  and  $H_y$  has the same field distribution. As a result, the equivalent permeability  $\mu_r(k + \frac{1}{2})$  can be related to the equivalent permittivity  $\varepsilon_r(k)$  by

$$\mu_r(k + \frac{1}{2}) = \frac{1}{\varepsilon_r(k)} \quad (4.7)$$

### 4.3 Field Distribution by Conformal Mapping

The equivalent effective permittivity in (4.4) is determined by the field distribution near the slot in the unit cell. It is a good approximation that the field near the slot is the same as the two-dimensional TEM field of the slotline. Through conformal mapping technique, the slotline can be mapped to an easier solution region as shown in Fig. 4.2 by the Schwartz-Chirstoffel transformation [47]

$$w = u + jv = j\left(\frac{1}{\pi} \sin^{-1} \frac{2z}{s} + \frac{1}{2}\right) \quad (4.8)$$

where  $s$  is the width of the slot.

The mapped region in  $(u, v)$  plane is a semi-infinite parallel plate structure for which the potential distribution can be analytically obtained by  $\phi(u, v) = v$ . By complex analysis, the potential distribution in  $(x, y)$  plane is

$$\phi(x, y) = v = \text{Im}(f(z)) \Big|_{z=x+iy} \quad (4.9)$$

and the electric field distribution can be readily derived by  $\vec{E} = -\nabla\phi$ . Thus, the field component  $E_x$  required in (4.4) is

$$E_x = -\frac{\partial v}{\partial x} = \frac{\frac{-2}{s\pi}}{\text{Re}\left(\sqrt{1 - \left(\frac{2(x+iy)}{s}\right)^2}\right)} \quad (4.10)$$

At  $y = 0$  plane, it can be simplified to be

$$E_x|_{y=0} = \frac{\frac{-2}{s\pi}}{\sqrt{1 - \left(\frac{2x}{s}\right)^2}} \quad (4.11)$$

and at  $x = 0$  plane,

$$E_x|_{x=0} = \frac{\frac{-2}{s\pi}}{\sqrt{1 + \left(\frac{2y}{s}\right)^2}} \quad (4.12)$$

It is worth mentioning that, as  $s$  tends to zero, (4.12) reduces to a  $1/y$  dependence assumed in the enhanced TSF [18].

Substituting (4.11) and (4.12) into (4.4), the equivalent permittivity for the thin-slot is

$$\varepsilon_r(k) = \frac{2\Delta_x}{\pi\Delta_y} \sinh^{-1}\left(\frac{\Delta_y}{s}\right) \quad (4.13)$$

It can be substituted to the traditional FDTD algorithm for updating the  $E_x$  and  $H_y$  fields at slot.

For the more general cases in that the slot has finite depth, the conformal mapping technique is also available [48]. However, the expression for the  $E_x$  field becomes much more complicated than that in (4.11) and (4.12). A simple analytic expression for  $\varepsilon_r(k)$  like (4.13) is not possible, and the numerical solution should be resorted to.

## 4.4 Numerical Results

It is interesting to compare the equivalent effective permittivity  $\varepsilon_r(k)$  used in different TSF's. Subject to the same definition in (4.2) and in the same coordinates adopted here, the various TSF's can be written in the same form as (4.3) and (4.5), but different expressions for  $\varepsilon_r(k)$ . Table 4.1 lists the  $\varepsilon_r(k)$  for capacitive TSF [15], uniform TSF [16], and enhanced TSF [18]. Note that the effective permittivity for enhanced TSF does not appear directly in reference [18]. Here, the expression is derived by assuming that the  $E_x$  field is uniform for  $|y| < s/4$  near the slot and follows the  $1/y$ -decay for  $|y| > s/4$  [18, eq. (1)]. In the common case that

$\Delta_x = \Delta_y = \Delta_z = \Delta$ , Fig. 4.3 shows  $\varepsilon_r(k)$  versus  $\Delta/s$ . It is found that the expressions of capacitive TSF, enhanced TSF, and the present TSF are close to each other for small  $s$ .

The present thin-slot formalism is applied to calculate the characteristic impedance  $Z_0$  of a coplanar strip (CPS) transmission line. Shown in the inset of Fig. 4.4, the total width of the CPS is fixed at  $2w + s = 1.1 \text{ mm}$ , with the dielectric constant of the substrate being  $\varepsilon_r = 1$  for sake of simplicity. In numerical simulation, FDTD cells of grid size is  $\Delta = 0.1 \text{ mm}$ . The total solution region is divided into  $21 \times 30 \times 300$  cells along  $x$ ,  $y$ , and  $z$  directions, respectively, with additional five cells Berenger's PML outside this region. The excitation is a retarded Gaussian pulse of the form

$$\vec{E}(x, y, t) = \vec{\Psi}(x, y) \exp \left[ - \left( \frac{t - t_0}{t_w} \right)^2 \right] \quad (4.14)$$

where  $\vec{\Psi}(x, y)$  is the quasi-static field solved by Laplace equation,  $t_0 = 300\Delta$ ,  $t_w = 100\Delta$  and the soft source [49] is located at  $z = 5\Delta$ .

For the numerical results, the voltage  $V(t, z)$  and the current  $I(t, z)$  are recorded at  $z = 200\Delta$ . The characteristic impedance can then be calculated by

$$Z_0(\omega, z) = \frac{\mathcal{F}[V(t, z)]}{\mathcal{F}[I(t, z)]} \quad (4.15)$$

where  $\mathcal{F}[\cdot]$  means Fourier transform. Because the effective permittivity and permeability are reciprocal, the product of effective permittivity and permeability is

equal to  $c^{-2}$ . It means that the velocity of wave is equal to the other cell; thus, it will fit the criterion of the stability condition.

The exact characteristic impedance for the present CPS structure is available by using the conformal mapping technique. In the case of thin slots ( $s < \Delta$ ), Fig. 4.4 shows the quasi-static characteristic impedance calculated by the present TSF versus the ratio  $s/\Delta$ . The results are also compared with those by the conformal mapping technique and by other TSF's. It is found that the computational results by the present TSF concurs with the exact solution, especially when the slot width is much smaller than the cell size. The larger discrepancy at larger  $s$  is expected since the end effects due to the finite size of metallization may not be negligible.

Comparatively, the results by other TSF's are not so satisfactory. The uniform TSF [16] results in a significant underestimation in  $Z_0$ . The capacitive TSF [15] partially takes into account the nonuniform variation of the slot field, but the accuracy deteriorates as  $s/\Delta$  increases. The enhanced TSF [18] can yield accurate results for small  $s$ , say  $s < 0.2\Delta$ , while its assumption of  $1/r$ -decay in the field behavior becomes worse for larger  $s$  as evident by (4.12).

In the FDTD simulation under an incident wave of Gaussian pulse, the characteristic impedance of the transmission line can be extracted over a wide spectrum by (4.15). The solid curves for Fig. 4.5 shows the real and imaginary part of  $Z_0$  versus frequency by the present TSF for the case of  $s = 0.5\Delta$ . For the sake of comparison, the same problem is also solved by the traditional FDTD with fine divisions such that the slot is divided into 2, 4, and 6 cells, respectively. The extracted results are shown by the dashed curves in the figure.

Theoretically, the propagating wave will be a purely TEM wave for the present CPS where the relative permittivity of substrate is set to be  $\epsilon_r = 1$ . This means that  $Z_0$  should be a constant independent of frequency and its imaginary part should be zero. It can be seen from Fig. 4.5 that the results by the present TSF closely comply with the characteristics as required by TEM. However, the results by traditional FDTD not only show large variations with respect to frequency but also exhibit significant imaginary parts. Such discrepancy against the theoretical prediction remains even with a much finer division, without mentioning its prohibitive numerical requirement in memory and CPU time. This demonstrates the advantages and efficiencies of the present TSF over the traditional FDTD method.

The present TSF can be applied to deal with other transmission lines which

involve thin slots, e.g., the coplanar waveguide (CPW). In this case, the electric field behavior near the slot derived in (4.10)-(4.12) is not exact but can still serve as a good approximation. Choosing the FDTD mesh similar to that in Fig. 4.4, the center of the two slots of CPW are separated by  $7\Delta$  ( $s + w = 7\Delta$ ) while the slot width  $s$  varies from 0 to a cell size  $\Delta$ . Fig. 4.6 shows the characteristic impedance versus the slot width ratio  $s/w$  of the CPW at the low frequency limit. Also shown in the figure for comparison are the results obtained by the conformal mapping technique and by other TSF's. Among the various TSF's, the present TSF compares most favorably to the analytic solution by the conformal mapping technique. However, the discrepancy increases for larger  $s$ , since the field distribution near the slot of CPW is assumed to be that of a single slot.

## 4.5 Summary

A novel thin-slot formalism is derived. The derivation is based on an exact modeling of the field distribution on the slot, which is analytically solved for the slotline by the conformal mapping technique. As a result, the formalism can not only be suitable for the slotline, but also serve as a good approximation for other practical structures that involve narrow slots with width much smaller than a wavelength. The formalism can be ideally cast into the FDTD analysis so that it is not necessary to reduce FDTD cell size to make concessions to slot size. Numerical results have demonstrated that the formalism is superior to other methods in dealing with structures of thin slots.

Methods	capacitive TSF	uniform TSF	enhanced TSF	The present TSF
$\varepsilon_r(k)$	$\frac{\Delta_x}{\Delta_y} \frac{K \left[ 1 - \left( \frac{s}{\Delta_x} \right)^2 \right]}{K \left[ \left( \frac{s}{\Delta_x} \right)^2 \right]}$	$\frac{\Delta_x}{s}$	$\frac{\Delta_x}{2\Delta_y} \left[ \ln \left( \frac{2\Delta_y}{s} \right) + 1 \right]$	$\frac{2\Delta_x}{\pi\Delta_y} \sinh^{-1} \left( \frac{\Delta_y}{s} \right)$

Table 4.1 The effective permittivity  $\varepsilon_r(k)$  for capacitive TSF [15], uniform TSF

[16], enhanced TSF [18], and the present TSF, where  $K[\cdot]$  is the complete

elliptic integr defined as  $K[m] = \int_0^1 \frac{1}{(1-t^2)(1-mt^2)} dt$



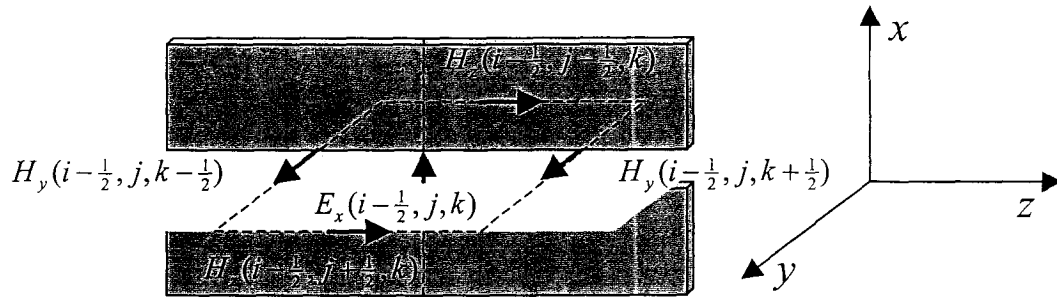


Fig. 4.1 A typical FDTD mesh with cell size larger than the width of slot.

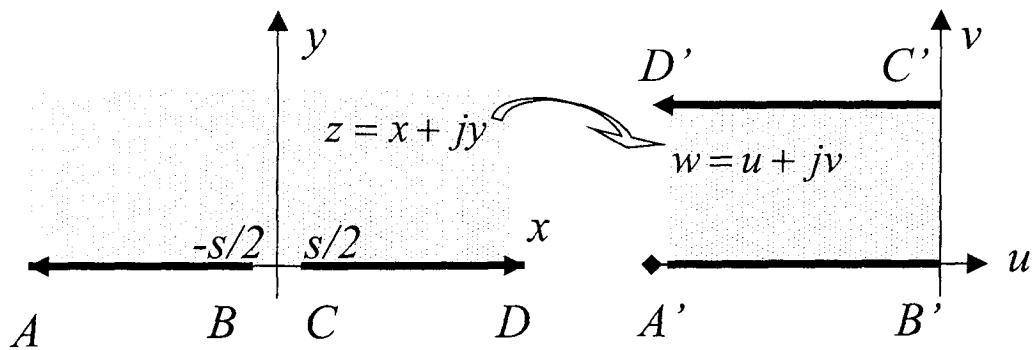


Fig. 4.2 Conformal mapping of a slot-line into semi-infinite parallel planes.

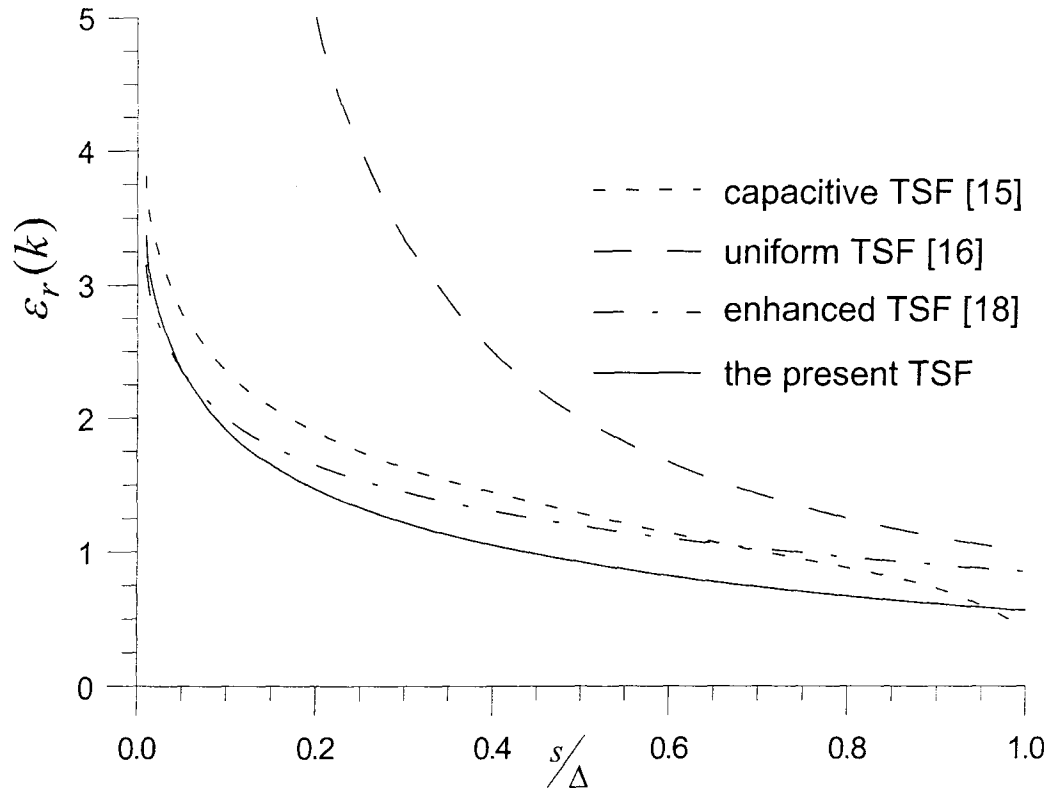


Fig. 4.3 Effective permittivity  $\varepsilon_r(k)$  of different methods verses the  $s/\Delta$  ratio.

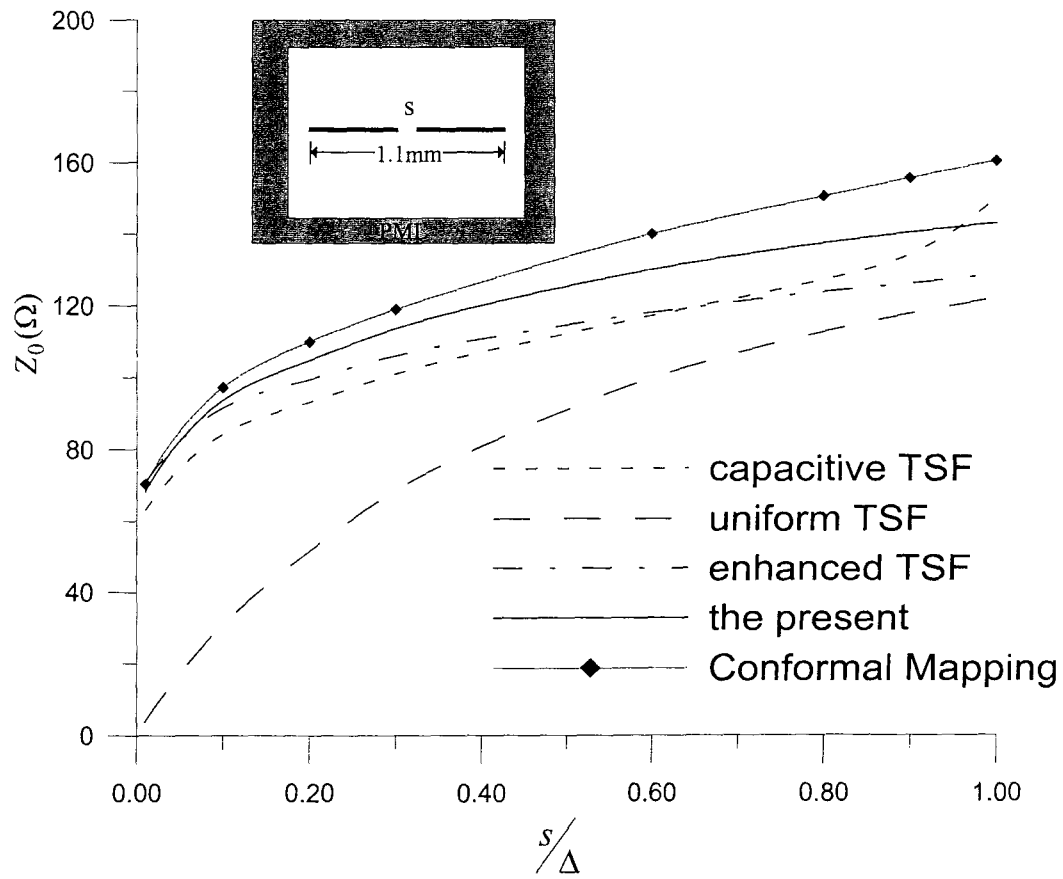


Fig. 4.4 Calculated results for the characteristic impedance of CPS versus  $s/\Delta$  for the slotline shown in the inset.

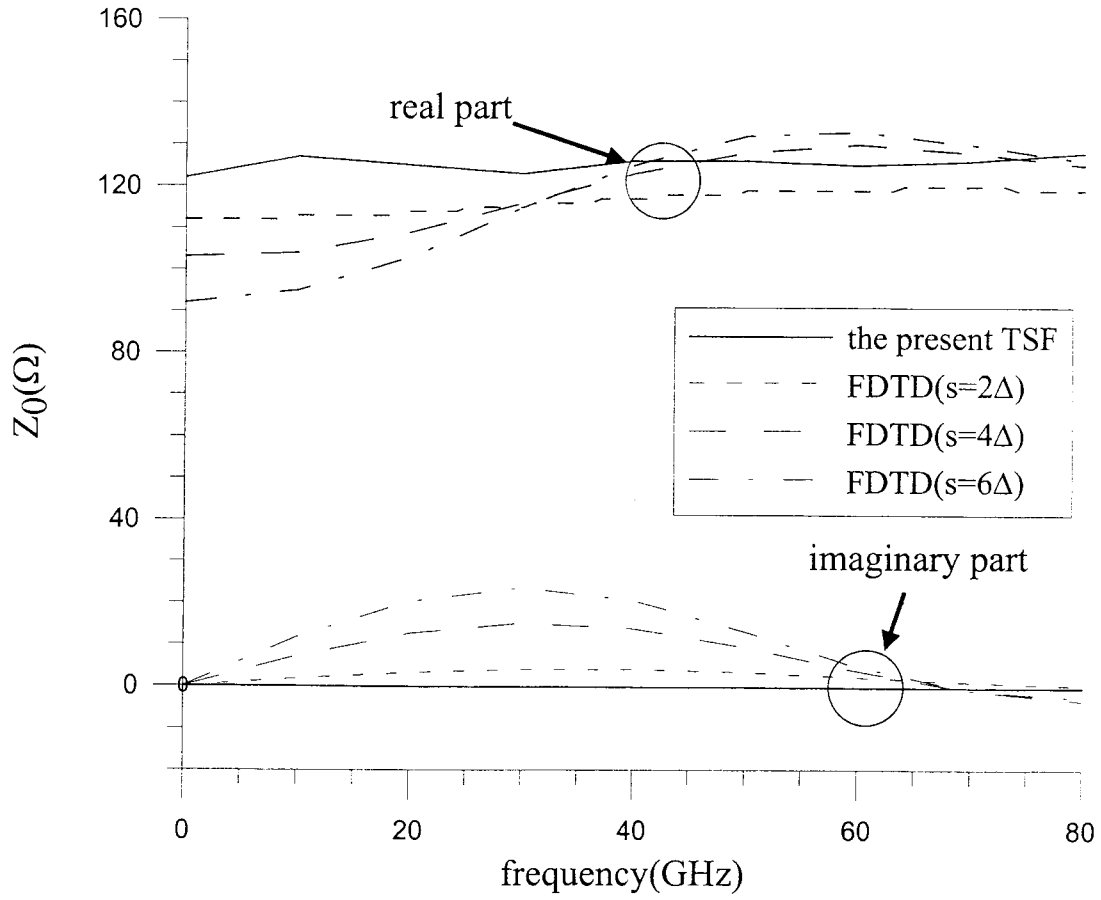


Fig. 4.5 Calculated results for the real and imaginary parts of  $Z_0$  versus frequency by the present TSF for the case of  $s = 0.5\Delta$ . Also shown for comparison are the results obtained by traditional FDTD with the slot divided into 2, 4, and 6 cells, respectively.

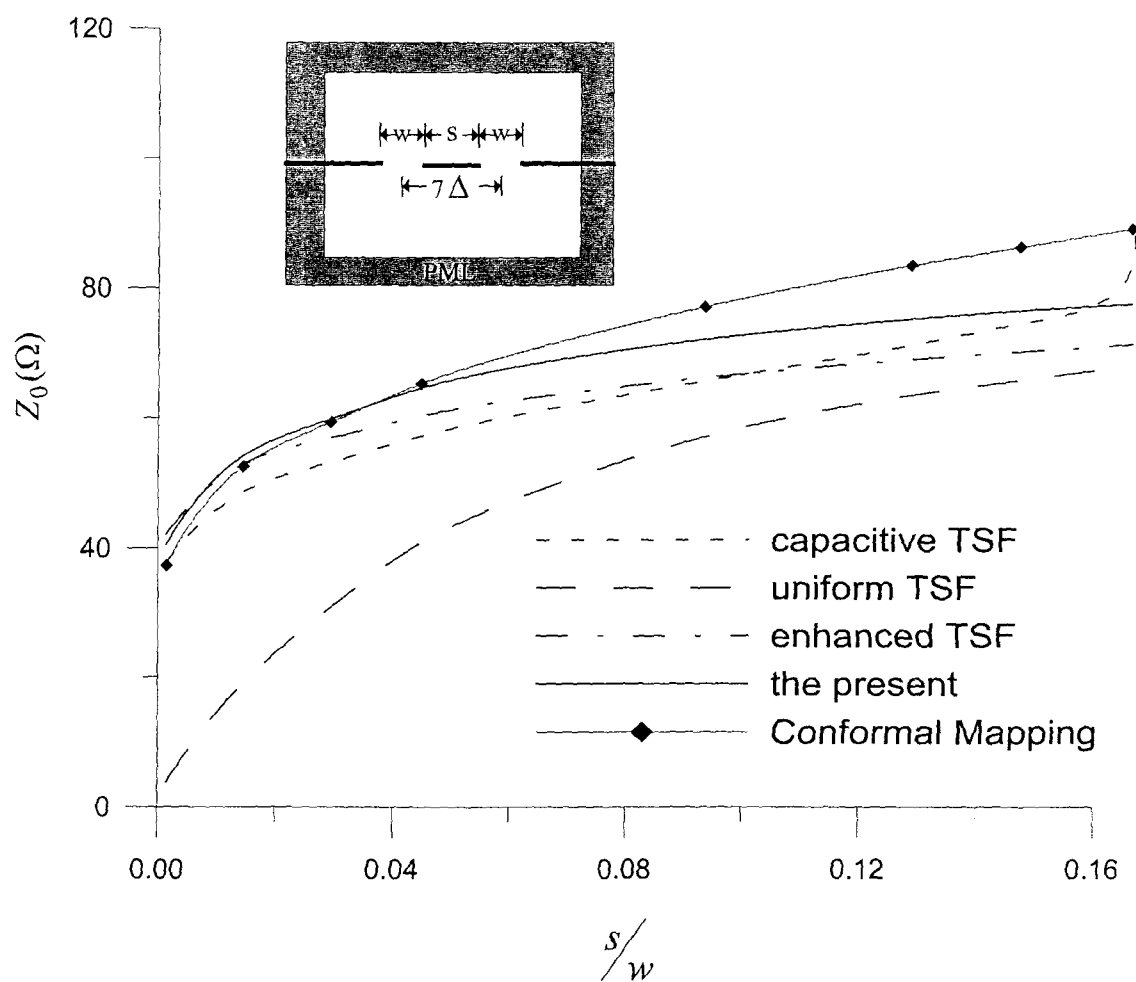


Fig. 4.6 Calculated results for the characteristic impedance  $Z_0$  versus  $s/w$  for the coplanar waveguide shown in the inset.

## Chapter 5

# Composite Effects of Reflections and Ground Bounce for Signal Line through a Split Power Plane

### 5.1 Introduction

In a multi-layered printed circuit board (PCB) or multi-chip module (MCM), it is common practice to cut a slot in the ground or power plane. For example, cutting a power plane into several areas provides multiple power distribution. Another is isolated power or ground plane area, called power island which isolates a noisy or sensitive circuit from other circuits [50]. However, signal lines have to cross the slots in order to communicate between different areas. Thus, incurred are two major signal integrity concerns: the reflection due to the discontinuity in signal return path and the ground bounce which is the voltage fluctuations between power and ground planes.

Traditionally considered to be mainly due to the electric current along vias, the ground bounce can be caused as well by the equivalent magnetic current flowing through the slot on the power or ground planes. As ground bounce noise generated either by other vias or slots in power/ground planes propagate across the slots, it will in turn induce noise voltage on slot and then couple into signal lines. To accurately model the propagation characteristics of signal traces over slot, the composite effects of signal reflection and ground bounce must be taken into account in view of the increasing complexity of the routing and the necessity of multiple power distribution.

The isolation of island has been discussed using the three-dimensional full wave solvers based on FDTD method [23] or mixed potential integral equations [51], but signal lines are not included and this method requires long computation time and substantial computer memory. In another point of view, the microstrip/slot coupling has been analyzed using transmission line model and equivalent circuit for mode conversion [20], but neglecting the presence of ground bounce between power and ground planes.

In this chapter, we propose a new efficient analysis scheme which consists of the two-dimensional FDTD method for radial wave propagation of ground bounce, the transmission line theory for signal propagation along microstrip and slotlines, and especially, an equivalent circuit for the coupling between ground bounce and signals

along the slot. The FDTD and transmission line simulations can be performed separately and linked together at each computation time step. The effects of the slot on signal propagation are thus characterized.

## 5.2 Theory and Circuit Modeling

Consider a three-layered structure shown in Fig. 5.1 in which the first layer is a microstrip line, the second layer is a power plane cut with a finite slot, and the third is a ground plane. A voltage source is impressed on the microstrip line which is terminated by a resistance of  $R_L$ . The whole structure can be divided into two regions, one between the microstrip line and power plane, and the other between parallel metal planes with a split on one plane. Since the separation between two metal planes is typically much smaller than the wavelength and the size of the planes, the fields inside can be assumed to be uniform along the  $z$ -direction. Consequently, the electromagnetic fields are functions of  $x$  and  $y$  and consist of  $E_z$ ,  $H_x$ , and  $H_y$  only.

They are commonly called ground bounce and can be solved by the two-dimensional FDTD method [52].

The voltage and current waves will propagate along the microstrip line as well as the slotline formed by the cut on power plane. They are modeled as transmission lines governed by the telegrapher's equation. Without loss of generality, assume that the slotline is positioned along  $x = x_0 \equiv (i_0 + \frac{1}{2})\Delta x$  while the microstrip line is along  $y = y_0 \equiv j_0\Delta y$ . Let  $V_{\mu\text{strip}}(x, t)$  and  $I_{\mu\text{strip}}(x, t)$  denote the voltage and current waves along the microstrip line, while  $V_{\text{slot}}(y, t)$  and  $I_{\text{slot}}(y, t)$  denote the voltage and current waves along the slotline. Mode conversion will happen at the cross-junction of microstrip line and slotline.

Fig. 5.2(a) shows the equivalent circuit for the microstrip line. Due to the mode conversion, the circuit is subject to an equivalent voltage source which is equal to the slotline voltage at the cross-junction [20]. Using central difference discretization to the telegrapher's equation, the voltage and current waves along the microstrip line satisfy

$$C_{\mu\text{strip}}\Delta x \frac{\partial}{\partial t} V_{\mu\text{strip}}(i\Delta x, t) = I_{\mu\text{strip}}((i - \frac{1}{2})\Delta x, t) - I_{\mu\text{strip}}((i + \frac{1}{2})\Delta x, t) \quad (5.1a)$$

$$L_{\mu\text{strip}}\Delta x \frac{\partial}{\partial t} I_{\mu\text{strip}}((i + \frac{1}{2})\Delta x, t) = V_{\mu\text{strip}}(i\Delta x, t) - V_{\mu\text{strip}}((i + 1)\Delta x, t) - V_{\text{slot}}(j_0\Delta y, t)\delta_{i, i_0} \quad (5.1b)$$

Here,  $C_{\mu strip}$  and  $L_{\mu strip}$  are per-unit-length capacitance and inductance, respectively, of the microstrip line. They can be obtained by solving a two-dimensional Laplace problem [53].

The equivalent circuit for the slotline is shown in Fig. 5.2(b). The equivalent current source density should include not only the term  $I_{\mu strip}(x_0, t)$  at cross-junction to account for the discontinuity in the return current path for microstrip line as described in [20] but also the term  $H_{y, FDTD}(x_0, y, t)$  along the whole slot for the coupling due to the ground bounce propagating in the underlying parallel-plate region. The telegrapher's equation for slotline should thus be modified as

$$C_{slot} \Delta y \frac{\partial}{\partial t} V_{slot}(j \Delta y, t) \cong -I_{slot}((j + \frac{1}{2}) \Delta y, t) + I_{slot}((j - \frac{1}{2}) \Delta y, t) + I_{\mu strip}((i_0 + \frac{1}{2}) \Delta x, t) \delta_{j, j_0} - H_y((i_0 + \frac{1}{2}) \Delta x, j \Delta y, t) \Delta y \quad (5.2a)$$

$$L_{slot} \Delta y \frac{\partial}{\partial t} I_{slot}((j + \frac{1}{2}) \Delta y, t) = V_{slot}(j \Delta y, t) - V_{slot}((j + 1) \Delta y, t) \quad (5.2b)$$

Here,  $L_{slot}$  and  $C_{slot}$  are the per-unit-length inductance and capacitance of slotline in the presence of power/ground planes, and  $H_y$  is the magnetic field in  $y$  direction under slotline in the region between power/ground planes.

In the region between two metal planes, the FDTD mesh inclusive of slotline is shown in Fig. 5.3. The voltage on slotline will act as equivalent magnetic current and couple energy into the region between power/ground planes. Thus, the updating for magnetic field in  $y$  direction must be rewritten as

$$\mu \frac{\partial}{\partial t} H_y((i + \frac{1}{2}) \Delta x, j \Delta y, t) \Delta x \cdot d = [E_z((i + 1) \Delta x, j \Delta y, t) - E_z(i \Delta x, j \Delta y, t)] d + V_{slot}(j \Delta y, t) \delta_{i, i_0} \quad (5.3)$$

The updating equations for all the other field quantities remain the same as those in conventional FDTD scheme and are omitted here.

The time marching can be briefly described as follows. The voltages  $V_{\mu strip}$  and  $V_{slot}$  can be updated from  $I_{\mu strip}$ ,  $I_{slot}$ , and  $H_y$  by (5.1a) and (5.2a). In the next



half time step,  $I_{\mu\text{strip}}$ ,  $I_{\text{slot}}$ , and  $H_y$  can be updated from  $V_{\mu\text{strip}}$ ,  $V_{\text{slot}}$ , and  $E_z$  with the help of (5.1b), (5.2b), and (5.3). Therefore, the coupling effect between slotline and power/ground planes is addressed. The composite effects of reflection and ground bounce among the whole structure can be modeled.

### 5.3 Numerical Simulation

Take the structure of a 10 cm  $\times$  10 cm PCB shown in Fig. 5.1 as an example. The heights of signal layer and power/ground planes are  $h = 635 \mu\text{m}$  and  $d = 150 \mu\text{m}$ , respectively, and the dielectric constant is both 9.7. The widths of microstrip line and slotline are  $570 \mu\text{m}$  and  $50 \mu\text{m}$ , respectively, and the length of slotline is 4 cm. In numerical simulation, the FDTD region between the two planes is divided into  $100 \times 100$  cells of cell size  $\Delta x = \Delta y = 1 \text{ mm}$ . The signal voltage source is a Gaussian pulse generator in series with an internal resistance of  $R_g = 50 \text{ ohm}$  between the top microstrip line and the second layer. On the other end of the signal line, a matched load ( $R_L = 50 \Omega$ ) is connected between the bottom microstrip line and the third layer. The top view of Fig. 5.1 is shown in Fig. 5.4, where points a, b, and c are separated from the shorted end of the slotline by 1, 10, and 20 mm, respectively, and d is  $\Delta x$  in front of the cross-junction.

The voltages at points A and B are monitored and the waveforms are shown in the upper figure of Fig. 5.5, while the voltages at points a, b, and c are shown in the middle figure, and the ground bounce on the bottom two planes at point d are shown in the lower figure. In the middle figure, as the signal propagates along the slot, it decays continually due to the energy coupling onto the power/ground planes. At late time, the ground bounce that is reflected by the boundary of the metal planes couples into the slotline and this causes some noise on the microstrip line as shown in the upper figure.

When the separation of power/ground planes is changed to  $300 \mu\text{m}$  and  $500 \mu\text{m}$ , the voltage waveforms at point A are shown in the inset of Fig. 5.6, and the reflected signals are enlarged to have a closer look. As the separation increases, energy coupled into the power/ground planes will decrease and the noise on the microstrip line will increase.

### 5.4 Experimental Validation

A test four-layered PCB with two slots is fabricated to investigate the coupling between two signal lines by slot-induced ground bounce. As in Fig. 5.7, the first and

fourth layers are signal planes with open-circuited microstrip lines at the center of the test board. The second and third layers are power plane/ground planes, both having a slot on it. The center of the slot is located just under the microstrip line and its direction is transverse to the direction of the microstrip line. Other geometric parameters can be found from Fig. 5.7(a), while the substrate material is of dielectric constant  $\epsilon_r = 4.3$  and thickness of 1.5 mm in each layer.

The whole structure is anti-symmetric for the upper two layers and lower two layers. Note that the second layer serves as the ground plane for the microstrip line on port 1 and the third layer serves as the ground plane for port 2. There are no vias in this structure. The ground bounce, if generated, could be contributed to the presence of the slots.

In the experiment, a ramped step pulse of about 100 ps rise time is used as the excitation on port 1. The TDR and TDT signals at point 1 and 2, respectively, are measured by Tektronix 11801C. When the signal propagates down the microstrip line, part of its return current path will be blocked by the slot. Ground bounce will be generated and propagates in the region between the second and third layers. It will bounce back and forth due to the presence of the finite boundary of the metal planes. When the ground bounce encounters the slot on the third layer, some energy will be picked up by the signal line on port 2 to appear as the coupled noise.

In numerical simulation, the measured input waveform is used as the excitation signal. The slotline is modeled as a transmission line with governing equations in (4.2a) and (4.2b). The equivalent inductance and capacitance of the slotline embedded in this structure is calculated by applying the integral equation method [54]. The value of inductance is calculated to be 317 nH/m, and capacitance 117 pF/m.

Fig. 5.8 shows the result of simulation and experiment. In the present case that the step voltage of the signal is 0.25 volts, the peak-to-peak coupled noise level of port 2 is measured to be 33 mV as compared to the simulated value of 48 mV. In other words, the generated coupled noise by the ground bounce due to the slots may achieve about 15% of the input level. The over-estimation in the simulated level can be contributed to the negligence of the loss by the substrate, conductor, and radiation in the simulation.

By taking Fourier transform of the time-domain responses, Fig. 5.9 shows the power spectrum density of the input signal, and the simulated and measured signals on port 2. Noticeable in the power spectrum are some peaks which correspond to the resonant modes in the parallel-plate region of size 8 cm  $\times$  6 cm. It is not difficult to derive that the resonant  $TM_{mn}$  mode has the field pattern

$$E_z(x, y) \propto \cos \frac{m\pi x}{a} \cos \frac{n\pi y}{b} \quad (5.4)$$

current distribution on the metal plane

$$\bar{J}(x, y) \propto \hat{x} \frac{m\pi}{a} \sin \frac{m\pi x}{a} \cos \frac{n\pi y}{b} + \hat{y} \frac{n\pi}{b} \cos \frac{m\pi x}{a} \sin \frac{n\pi y}{b} \quad (5.5)$$

and resonant frequency

$$f_{mn} = \frac{c}{2\sqrt{\epsilon_r}} \sqrt{\left(\frac{m}{a}\right)^2 + \left(\frac{n}{b}\right)^2} \quad (5.6)$$

Based on (5.6), the first peak in Fig. 5.9 is  $TM_{10}$  mode at 0.9 GHz. However, only some of the resonant modes will be visible. Since the present structure together with the excitation is symmetric with respect to  $y$ , all the  $TM_{mn}$  modes with odd  $n$  will not be excited. Furthermore, the slotlines are located at  $x = a/4$  and  $x = 3a/4$ . They will not excite the resonant modes with  $m=4k$ , for which the modal current in (5.5) has no  $x$  component to cut into the slotline. Thus, the second excited resonant mode will be  $TM_{20}$  at 1.8 GHz, shown in both the measurement and simulation. The next excited resonant modes are  $TM_{12}$  at 2.6 GHz and  $TM_{30}$  at 2.7 GHz, which appear only as one peak for lack of the resolution.

In addition to the resonant parallel-plate modes, both simulation and measurement exhibit a slotline mode near 2.4 GHz. This can be contributed to the standing wave by the reflection back and forth in the simulation. The agreement between measurement and simulation deteriorates as the frequency becomes higher. Since electromagnetic effects neglected in the present method may become significant, such as the radiation from the open boundary of parallel plates and from the short-end of slotline, the dispersion of microstrip line and slotline, frequency-dependant skin-effect loss of the metal, and so on. It exhibits that the simulation tends to over estimate the high-frequency components which are subject to larger attenuation due to the electromagnetic effects.

The same structure is measured by HP 8510C. Fig. 5.10 shows the results of  $S_{21}$  related to frequency for both simulation and experiment. The Gaussian pulse is used as the excitation for numerical simulation. Both time-domain and frequency-domain measurements show the same results. The first peak is  $TM_{10}$  mode at 0.9 GHz, the second peak is  $TM_{20}$  at 1.8 GHz, the slotline mode appears at 2.4GHz and the third peak is  $TM_{12}$  at 2.6 GHz.

Fig. 5.11 shows the simulation results of TDT signals on port 2 versus the different widths of slot. The peak-to-peak voltages are 48 mV, 52 mV, and 58 mV with respect to slot widths: 0.3 mm, 0.6 mm, and 0.9 mm. The larger the slot width, the higher the TDT voltage level.

## 5.5 Summary

A new modeling scheme is proposed in this chapter to simulate the signal integrity issues due to signal lines flowing above split power and ground planes. The slot on the split planes is treated as a transmission line, and through slot the energy in the signal line can be coupled to cause ground bounce in the parallel-plate region and vice versa. The contributions of the coupling can be cast into the transmission lines as equivalent sources so that the composite effects of reflection, ground bounce, and signal coupling can be simulated very efficiently in the time domain by combining one-dimensional transmission line and two-dimensional FDTD analyses. Simulation and measurement are performed to characterize the slot-induced ground bounce.

Although ground bounce caused by a single slot coupling is only about 5% of input signal, the effects cannot be ignored as multi-trace signal flows through the slot simultaneously. Both simulation and experiment show that the slot induced bounce may result in significant coupled noise on distant quiet signal line with peak-to-peak noise voltage exceeding 15% of the input signal level.

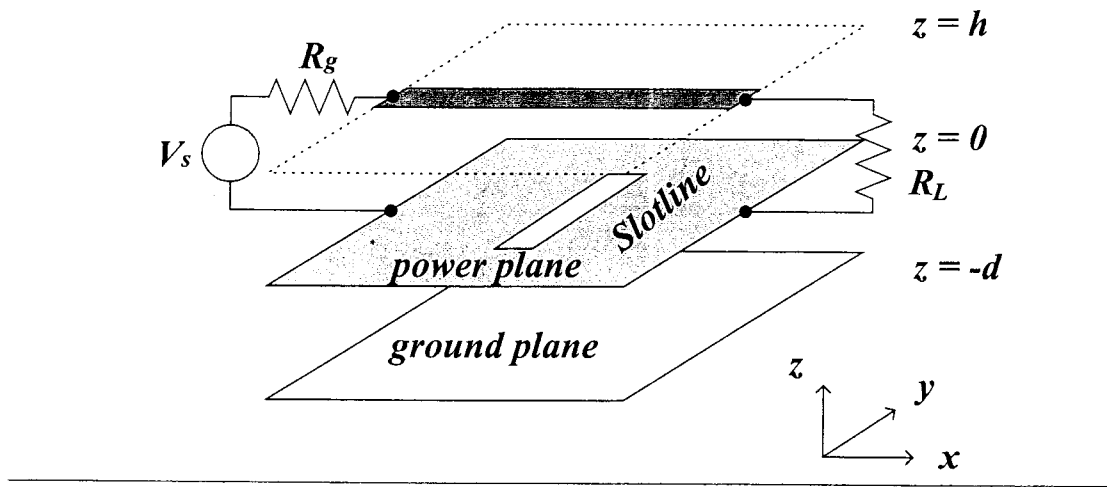


Fig. 5.1 A simple multi-layered structure with split power plane.

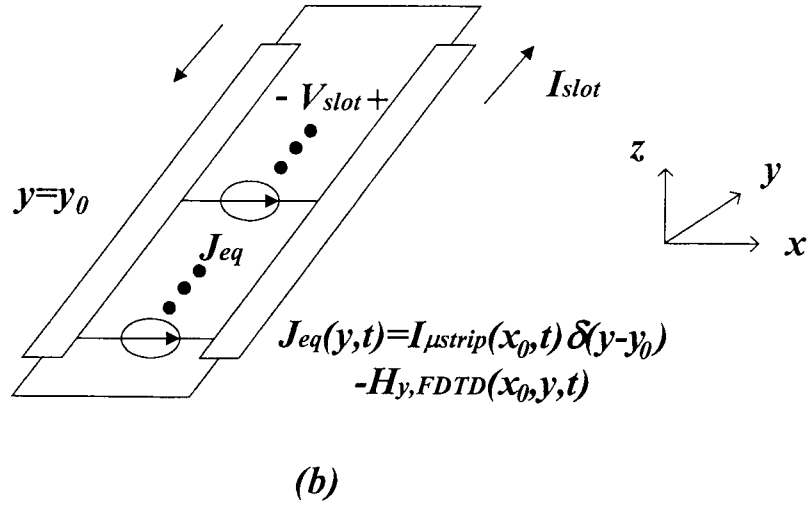
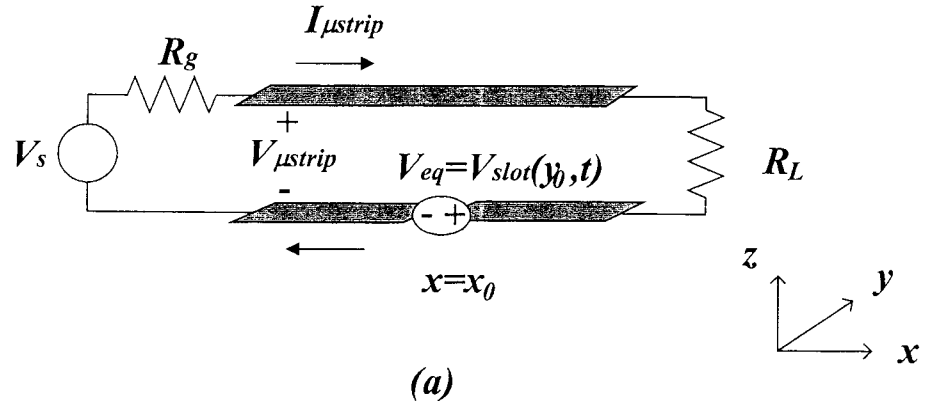


Fig. 5.2 Equivalent circuits at cross-junction for (a) microstrip line and (b) slotline.

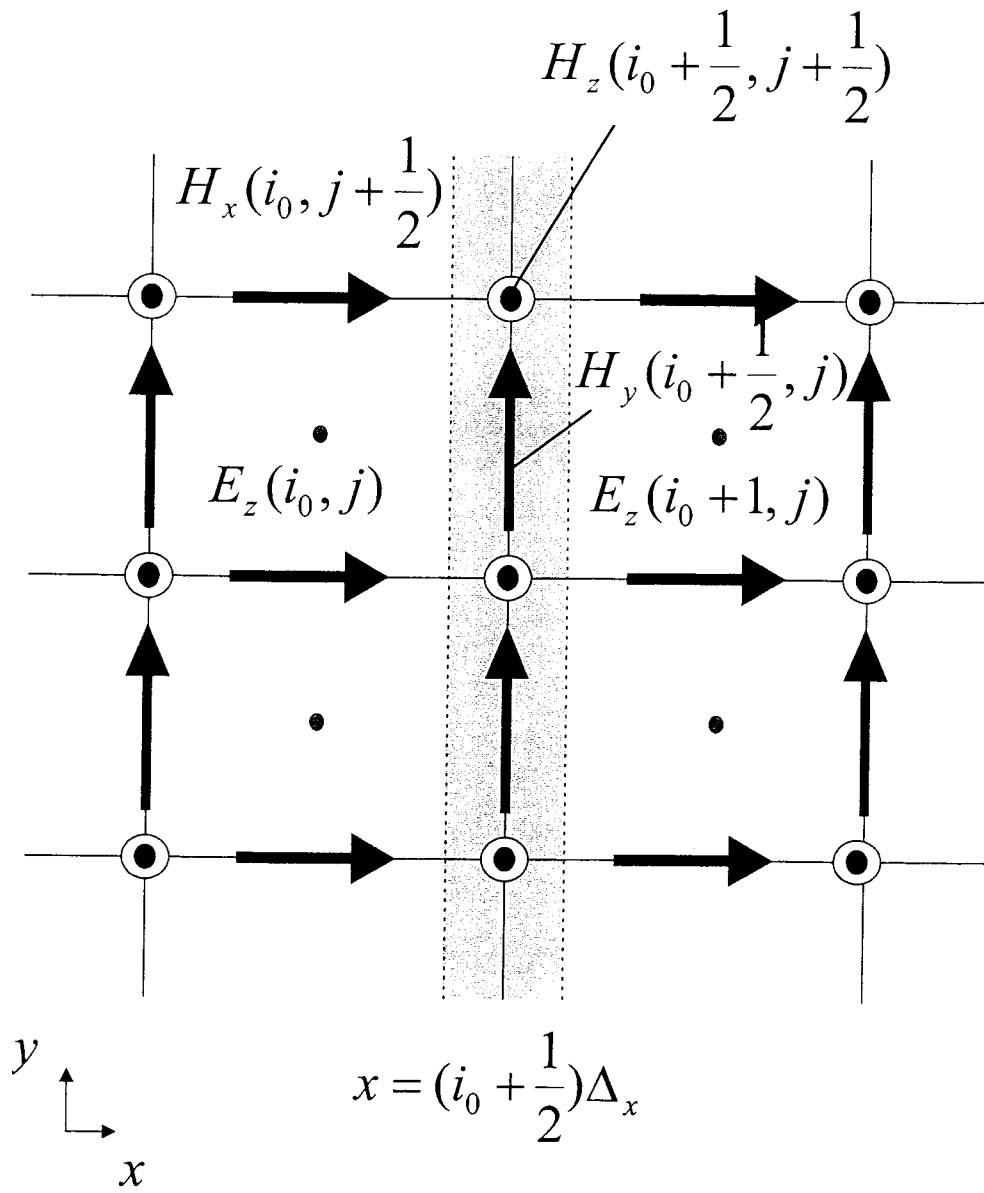


Fig. 5.3 FDTD mesh inclusive of slotline. Here,  $E_z(i, j)$  is a short-hand notation for  $E_z(i\Delta_x, i\Delta_y, t)$  and similarly for  $H_x$ ,  $H_y$ , and  $H_z$ .

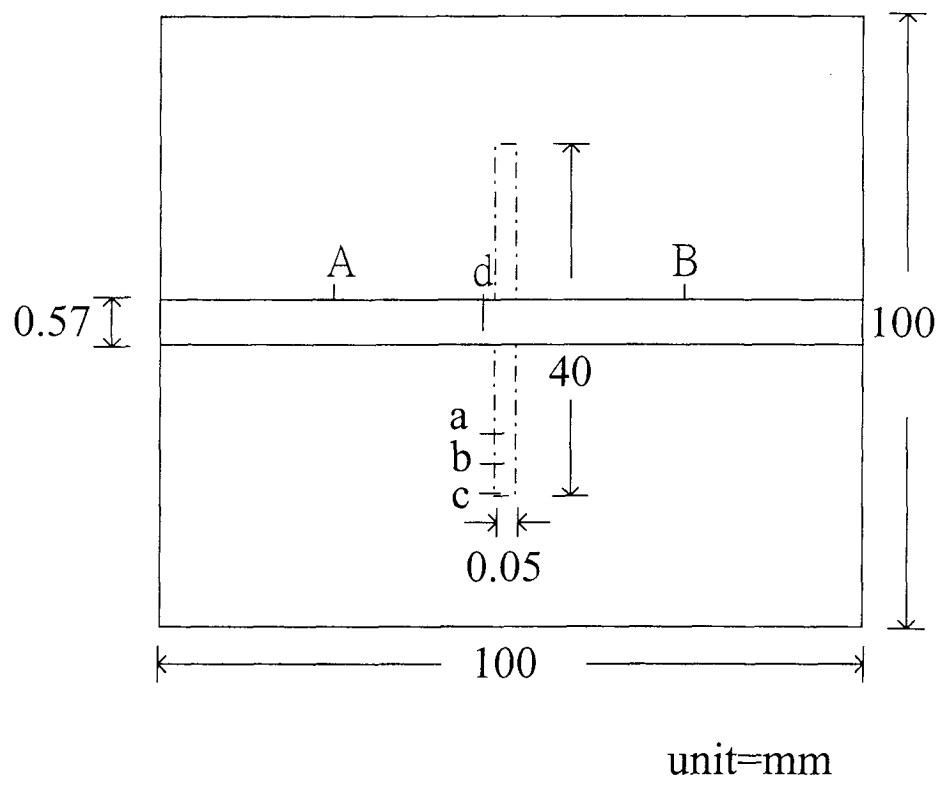


Fig. 5.4 Top view of Fig. 5.1.



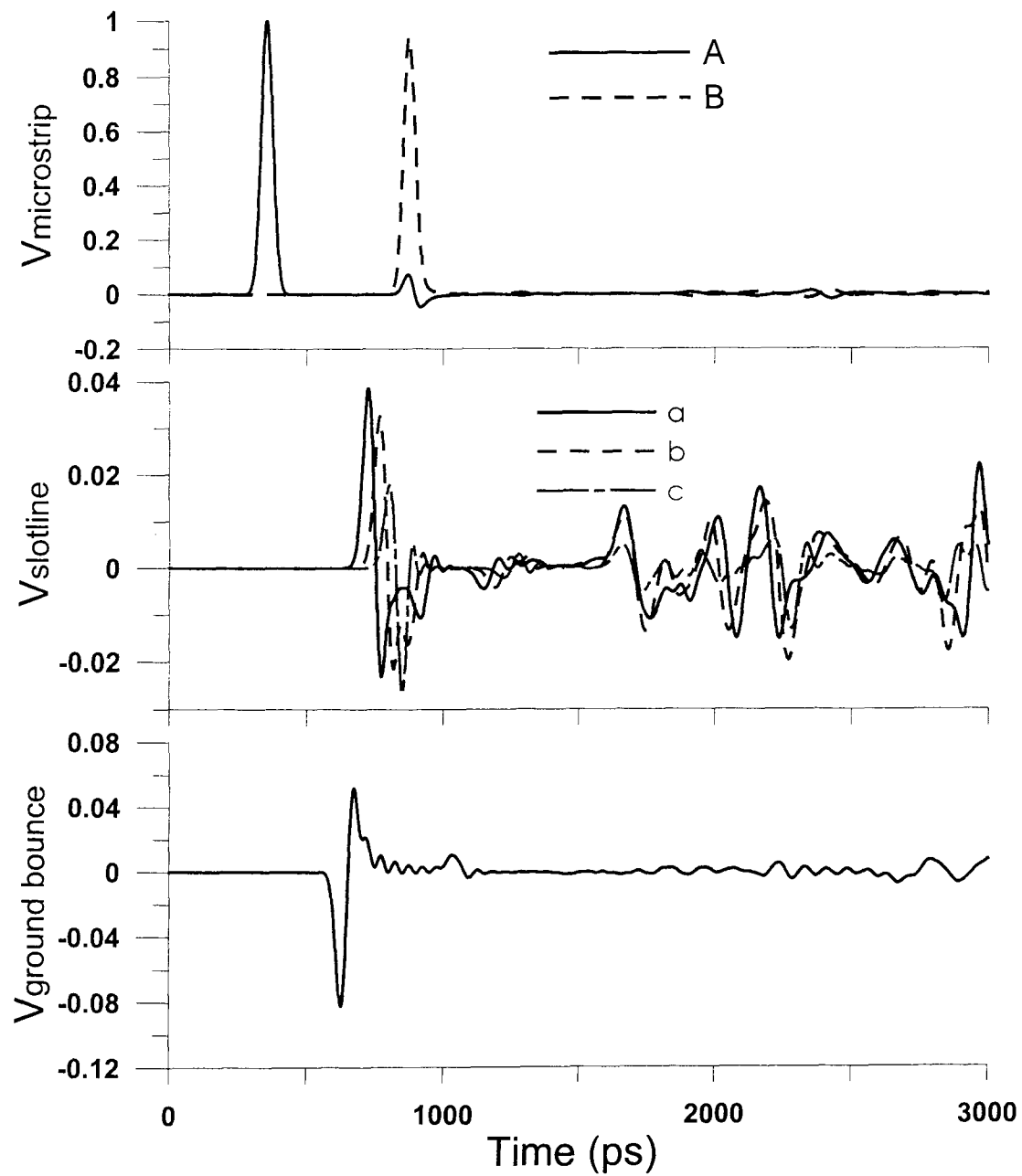


Fig. 5.5 Voltages at A, B on microstrip line (upper figure), and voltages at a, b, c on slotline (middle figure), and ground bounce near slotline (lower figure).

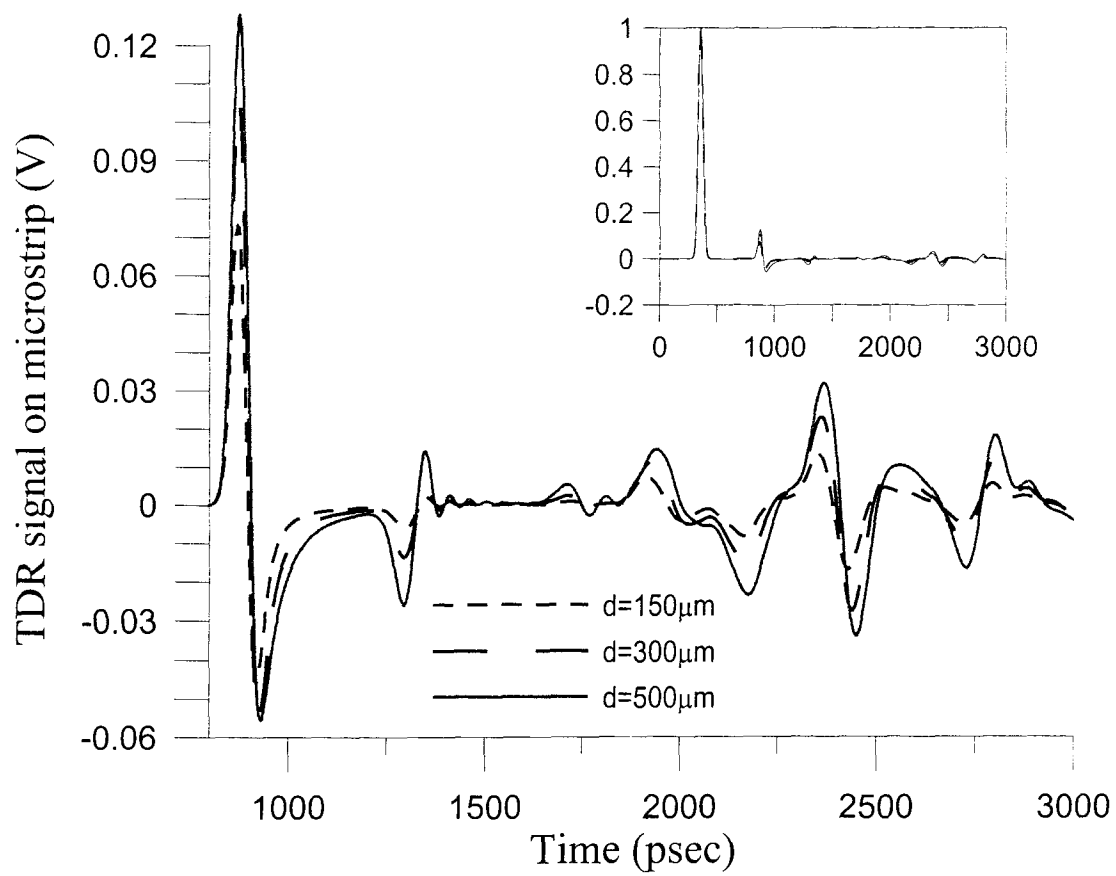


Fig. 5.6 Comparison of voltage at A with different separation of power/ground planes as a parameter.

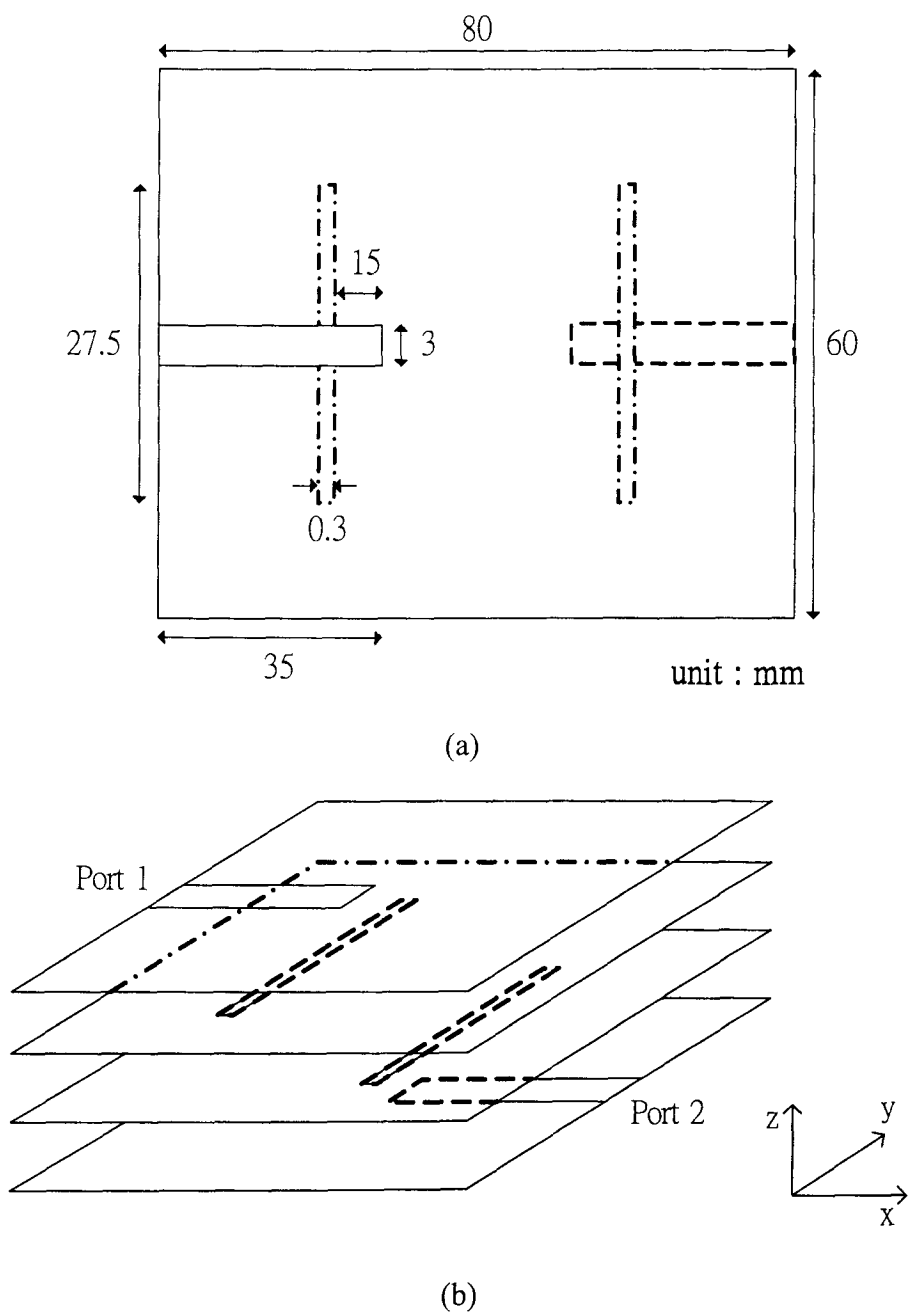


Fig. 5.7 A test PCB used for experiment and simulation to depict the slot-induced ground bounce: (a) top view and (b) side view.

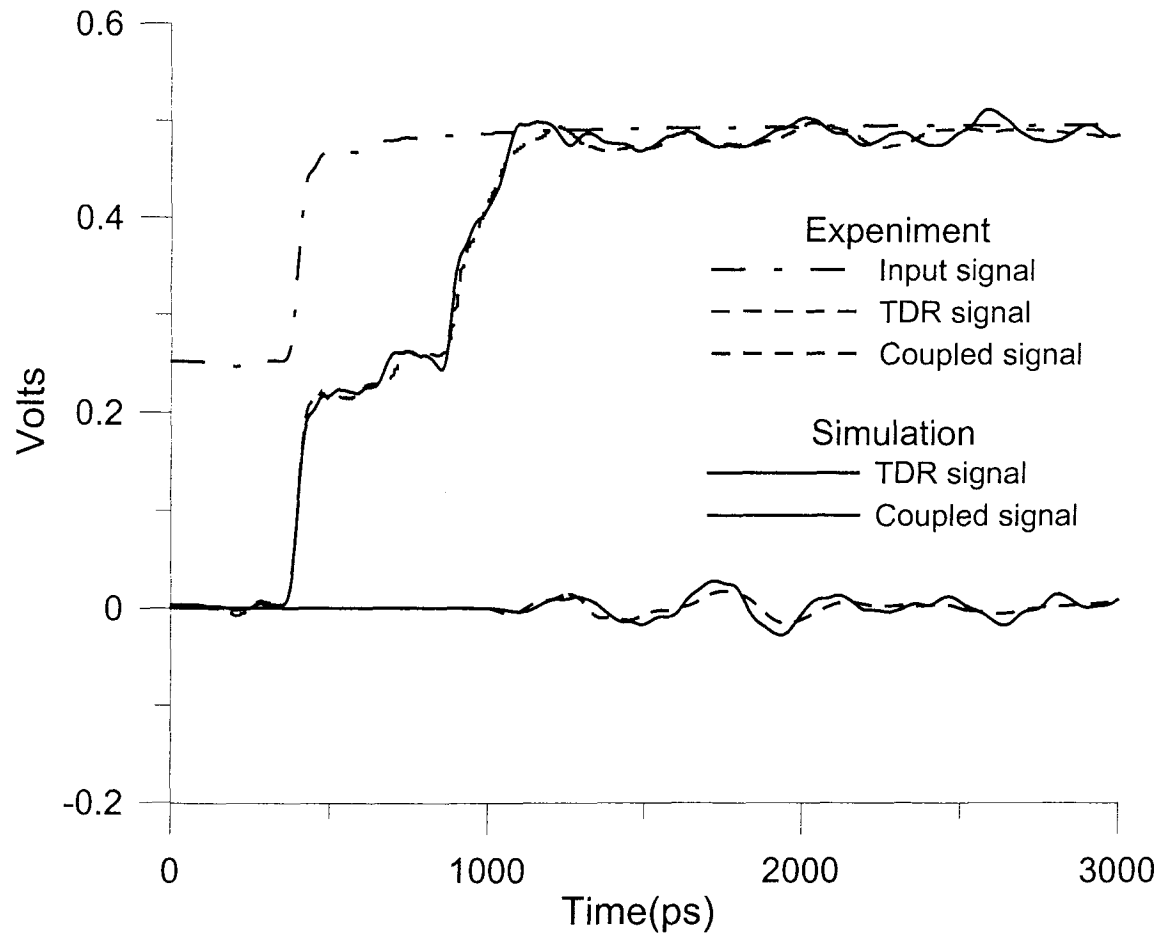


Fig. 5.8 Measured and simulated waveforms of the TDR signal on port 1 and TDT signals on port 2 for the test setup in Fig. 5.7.

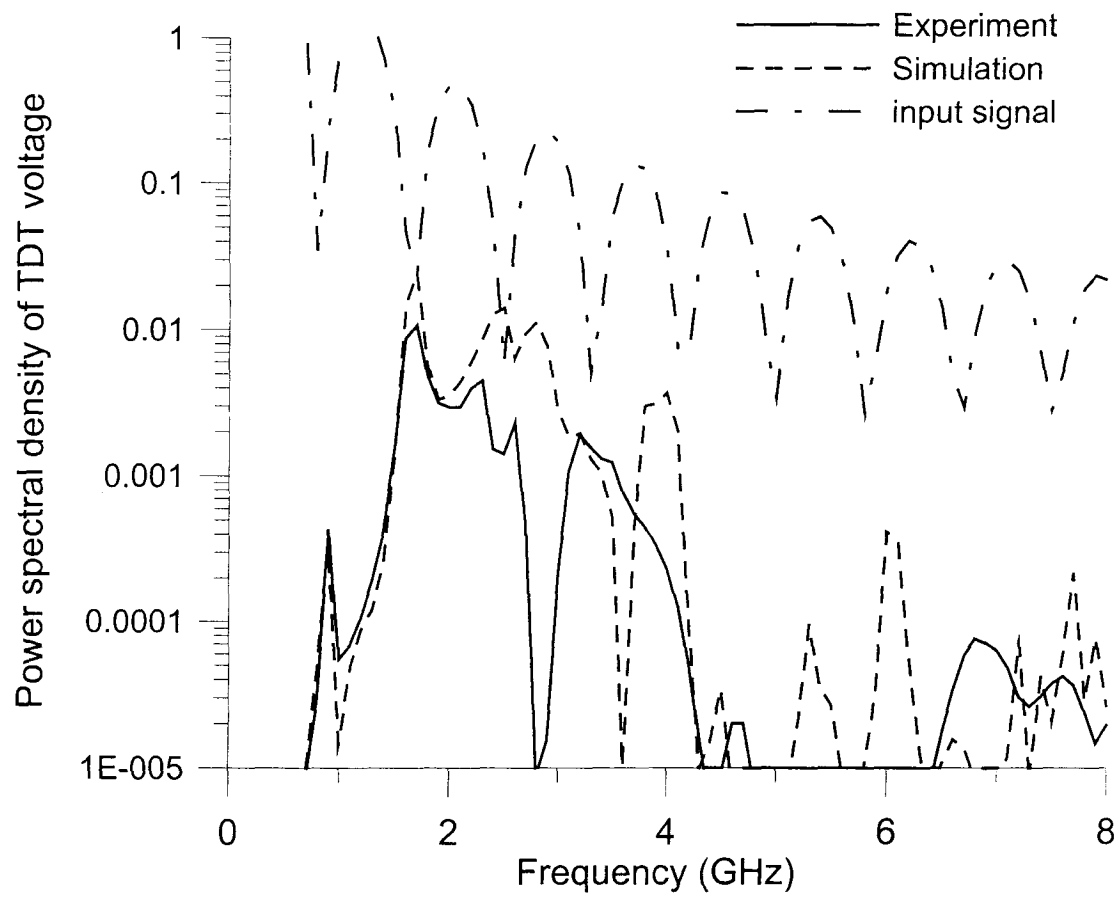


Fig. 5.9 Power spectral of the input signal, and the simulated and measured output signals.

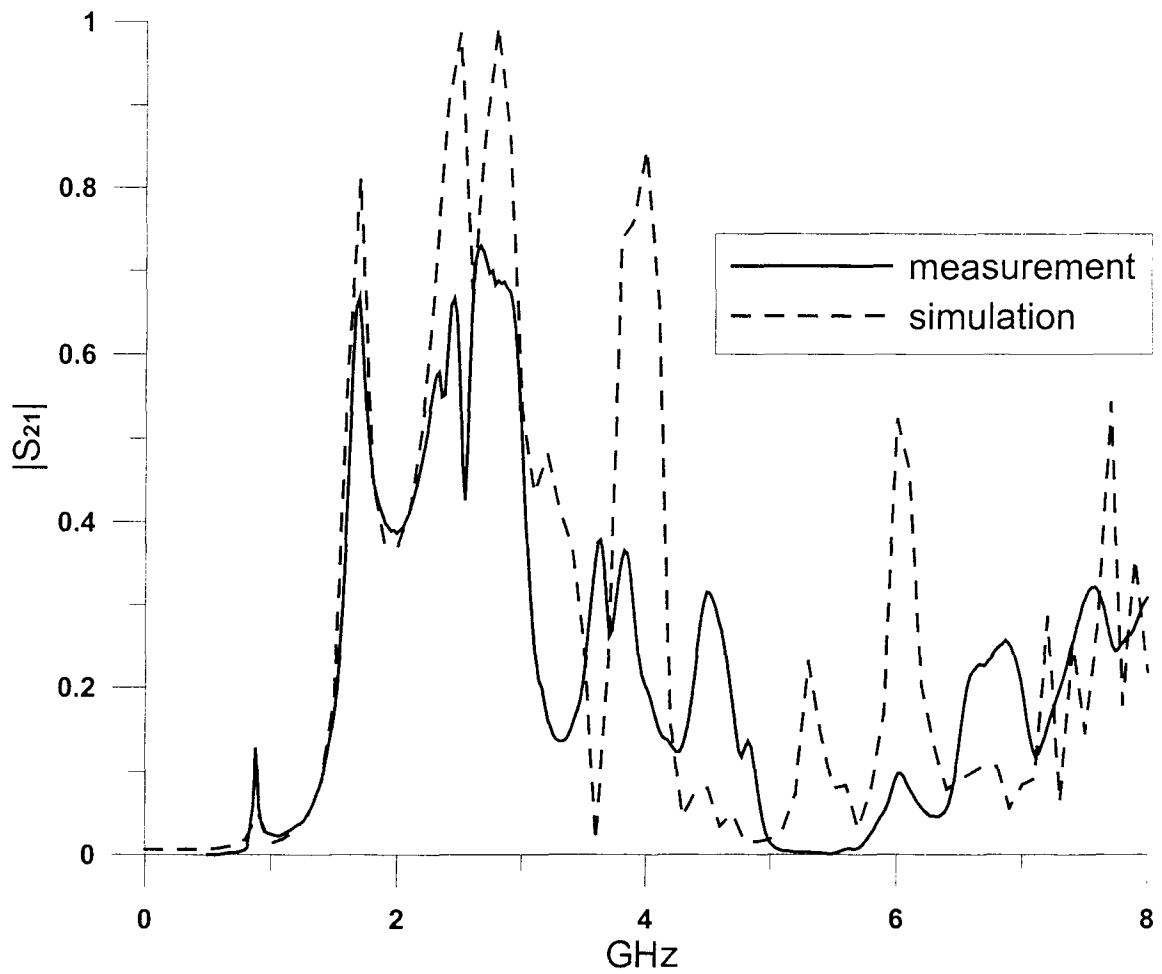


Fig. 5.10  $S_{21}$  of the simulation and measurement. The measurement is done by HP8510C.

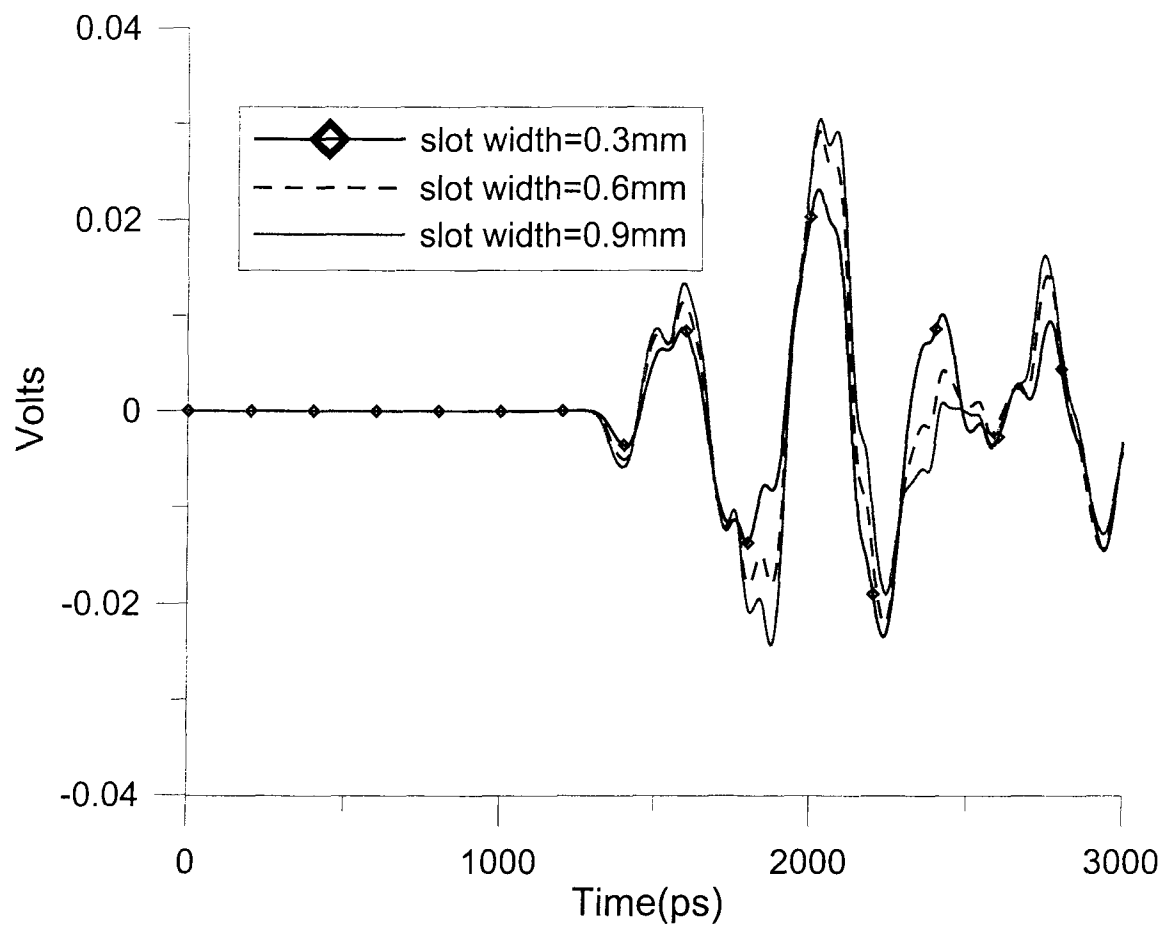


Fig. 5.11 Simulation results of TDT signals on port 2 versus the different widths of slot.

## Chapter 6

### Hybrid TIE/FDTD Method for Open Boundary

#### Coupling between Isolation Islands

##### 6.1 Introduction

In multi-layer structures, the signal crossing the slot will excite the parallel plate modes which exhibit as ground bounce between the power and ground planes. Mode conversion happens among microstrip mode, slotline mode, and the parallel plate mode. In the previous chapter, an efficient model based on equivalent circuits and two-dimensional FDTD analysis has been successfully established to simulate this complicated mode conversion mechanism.

In addition to slots, there are many vias between two parallel plates to serve for the signal and/or power transmission in the vertical direction. Extensive studies have been presented in the literature and most of them focus on the ground bounce excited and coupled due to the presence of the vias. In light of the narrow separation between the parallel plates, an efficient approach based on two-dimensional FDTD method is possible for practical problems of thousands of vias [52]

In reality, the power and ground planes in PCBs must be finite in size. The edges of the finite-size plate will not only cause signal reflection but also radiation. It can serve as EMI source as well as receptor. For structures with isolated power islands, the coupling among the edges may become a major source of noise and should be taken into account. As a result, mode coupling and conversion in terms of parallel plate mode will happen among discontinuities of vias, slots in split plane, and edges of the finite-size plates [22]

The complicated mode conversion mechanism has been investigated using the three-dimensional FDTD method [22]-[24]. However, the packaging structures usually include elements of drastically different scales, say, the microstrip and slotline are usually very narrow as compared with the parallel plate. The FDTD method is usually incapable of accurately modelling the structure details and if so, will need long computation time and large computer memory. On the other hand, structures of different scales could be modelled much more powerfully by integral-equation based methods, like MPIE [51] and PEEC [55], [56]. However, modeling of the finite-size



plates in PEEC calls for a great number of unknowns associated with a full matrix, which will easily exhaust the available computer resources. Both methods, although flexible and general, still find difficulty in dealing with practical packaging structures.

In a PCB, the electric field between ground/power planes is uniform in the longitudinal direction except near the edge due to the fringing effects. A more efficient approach should be based on two-dimensional FDTD [52]. However, such an approach usually puts perfect magnetic conductor (PMC) on the edge and neglects the radiation effects. A new efficient analysis scheme is proposed in this chapter. It hybridizes the two-dimensional FDTD method for the ground bounce propagation between parallel plates and the time-domain equivalent circuits for electromagnetic wave radiation/coupling due to the edges of the finite plates. The FDTD and edge opening simulations can be performed separately and linked together at each computation time step. The effects of the open edges along the boundary on signal propagation are thus characterized.

## 6.2 Hybrid TIE/FDTD Method

### 6.2.1 Equivalent problems

Fig. 6.1(a) shows a typical PCB structure with separated power planes of finite size. The ground plane is much larger in size and assumed to be infinite in this paper. Due to the wave leakage from the aperture opening along the boundary, there will be some coupling between the two power islands. It is desired to derive an efficient formulation directly applicable for the time domain analysis.

The problem can be decomposed into an interior open circuit problem and an exterior short circuit problem shown in Fig. 6.1(b) and 6.1(c), respectively. Let  $\vec{s}$  denote the position vector on the boundary surface. In the interior problem, the parallel plates are assumed to be ideally open at the boundary but with the impressed surface current density  $\vec{J}_g(\vec{s}, t) = -\hat{n} \times \vec{H}(\vec{s}, t)$  where  $\hat{n}$  is the unit outwards normal vector and  $\vec{H}(\vec{s}, t)$  is the magnetic field intensity on the boundary surface.

In the exterior problem, the aperture is assumed to be short-circuited but with an equivalent voltage source  $V(\vec{s}, t)$ . The voltage is directly related to the electric field on the plate boundary by  $V(\vec{s}, t) = -d \cdot E_z(\vec{s}, t)$ . Let the resultant magnetic field intensity along the boundary be  $\vec{H}^s(\vec{s}, t)$ . The surface current density flowing across the shorted aperture can be given by  $\vec{J}(\vec{s}, t) = \hat{n} \times \vec{H}^s(\vec{s}, t)$  as shown in Fig. 6.1(c).

According to the field continuity between  $\vec{H}(\vec{s}, t)$  and  $\vec{H}^s(\vec{s}, t)$ , the surface currents in the interior and exterior problems require  $\vec{J}_g(\vec{s}, t) + \vec{J}(\vec{s}, t) = \vec{0}$ . In other words, the total current flow across the aperture is zero, which justifies the equivalence between the original and the equivalent problems.

### 6.2.2 Interior open-circuit problem

Consider the problem in Fig. 6.1(b). In common cases that  $d$  is much smaller than the wavelength and the size of the plate, it is reasonable to assume that the electric field between the parallel plates contains  $E_z(x, y, t)$  component only. In reality, the ground bounce between the parallel plates is measured by

$$V(x, y, t) = -d \cdot E_z(x, y, t) \quad (6.1)$$

The surface current density on the upper plane  $\vec{J}(x, y, t)$  is related to the magnetic field intensity between the two plates by

$$\vec{J}(x, y, t) = -\hat{z} \times \vec{H}(x, y, t) \quad (6.2)$$

Note that the current density on the lower plane is  $-\vec{J}(x, y, t)$ .

From the Maxwell equation between the electric and magnetic fields, it is not difficult to derive the relation between the voltage and surface current density.

Without loss of generality, assume the plate is rectangular and divided into  $N_x \cdot N_y$

small cells of size  $\Delta_x \times \Delta_y$ . The relation can be more physically written in terms of

the equivalent LC network [57] as shown in Fig. 6.2. The capacitance and inductance in the network are given by

$$C_{FDTD} = \frac{\epsilon \Delta_x \Delta_y}{d}; \quad L_{FDTD}^x = \frac{\mu d \Delta_x}{\Delta_y}; \quad L_{FDTD}^y = \frac{\mu d \Delta_y}{\Delta_x} \quad (6.3)$$

For the nodal voltages along the boundary, the impressed current source should be accounted for to model the electromagnetic coupling and/or radiation from the open edge. They satisfy the following form

$$\kappa C_{FDTD} \frac{d}{dt} V(\vec{s}, t) = I_{FDTD}^{inc}(t) - I_g(\vec{s}, t) \quad (6.4)$$

Here,  $\kappa$  is the area fill factor. The value is  $\kappa = \frac{1}{2}$  for the node along the “straight” part of the boundary, while  $\kappa = \frac{1}{4}$  for the node at the corner. The term  $I_{FDTD}^{inc}(t)$  denotes sum of the current in the interior problem injected to the node. Say, for the node  $\vec{s} = (x_{N_x}, y_j)$  on the right side of the boundary shown in Fig. 6.2,

$$I_{FDTD}^{inc}(t) = I^x(x_{N_x - \frac{1}{2}}, y_j, t) + I^y(x_{N_x}, y_{j - \frac{1}{2}}, t) - I^y(x_{N_x}, y_{j + \frac{1}{2}}, t) \quad (6.5)$$

The impressed current  $I_g(\vec{s}, t) = -\int \vec{J}_g(\vec{s}, t) \cdot \hat{z} d\vec{s}$  is available from the exterior problem and should be accounted for when updating the voltage at the boundary.

### 6.2.3 exterior short circuit problem

The voltage across the aperture along the plate boundary can be treated as an equivalent magnetic current density

$$\vec{M} = \vec{E} \times \hat{n} = -\frac{V(\vec{s}, t)}{d} \hat{s} \quad (6.6)$$

where  $\hat{s}$  denotes the unit vector tangential to the boundary counter-clockwise. In common cases, the separation  $d$  between the two plates is very small and can be neglected. It is a good approximation to model the problem as the excited field by the magnetic current source on a planar ground plane. If the ground plane is large enough to apply image theory, the ground plane can be replaced by doubling the magnetic current, which is illustrated in Fig. 6.3.

To facilitate the derivation, it is easier to employ the time-harmonic analysis. All the variables in the following two sections are expressed in terms of the phasor notation. The scattered magnetic field on the aperture due to the magnetic current can be expressed as [57]

$$\vec{H}^s = \frac{\nabla \nabla \cdot \vec{F} + k^2 \vec{F}}{j\omega\mu} = -\nabla \Psi - j\omega\epsilon \vec{F} \quad (6.7)$$

where the magnetic vector potential

$$\vec{F}(\vec{s}) = \int_{\Gamma} G(|\vec{s} - \vec{s}'|) \vec{M}(\vec{s}') d\vec{s}' \quad (6.8)$$

in which  $G(R) = \frac{e^{-jkR}}{2\pi R}$  is the free space Green's function in the presence of the ground plane,  $k$  is the free space wave number, and  $\Gamma$  denotes the boundary surface.

In (6.7), the magnetic scalar potential  $\Psi$  is introduced as the dual of electric potential. After some algebraic simplification, it can be expressed as

$$\Psi(\vec{s}) = \frac{1}{\mu} \int_{\Gamma} G(|\vec{s} - \vec{s}'|) \rho_m(\vec{s}') d\vec{s}' \quad (6.9)$$

where  $\rho_m$  can be called surface magnetic charge density by duality and is defined by

$$\rho_m(\vec{s}) = -\frac{1}{j\omega} \nabla \cdot \vec{M}(\vec{s}) \quad (6.10)$$

The derivation to (6.9) is possible since  $G$  is a function of  $|\vec{s} - \vec{s}'|$  only and the vector identity

$$\int (\nabla \cdot G) \vec{M} d\vec{s}' = \int (-\nabla' \cdot G) \vec{M} d\vec{s}' = -\int \nabla' \cdot (G \vec{M}) d\vec{s}' + \int G \nabla' \cdot \vec{M} d\vec{s}' \quad (6.11)$$

where  $\nabla'$  means the del operator acting on the primed coordinate  $\vec{s}'$ . It is obvious that the first term in the RHS of (6.11) is zero since either  $\Gamma$  is a close surface or  $\vec{M} = 0$  at the end.

The surface current density across the aperture from the exterior problem will be  $\hat{n} \times \vec{H}^s(\vec{s})$ . Since the total current flows across the aperture should be zero, the integral equation governing the impressed surface current density  $\vec{J}_g(\vec{s})$  in the interior problem and the voltage source  $V(\vec{s})$  in the exterior problem is given by

$$\vec{J}_g(\vec{s}) + \hat{n} \times \vec{H}^s(\vec{s}) = 0 \quad (6.12)$$

Note that  $\vec{H}^s(\vec{s})$  is related to  $V(\vec{s})$  by (6.7), (6.8), (6.9), and (6.10).

## 6.2.4 Moment method solution

Assume that the magnetic currents is expressed as

$$\vec{M}(\vec{s}) = \sum_j V(\vec{s}_j) \vec{B}_j(\vec{s}) \quad (6.13)$$

where  $\vec{B}_j(\vec{s})$  is the roof-top basis on the area of cells  $Ce_{j-\frac{1}{2}}$  and  $Ce_{j+\frac{1}{2}}$  as illustrated in Fig. 6.4. The surface magnetic charge density by (6.10) becomes

$$\rho_m(\vec{s}) = \sum_j \lambda(\vec{s}_{j+\frac{1}{2}}) \Pi_{j+\frac{1}{2}}(\vec{s}) \quad (6.14)$$

Here,  $\Pi_{j+\frac{1}{2}}(\vec{s})$  is a pulse basis, being  $1/(d \cdot |\vec{s}_{j+1} - \vec{s}_j|)$  on the cell  $Ce_{j+\frac{1}{2}}$  and zero elsewhere.  $\lambda(\vec{s})$  denotes the magnetic flux over this cell and is related to the voltage by

$$j\omega\lambda(\vec{s}_{j+\frac{1}{2}}, t) = V_g(\vec{s}_j) - V_g(\vec{s}_{j+1}) \quad (6.15)$$

Choosing the same basis functions (6.13) as the weighting function, the integral equation (6.12) yields to

$$I_g(\vec{s}_i) \cong \int_i \vec{J}_g(\vec{s}) \cdot \hat{n} \times \vec{B}_i(\vec{s}) d\vec{s} = - \int_i \vec{H}^s(\vec{s}) \cdot \vec{B}_i(\vec{s}) d\vec{s} \quad (6.16)$$

The RHS in (6.16) contains the contributions from two terms. For the contribution of magnetic scalar potential, it is not difficult to show that

$$\begin{aligned} - \int_i \vec{B}_i \cdot \nabla \Psi d\vec{s} &= - \int_i \nabla \cdot (\Psi \vec{B}_i) d\vec{s} + \int_i \Psi \nabla \cdot \vec{B}_i d\vec{s} = \int_i \Psi \nabla \cdot \vec{B}_i d\vec{s} \\ &= \frac{1}{\mu} \sum_j \lambda(\vec{s}_{j+\frac{1}{2}}) \left\{ \int_{e_{i-\frac{1}{2}}} \Pi_{i-\frac{1}{2}}(\vec{s}) - \int_{e_{i+\frac{1}{2}}} \Pi_{i+\frac{1}{2}}(\vec{s}) \right\} \int_{e_{j+\frac{1}{2}}} G(|\vec{s} - \vec{s}'|) \Pi_{j+\frac{1}{2}}(\vec{s}') d\vec{s}' d\vec{s} \end{aligned} \quad (6.17)$$

As a result, (6.16) becomes

$$I_g(\vec{s}_i) \cong \sum_j \left( L_{i+\frac{1}{2}, j+\frac{1}{2}}^{-1} - L_{i-\frac{1}{2}, j+\frac{1}{2}}^{-1} \right) \lambda(\vec{s}_{j+\frac{1}{2}}) + j\omega \sum_j C_{i,j} V(\vec{s}_j) \quad (6.18)$$

in which

$$\begin{aligned} L_{i+\frac{1}{2}, j+\frac{1}{2}}^{-1} &\equiv \frac{1}{\mu} \int_{e_{i+\frac{1}{2}}} \int_{e_{j+\frac{1}{2}}} \frac{e^{-jkR}}{2\pi R} \Pi_{i+\frac{1}{2}}(\vec{s}) \Pi_{j+\frac{1}{2}}(\vec{s}') d\vec{s} d\vec{s}'; \\ C_{i,j} &\equiv \varepsilon \int_i \int_j \frac{e^{-jkR}}{2\pi R} \vec{B}_i(\vec{s}) \cdot \vec{B}_j(\vec{s}') d\vec{s} d\vec{s}' \end{aligned} \quad (6.19)$$

### 6.2.5 Time domain integral equation

Physically,  $C_{i,j}$  denotes the capacitive coupling between branch voltages  $V(\vec{s}_j)$  and  $V(\vec{s}_i)$ ,  $C_{i,i}$  is the self-capacitance,  $L_{i+\frac{1}{2}, j+\frac{1}{2}}$  denotes the mutual inductance between cells  $e_{i+\frac{1}{2}}$  and  $e_{j+\frac{1}{2}}$ , and  $L_{i+\frac{1}{2}, i+\frac{1}{2}}$  is the self inductance of the cell  $e_{i+\frac{1}{2}}$ . Due to the phase retardation term  $e^{-jkR} = e^{-j\omega R/c}$ , the effect of  $C_{i,j}$  in the time domain happens at  $\frac{1}{c} R_{i,j} = \frac{1}{c} |\vec{s}_i - \vec{s}_j|$  earlier, and similarly for  $L_{i+\frac{1}{2}, j+\frac{1}{2}}^{-1}$ . Hence from (6.18), the time domain relation between  $I_g(\vec{s}_i, t)$  and  $V(\vec{s}_i, t)$  is given by

$$I_g(\bar{s}_i, t) \cong \sum_j L_{i+\frac{1}{2}, j+\frac{1}{2}}^{-1} \lambda(\bar{s}_{j+\frac{1}{2}}, t - \frac{1}{c} R_{i+\frac{1}{2}, j+\frac{1}{2}}) - \sum_j L_{i-\frac{1}{2}, j+\frac{1}{2}}^{-1} \lambda(\bar{s}_{j+\frac{1}{2}}, t - \frac{1}{c} R_{i-\frac{1}{2}, j+\frac{1}{2}}) + \sum_j C_{i,j} \frac{d}{dt} V(\bar{s}_j, t - \frac{1}{c} R_{i,j}) \quad (6.20)$$

where  $C_{i,j}$  and  $L_{i+\frac{1}{2}, j+\frac{1}{2}}^{-1}$  are the dc-values obtained from (6.19) with  $k=0$ . By

(6.15), the magnetic flux  $\lambda(\bar{s}_{j+\frac{1}{2}}, t)$  satisfies

$$\frac{d}{dt} \lambda(\bar{s}_{j+\frac{1}{2}}, t) = V(\bar{s}_j, t) - V(\bar{s}_{j+1}, t) \quad (6.21)$$

By substituting (6.20) into (6.4), the equivalent circuit for the nodes along the boundary can be obtained and illustrated in Fig. 6.5. The desired updating equation is

$$(\kappa C_{FDTD} + C_{i,i}) \frac{dV(\bar{s}_i, t)}{dt} = I_{FDTD}^{inc} - L_{i+\frac{1}{2}, i+\frac{1}{2}}^{-1} \lambda(\bar{s}_{i+\frac{1}{2}}, t) + L_{i-\frac{1}{2}, i-\frac{1}{2}}^{-1} \lambda(\bar{s}_{i-\frac{1}{2}}, t) + [-I_i^+ + I_i^- - I_i^g] \quad (6.22)$$

where the terms in the bracket consist of the earlier contributions and are given by

$$\begin{aligned} I_i^+ &= \sum_{j \neq i} L_{i+\frac{1}{2}, j+\frac{1}{2}}^{-1} \lambda(\bar{s}_{j+\frac{1}{2}}, t - \frac{1}{c} |\bar{s}_{i+\frac{1}{2}} - \bar{s}_{j+\frac{1}{2}}|) \\ I_i^- &= \sum_{j \neq i} L_{i-\frac{1}{2}, j-\frac{1}{2}}^{-1} \lambda(\bar{s}_{j-\frac{1}{2}}, t - \frac{1}{c} |\bar{s}_{i-\frac{1}{2}} - \bar{s}_{j-\frac{1}{2}}|) \\ I_i^g &= \sum_{j \neq i} C_{i,j} \frac{d}{dt} V(\bar{s}_j, t - \frac{1}{c} |\bar{s}_j - \bar{s}_i|) \end{aligned} \quad (6.23)$$

### 6.2.6 Time marching scheme

The time-marching scheme can be described as follows:

*Step 1)* Start from the voltage  $V^{n-1}(\bar{s}_i)$  the magnetic flux  $\lambda^{n-\frac{1}{2}}(\bar{s}_{i+\frac{1}{2}})$  for all  $i$

and the voltage  $V_{FDTD}^{n-1}$  and current  $I_{FDTD}^{n-\frac{1}{2}}$  in the interior problem. Here, the superscript denotes the time step.

*Step 2)* Update the voltage  $V_{FDTD}^n$  in the interior problem from  $V_{FDTD}^{n-1}$  and

$I_{FDTD}^{n-\frac{1}{2}}$  by employing Ampere's law. Note that the voltage  $V^n(\bar{s}_i)$  along boundary has yet to be determined since the Ampere's law is not applicable there.

*Step 3)* Update the voltage  $V^n(\bar{s}_i)$  by (6.22).

*Step 4)* Update the magnetic flux  $\lambda^{n+\frac{1}{2}}(\bar{s}_{i+\frac{1}{2}})$  from  $\lambda^{n-\frac{1}{2}}(\bar{s}_{i+\frac{1}{2}})$  and  $V^n(\bar{s}_i)$  by

$$(6.21).$$

*Step 5)* Update currents  $I_{FDTD}^{n+\frac{1}{2}}$  from  $V_{FDTD}^n$ , and current  $I_{FDTD}^{n-\frac{1}{2}}$  by employing Faraday's law.

It is worthy mentioning that *steps 2)* and *5)* in the updating equations for voltage and current inside the FDTD unit cell are exactly the same as those in the conventional 2D-FDTD.

### 6.3 Numerical Examples

A patch antenna with infinite ground plane is used to test the present methodology. As shown in Fig. 6.6, the size of patch is 1.8cm×2.4cm, with the dielectric constant  $\epsilon_r = 2.33$ , and substrate thickness  $d = 1\text{mm}$ . In numerical simulation, the grid size of FDTD is  $\Delta = 0.5\text{mm}$ . The total simulation region is divided into  $36 \times 48$  cells along  $x$  and  $y$  directions, respectively. The signal voltage source is a Gaussian pulse generator

$$V_s(t) = \exp\left[-\left(\frac{t-t_0}{\sigma}\right)^2\right] \quad (6.24)$$

in series with an internal resistance of 50 ohm and is incident at  $\bar{r}_0 = (4\text{mm}, 12\text{mm})$ . The parameters of Gaussian pulse are  $\Delta t = 1\text{ps}$ ,  $t_0 = 50\Delta t$ ,  $\sigma = 10\Delta t$ .

From the simulated waveform at  $\bar{r}_0$ , the input impedance to the patch structure  $Z_i(\omega)$  is calculated by

$$Z_0(\omega, z) = \frac{F[V(\bar{r}_0, t)]}{F[I(\bar{r}_0, t)]}. \quad (6.25)$$

Hence,  $S_{11}$  can be calculated by

$$S_{11}(\omega) = \frac{Z_i(\omega) - 50}{Z_i(\omega) + 50}. \quad (6.26)$$

Figure 6.7 compares the results simulated by the present method and IE3D. The first null occurs at 5.3 GHz for the present method and 5.22 GHz for IE3D. It is found that the results by both methods are in good agreement. However, the null frequency of the present method is slightly higher than that predicted by IE3D, since the present method assumes that the magnetic current along the open boundary radiates in free space. The real relative permittivity  $\epsilon_r$  should be higher than one due to the presence of substrate.

## 6.4 Experimental Validation

A four-layer PCB of two isolation power islands is fabricated to investigate the coupled noise between islands. As shown in Fig. 6.8, the two power islands are of size  $2.5\text{cm} \times 3\text{cm}$  and separated by 1mm, while the substrate is of thickness  $d=1.2\text{mm}$ , and dielectric constant  $\epsilon_r = 4.2$ . The whole structure is symmetric.

In the experiment, a ramped step pulse of about 100ps rise time is used as the excitation on port 1. The TDR and TDT signals at ports 1 and 2, respectively, are measured by Tektronix 11801C. Since there are no vias nor transmission lines between these two power islands, the measured signal at port 2, if any, could be contributed to the coupling of the open boundary.

In numerical simulation, the measured input waveform is used as the excitation signal. The total simulation region is divided into  $61 \times 25$  cells with grid size  $\Delta = 1\text{mm}$  along  $x$  and  $y$  directions, respectively. Noting that the power plane for this structure is embedded into the dielectric, the relative permittivity for the exterior problem is chosen as  $\epsilon_r = 4.2$ . A better value should be somewhat lower than 4.2, since the material is not distributed in the whole space. The simulation is performed to 8000 time steps with  $\Delta t = 1\text{ps}$  to get a frequency resolution of 0.125GHz.

Figures 6.9(a) and (b) show the results at TDR and TDT ports, respectively. These curves denote the results obtained by simulation with radiation and PMC boundary, and experiment. They exhibit different RC time constants at the TDR port. The value is close to 1162ps for the case of PMC boundary. This can be justified since the capacitance is calculated to be  $C = \epsilon \frac{A}{d} \approx 23.24\text{pF}$  by parallel-plate formula, and the resistance  $R=50\text{ohm}$ . The RC time constant will be larger in the present method, since the fringing effect enlarges the effective area of patch. It is noted from the figure that the RC time constant of experiment is even longer, which might be contributed to some additional loss of measurement system and PCB conductor and dielectric.

At the TDT port, the conventional method, which assumes PMC boundary fails to predict any coupled noise. In the present case that the step voltage of the signal is 0.25 volts, the coupling noise level at port 2 is measured to be 4mV as opposed to 5.3mV by the present simulation method. In other words, the generated coupled noise between isolation islands for the present case may achieve about 2% of the input level. The over-estimation in the simulation result can be contributed to the negligence of the loss by the substrate, conductor, and radiation.

Figure 6.10 shows the power spectrum density of the TDT signal obtained by the measurement and the present method. Also shown for comparison are the results by



frequency domain full wave solver IE3D, for which the power spectrum density is calculated by the multiplication of  $S_{21}$  and power spectrum density of input waveform. Both the present simulation and IE3D are executed on the same computer with CPU of Pentium III 1GHz. The present method needs 450 seconds to calculate the response. Based on the same gridding and the same frequency resolution, IE3D needs 33062 seconds to complete the simulation, almost 74 times longer. In addition, it can be seen from the figure that the results predicted by IE3D deviate from the measured data much more significantly than those by the present simulation method.

There are some peaks to signify the various resonance modes in Fig. 6.10. Since the position of excitation is located at the symmetric line of the short edge, the first two peaks correspond to  $TM_{10}$  and  $TM_{20}$  modes and should occur at 2.375GHz and 4.714GHz, respectively. The agreement between measurement and simulation demonstrates the accuracy of the present method. The frequency of the peak coupling noise is a little bit lower than the measurement, which may be partly contributed to using  $\varepsilon_r = 4.2$  for the exterior problem.

## 6.5 Summary

A new methodology is presented to simulate the signal integrity issues between isolation islands due to radiation coupling from the power plane boundary. The methodology can be cast into two-dimensional FDTD to analyze the radiation problems of PCB. Favorable agreement between numerical and experimental results has demonstrated the accuracy of this method. Although the coupled noise caused by radiation is less than 2%, the effects may severely deteriorate the signal integrity of other islands at some resonant frequencies.

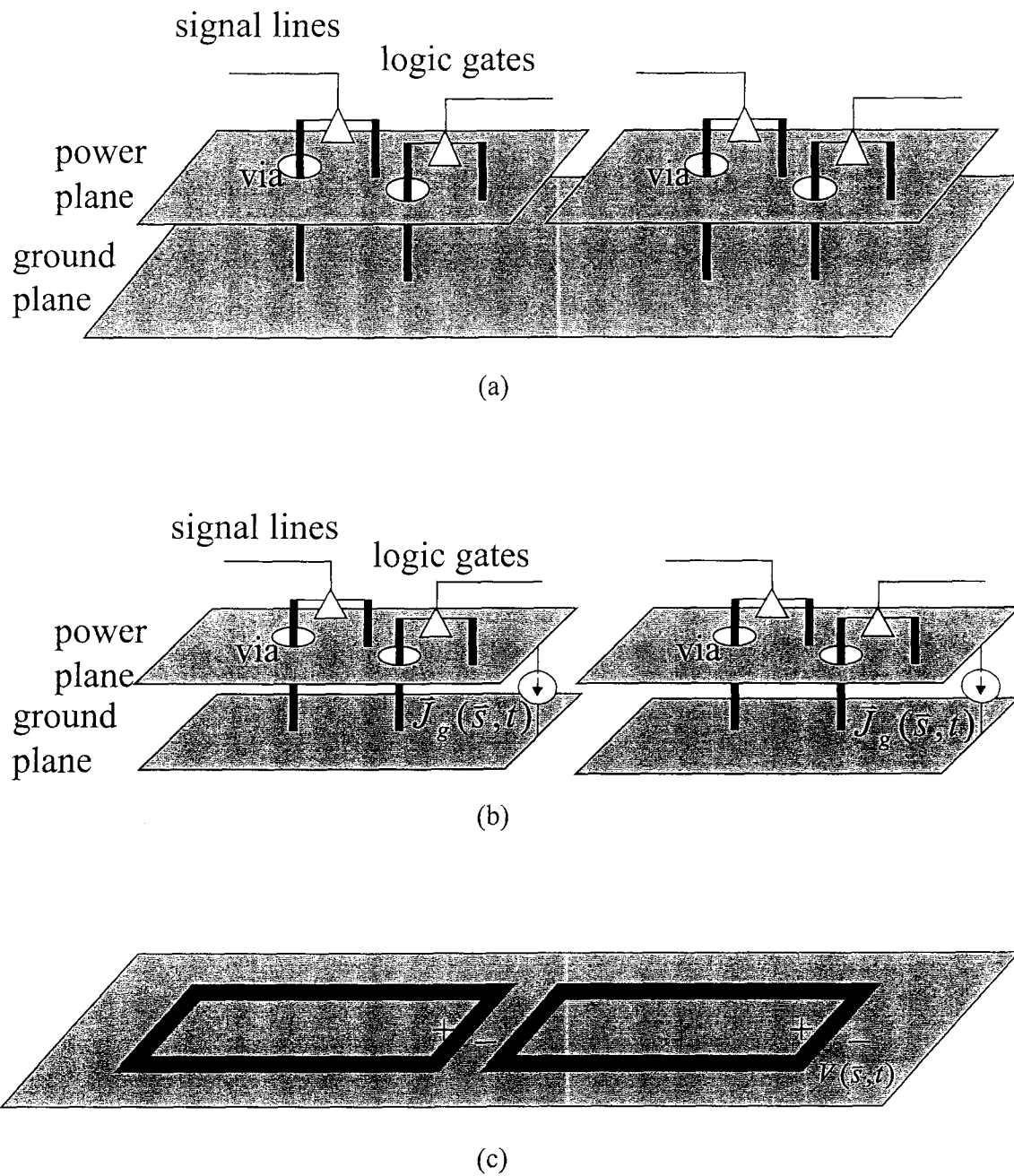


Fig. 6.1 A typical PCB structures with separated power islands. (a) Original problem, (b) interior open-circuit problem, and (c) exterior-short circuit problem.

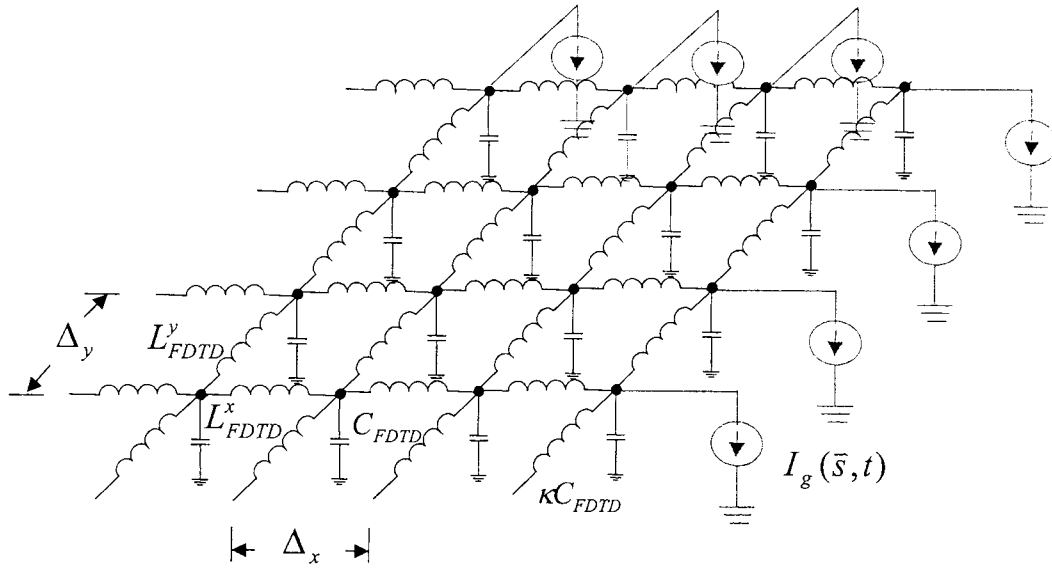


Fig. 6.2 Equivalent LC network for interior problem.

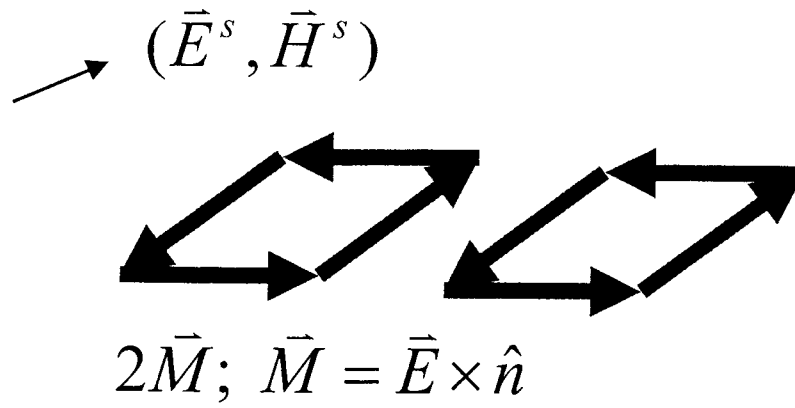
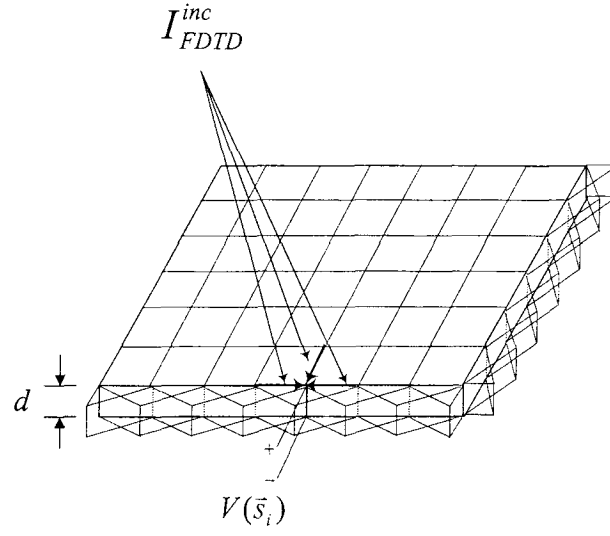
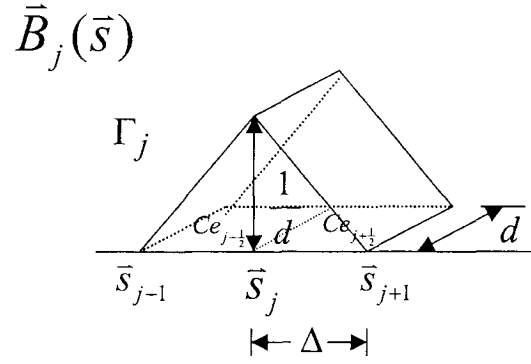


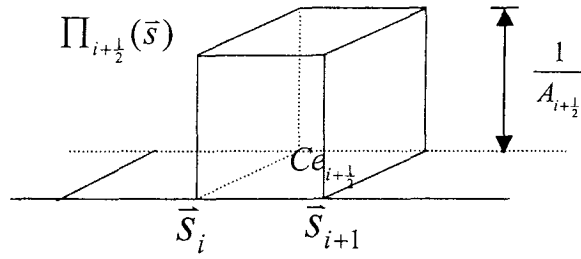
Fig. 6.3 Equivalent magnetic current source and resultant electromagnetic field for exterior problem.



(a)



(b)



(c)

Fig. 6.4 (a) Grid meshing for the structure and node voltage  $V(\bar{s}_j)$ , (b) roof-top basis for magnetic current, and (c) pulse basis for magnetic flux across the aperture.

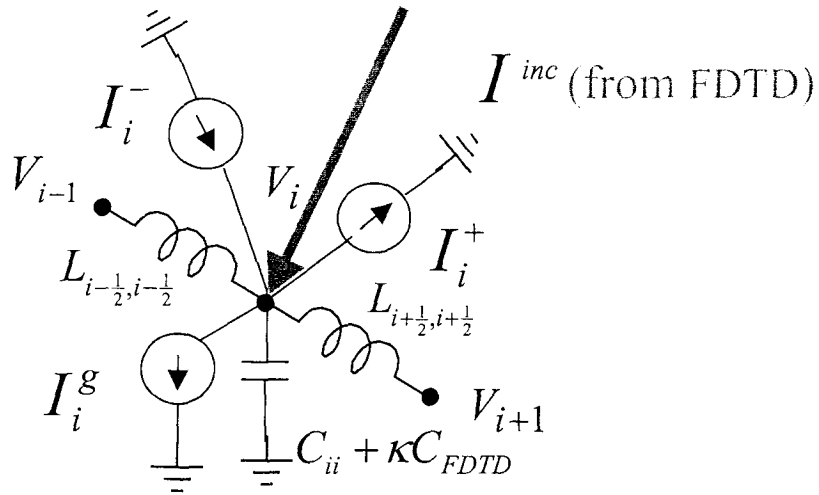


Fig. 6.5 Equivalent circuit for updating the node voltage at boundary.

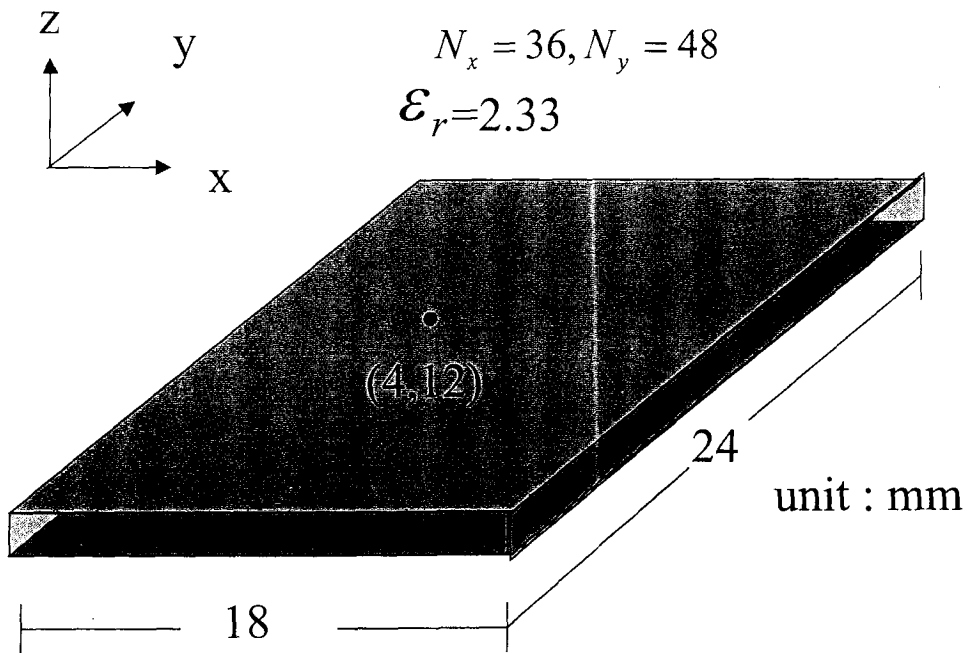


Fig. 6.6 A patch antenna of infinite ground plane used for simulation.

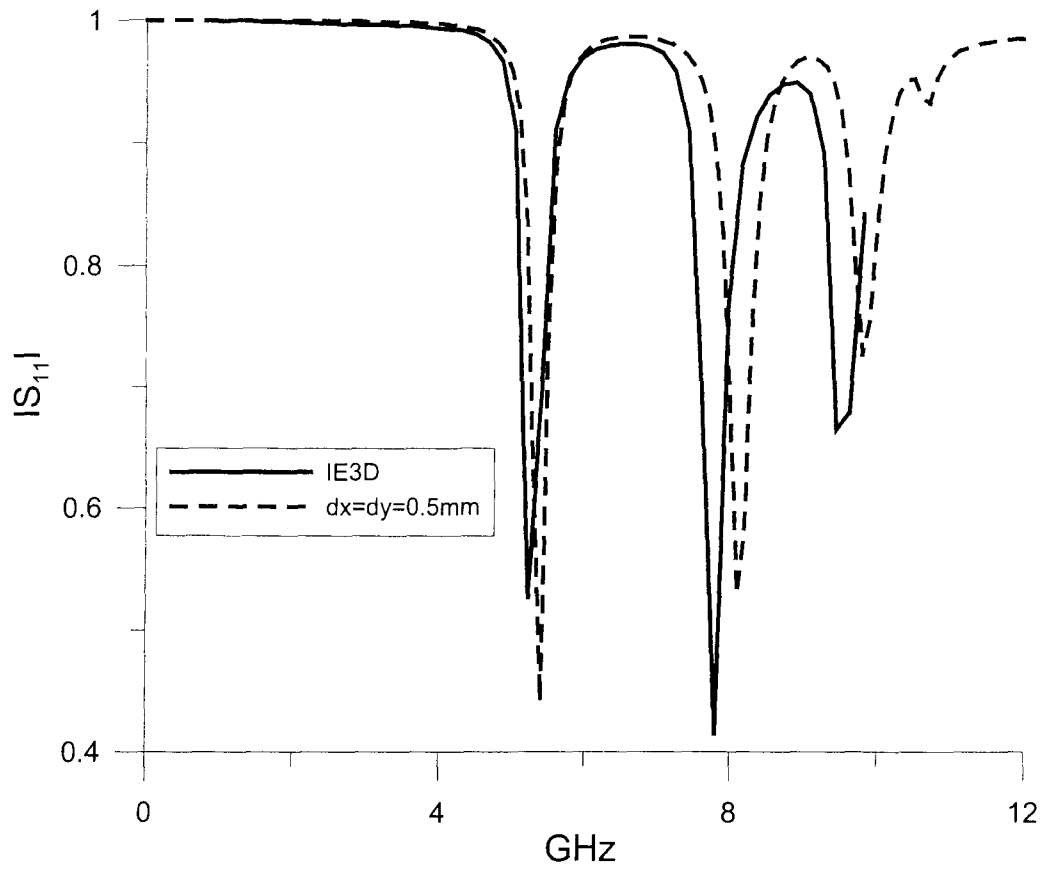
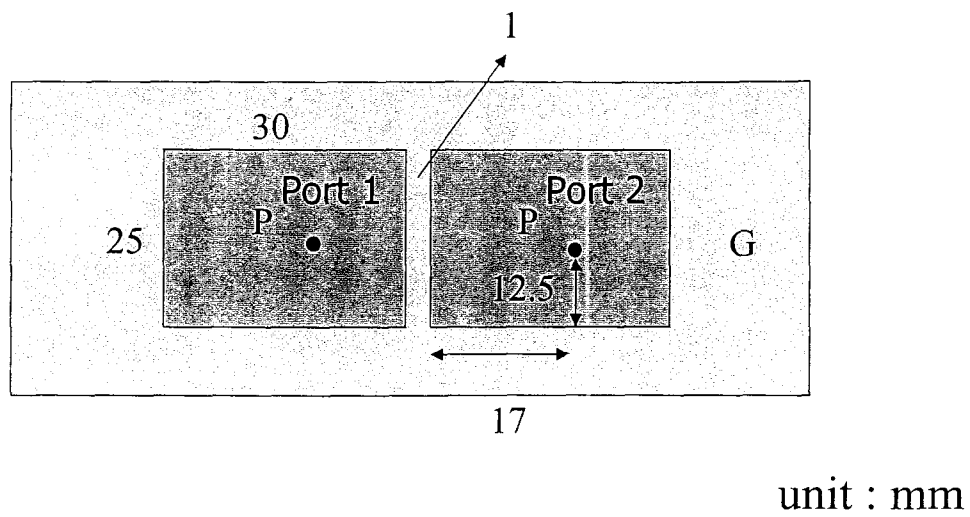
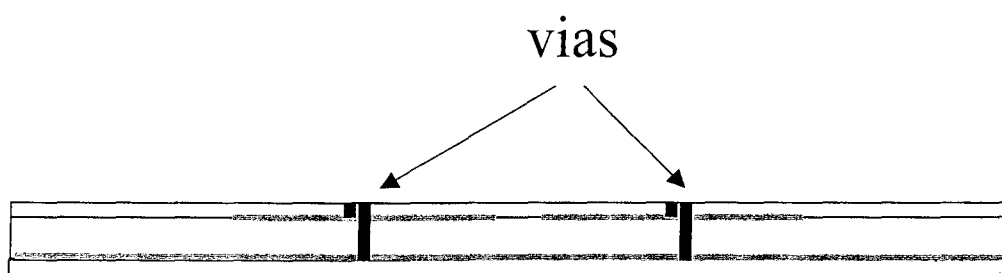


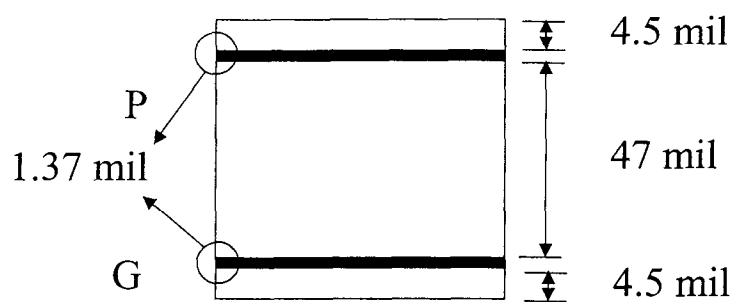
Fig. 6.7 simulated results for  $S_{11}$  by the present method and a frequency domain full wave solver IE3D.



(a)



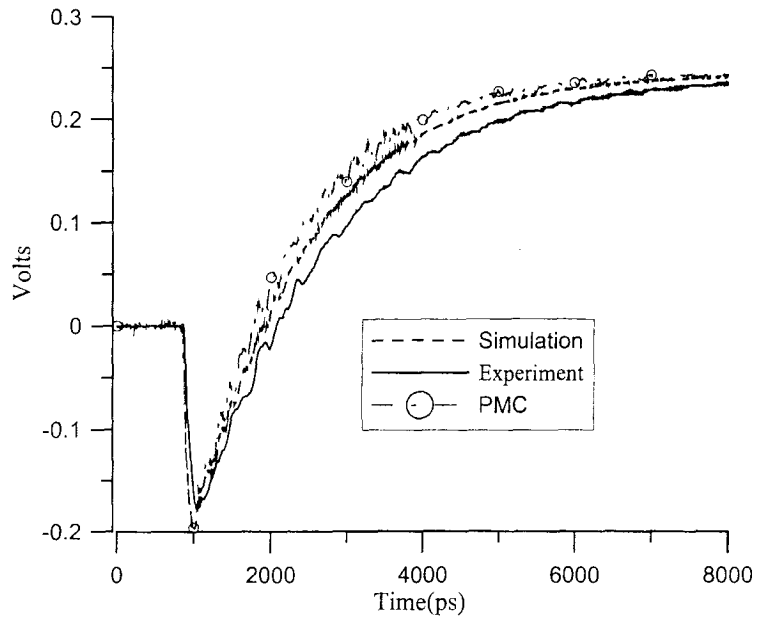
(b)



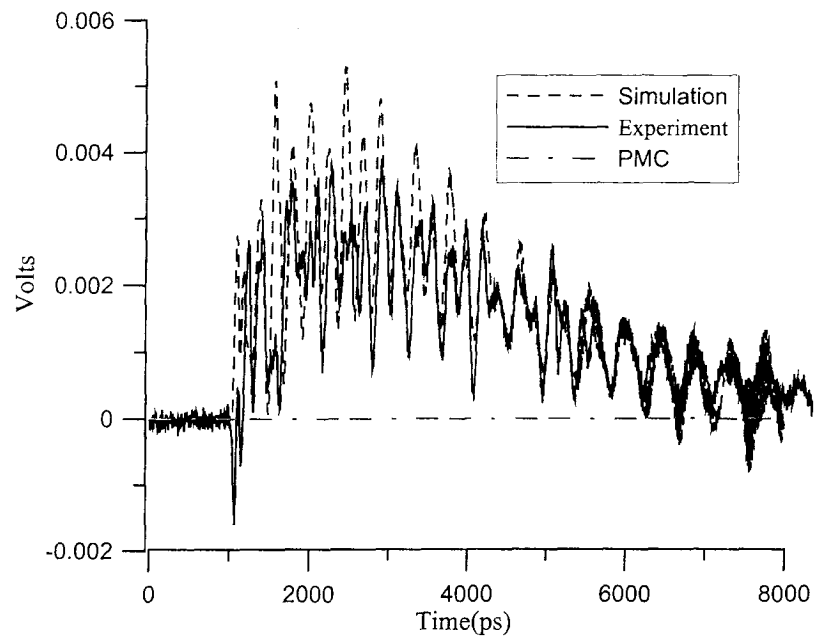
(c)

Fig. 6.8 A test PCB of isolation power plane used for experiment and simulation. (a)

Top view, (b) side view, and (c) thickness of the substrate and metal plane.



(a)



(b)

Fig. 6.9 Measured and simulated waveforms of (a) TDR signal at port 1 and (b) TDT signal at port 2.



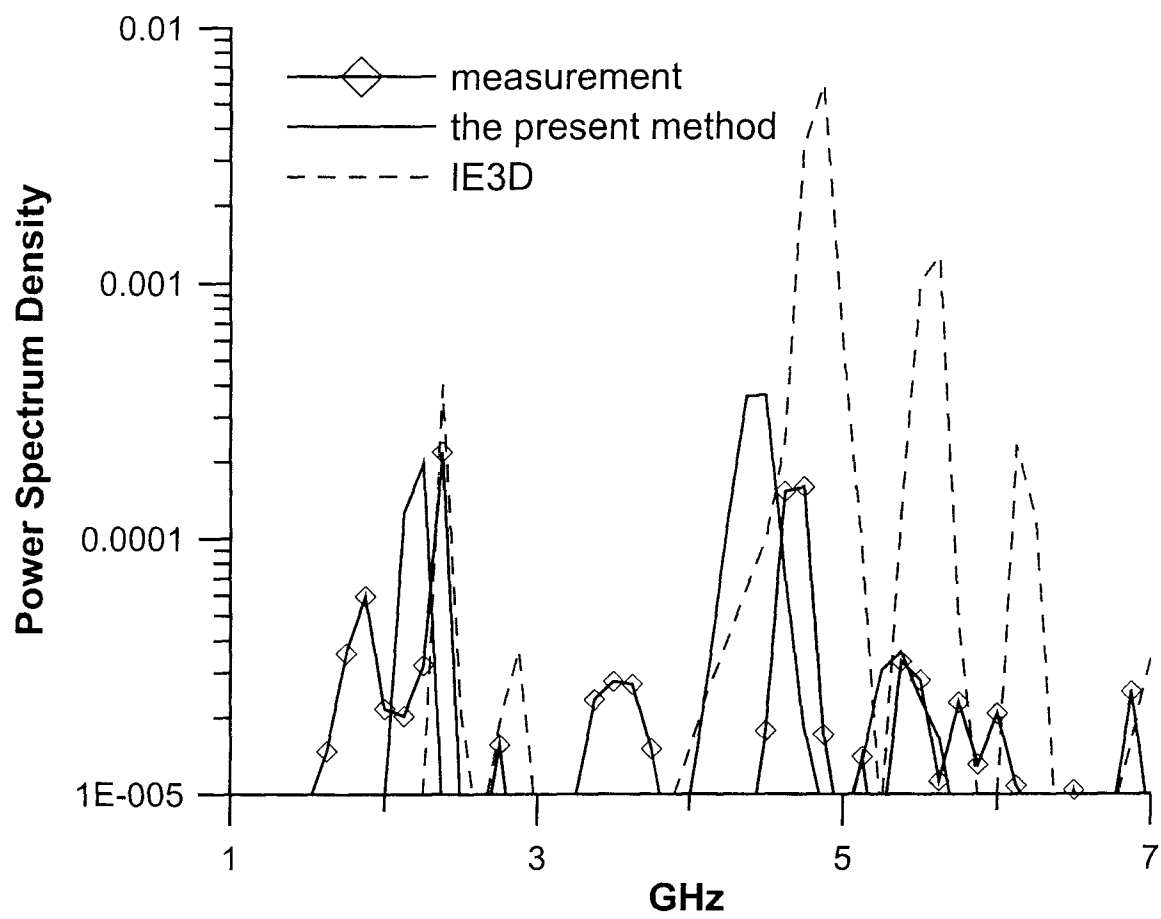


Fig. 6.10 Power spectrum density of TDT signal. Comparisons among measurement, the present method, and IE3D.

## Chapter 7

### Visualization for Simulation Results

#### 7.1 Introduction

Visualization systems provide a good interface between computers and users. Visualization of numerical results, such as the mesh grid in FE/FDTD method (pre-processing) and the field distribution in printed circuits (post-processing), can not only help the programmers in debugging during the development of the program, but also help the users have a physical insight of electromagnetic phenomenon. Many physical parameters are invisible and hard to measure, e.g. electric currents and fields. However, they can be numerically computed and present with visualization tools. More understanding on physical mechanism will thus be obtained.

One salient feature of FDTD method is the capability of simulating the field distribution as a function of time. Therefore it is one of the most popular schemes incorporated with the graphic interface to display the behavior of electromagnetic wave. Two kinds of visualization systems will be described in this chapter. One is the employment of the web-based visualization system, and the other is to present the simulation results by commercial software.

#### 7.2 Web-Based Visualization System

Web-based visualization tool has been widely applied for various areas of science since the popularization of networks. The solver is put on the remote high-performance computer, and the calculated data is then visualized on the client via web-based communication tools. Although popular in science, only few visualization tools for electromagnetic simulation are developed.

A web-based visualization tool has been recently developed by National Center for High-Performance Computing (NCHC). It can be incorporated with the extended FDTD method to aid the visualization. This tool contains three parts: Visualization Client (client), Server, and Computation Solver (solver) as displayed in Fig. 7.1 [58]. A researcher may use the Java coded Problem-Solving Environment (PSE) to interact with the system from the client. The Server forwards data and communicates between the client and the solver. The communication between the client and the server is

established via Socket(TCP/IP, standing for Transmission Control Protocol/Internet Protocol), while the communication between the server and the solver is achieved by Parallel Virtual Machine (PVM). In running time, the solver sends simulation results to the server then the server forwards it back to the client for the visualization to the corresponding results. Once the web-based visualization system is set up, the researcher only need to create the EM solver and input file to fit their needs.

To demonstrate the performance of the present visualization system, the extended FDTD method is applied to simulate the electromagnetic scattering of two-dimensional circular dielectric object for TM case. A circular cylinder of dielectric constant  $\epsilon_r = 4$  and radius of  $10\Delta$  is normally illuminated by a Gaussian pulse of three-sigma pulse width  $20\Delta$  along +X direction. The visualization region is displayed in Fig. 7.2. The solver code is properly inserted with some PVM codes and executed on the sp2 in NCHC. The server is also located in NCHC which transfers the data from the sp2 to the local client for visualization. The client is the notebook with Pentium 233.

Fig. 7.3 to Fig. 7.9 show the  $E_z$  field surface plot and the  $H$  field vector plot for the region as shown in Fig. 7.2 at some specified time steps. Fig. 7.3 shows the peak of the Gaussian pulse is approaching the boundary of the circular cylinder on point A at time step 100. The plane wave is slightly deformed along the boundary of the circular cylinder. Fig. 7.4 shows the peak of the Gaussian pulse hit the other boundary of the circular cylinder on point D at time step 160. The shape of the pulse is strongly deformed and confined inside the circular cylinder. Fig. 7.5 shows the pulse interacts with the boundary with opposite phase on point D at time step 200. Fig. 7.6 shows the pulse is separated into two small pulses and reflected back to the point B and point C along the boundary of the circular cylinder at time step 240. Fig. 7.7 shows these two small pulses collide on the boundary of the circular cylinder on the point A at time step 280. Fig. 7.8 and Fig. 7.9 show the pulse reflected back to point D via point B and point C with the same route at time step 320 and 360, respectively. For successive process, the behavior of the pulse inside the circular cylinder repeats in the same way as aforementioned process from Fig. 7.5 to Fig. 7.9, meanwhile the peak of the pulse gradually decay as marching. It is observed that the pulse takes about 160 times steps to complete one round trip which may be treated as the period of the pulse inside the circular cylinder. From the computer animation, we may also realize how the amplitude and the phase change. Here, the numerical results have been successfully visualized by incorporated with the technique of the distributed computing.

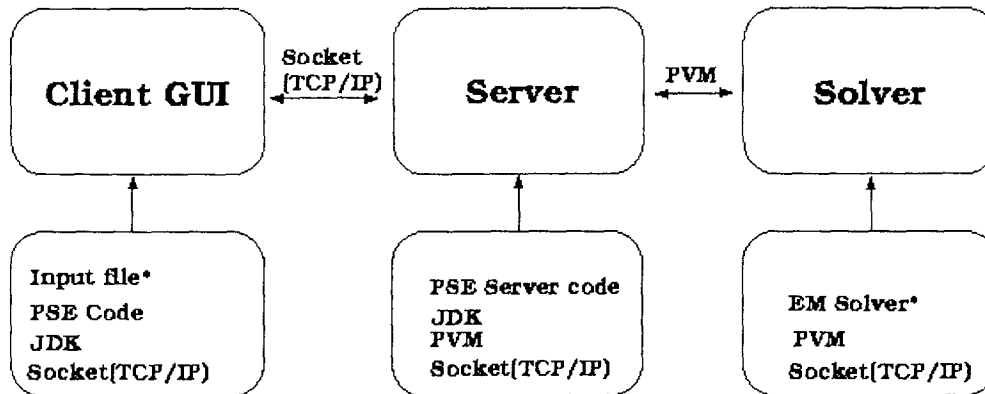
### 7.3 Visualization with Commercial Software

A simple way for visualization of numerical results by the commercial software, MATFOR (AnCAD, Inc), is described in this session. MATFOR is a numerical and visualization library based on FORTRAN 90/95 [59]. With a few additional instruction lines, a FORTRAN program can be corporate with MATFOR for animation.

The case for isolation islands that is described in the previous chapter is used as an example for animation. Fig. 7.10 is the structure of the isolation islands, and Fig. 7.11 to Fig. 7.16 show surface plot and contour plot of  $E_z$  field between planes. In the beginning, a Gaussian pulse is excited underneath one of the island, and then coupled to the other. From the animation, it is obvious that the coupling is through the two nearest edges between the two islands.

### 7.4 Summary

Two kinds of visualization system are introduced. One is web-based and the other is with commercial software. With the help of the fields visualization, the researchers can have deep understanding about the physical mechanism of the electromagnetic phenomena.



- **Client GUI :**  
 Input file : set parameters for visualization which is edited by user.  
  
 PSE code : a Java code, to start the program and visualize the data transferred from Solver.
- **Server :**  
 PSE Server code : a Java code, to establish the communication between Java and PVM.
- **Solver :**  
 EM Solver : the electromagnetic simulator, say FDTD, FEM, which should be properly inserted with some PVM codes to send the data required by the Input file.

Fig. 7.1 The web-based visualization system.

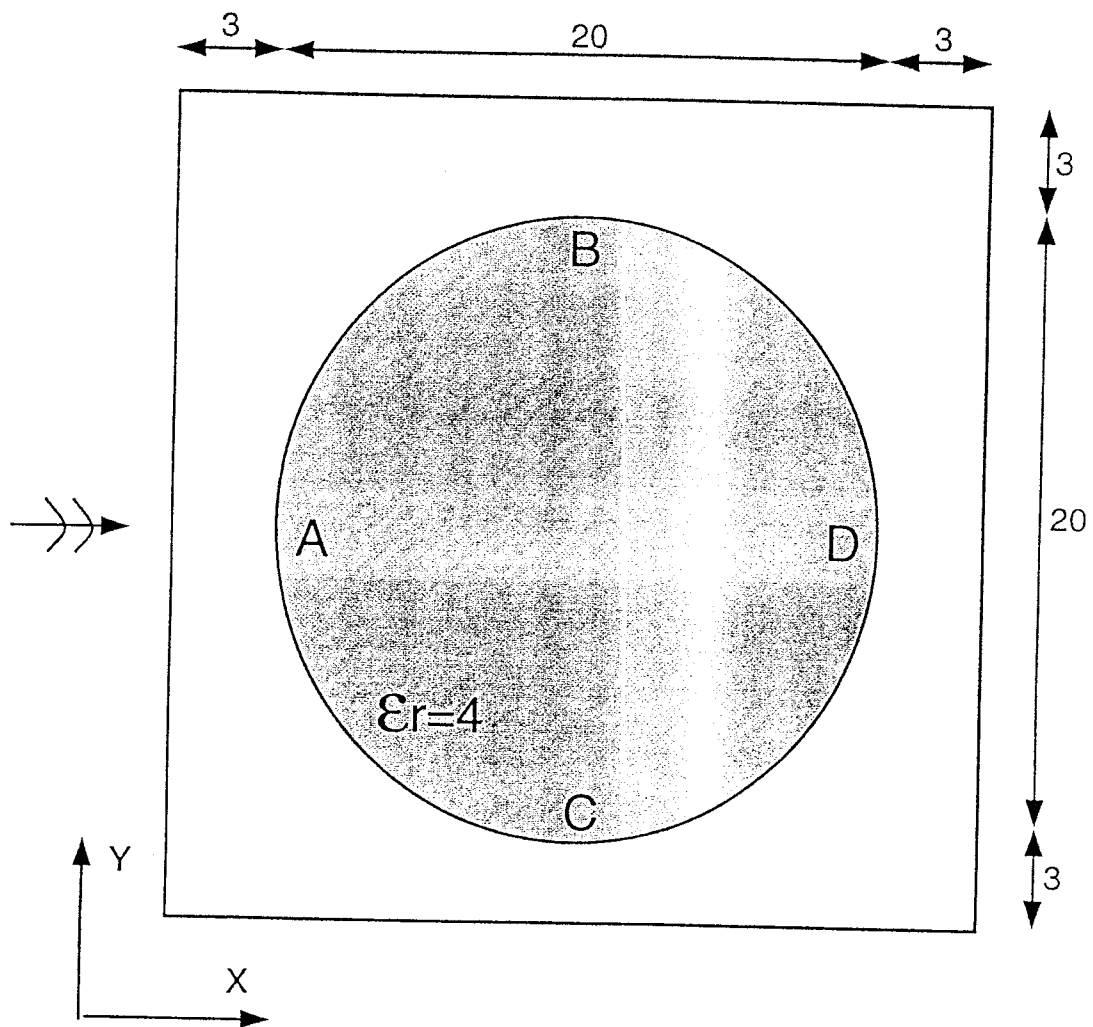
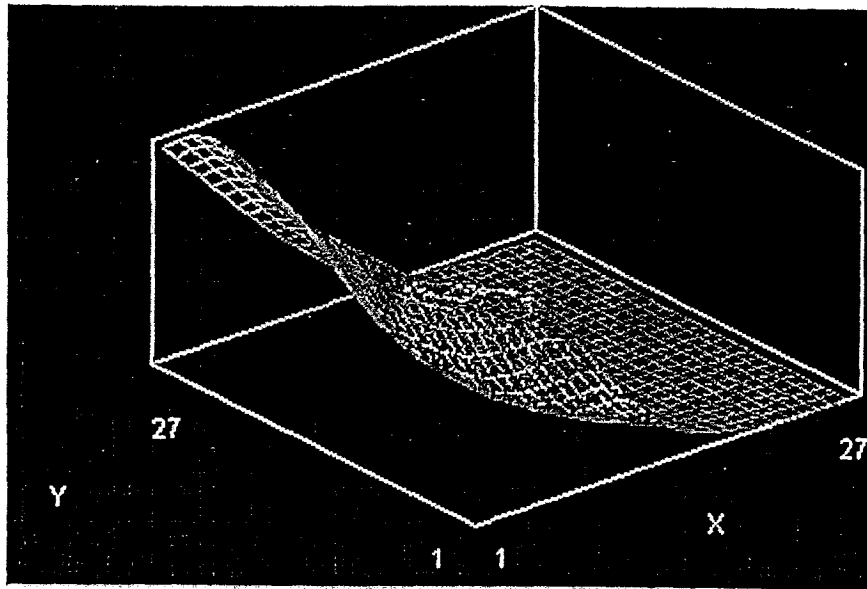
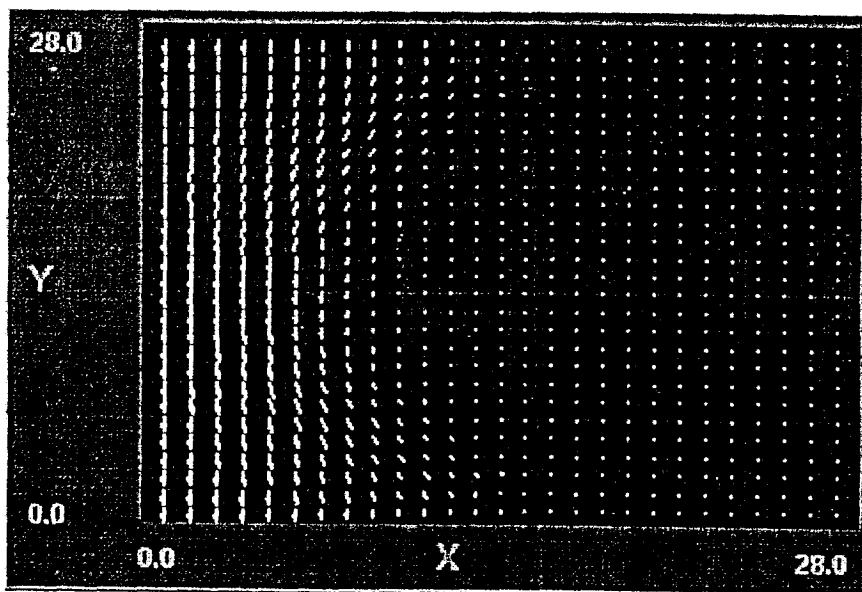


Fig. 7.2 The visualization region for dielectric circular cylinder.

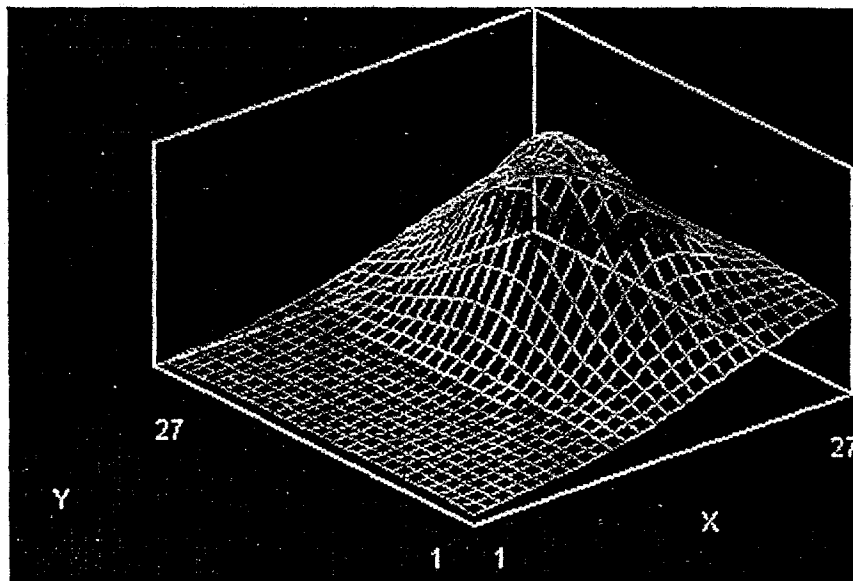


(a)

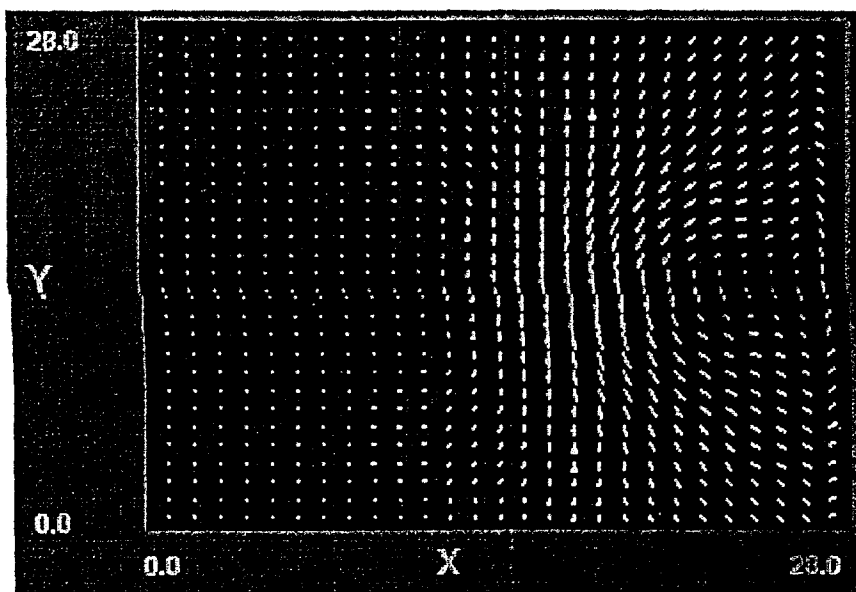


(b)

Fig. 7.3 (a) The  $E_z$  field surface plot and (b) the  $H$  field vector plot at time step 100.



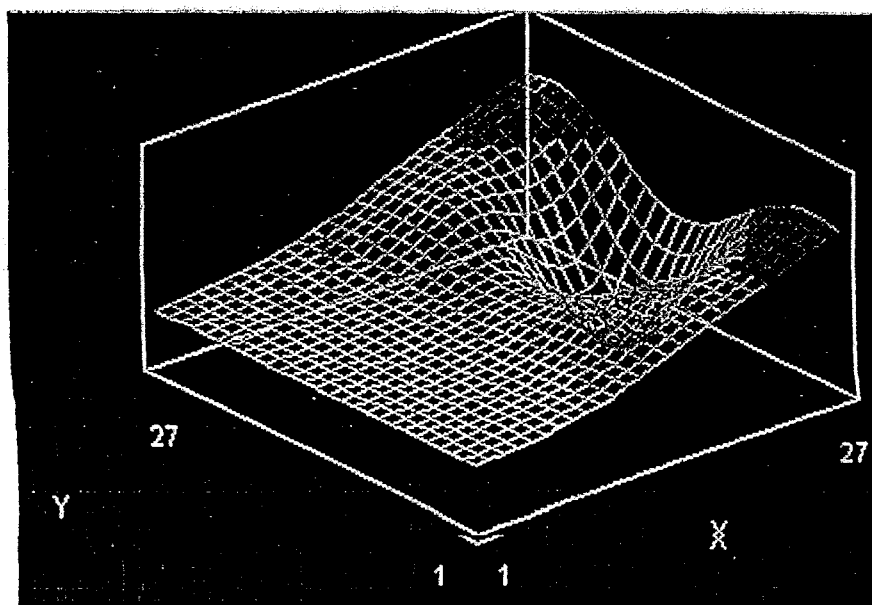
(a)



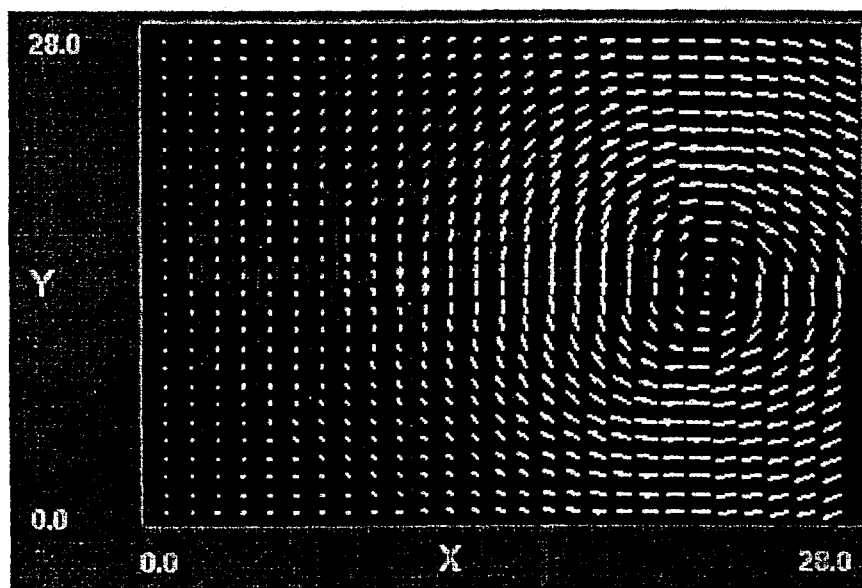
(b)

Fig. 7.4 (a) The  $E_z$  field surface plot and (b) the  $H$  field vector plot at time step 160.



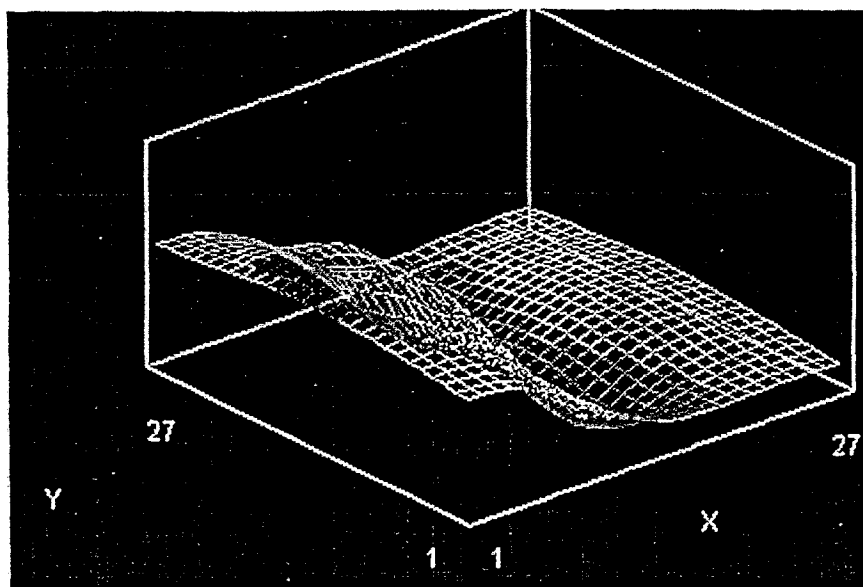


(a)

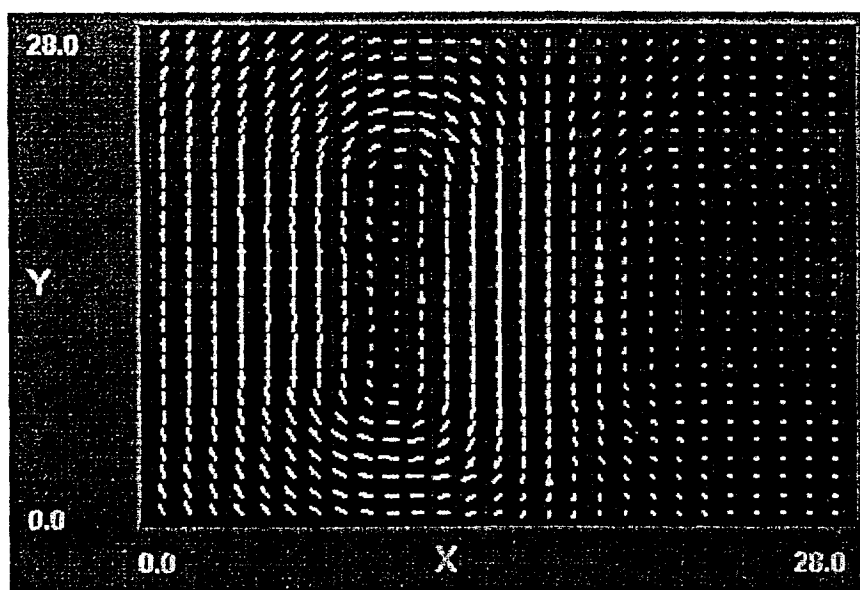


(b)

Fig. 7.5 (a) The  $E_z$  field surface plot and (b) the  $H$  field vector plot at time step 200.

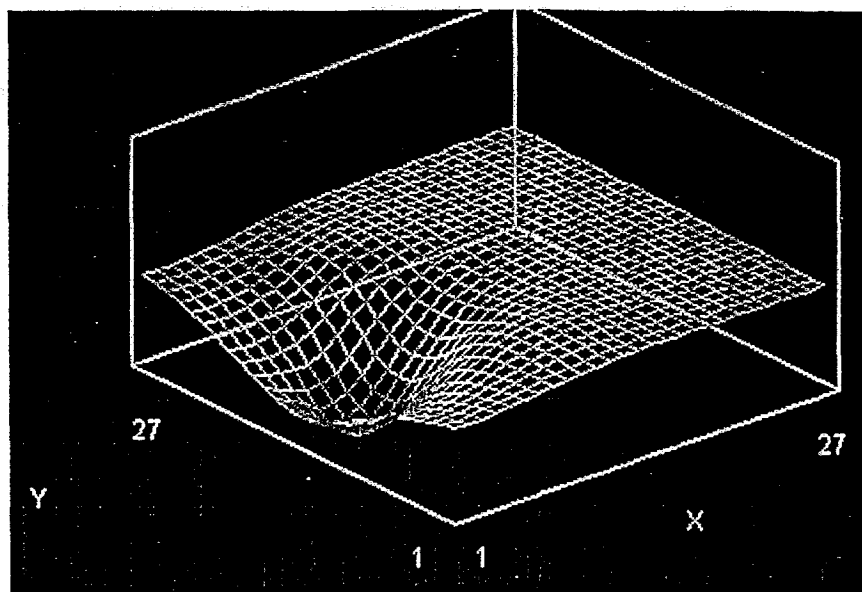


(a)

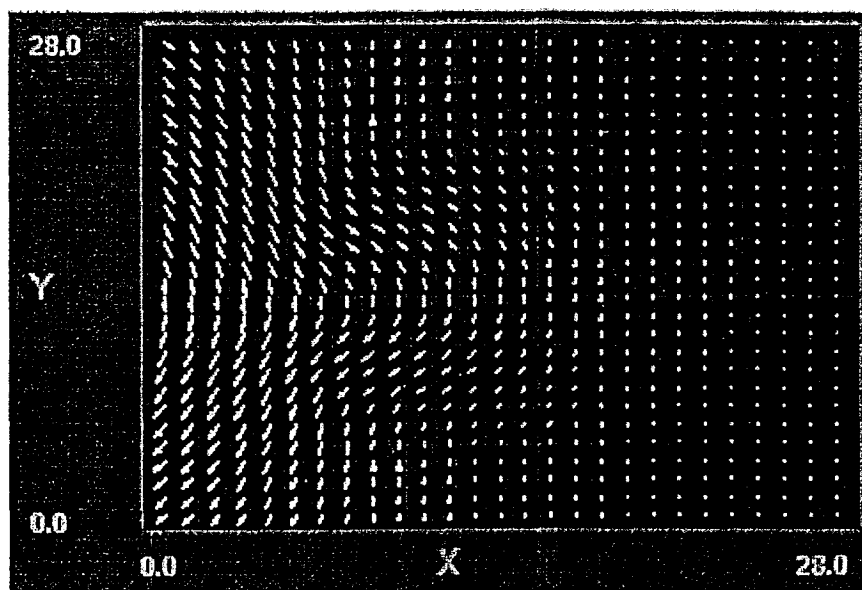


(b)

Fig. 7.6 (a) The  $E_z$  field surface plot and (b) the  $H$  field vector plot at time step 240.

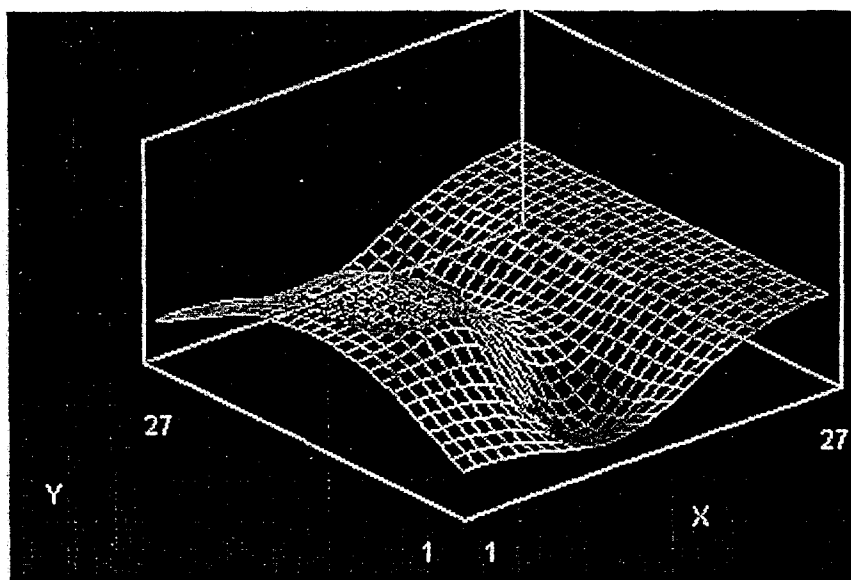


(a)

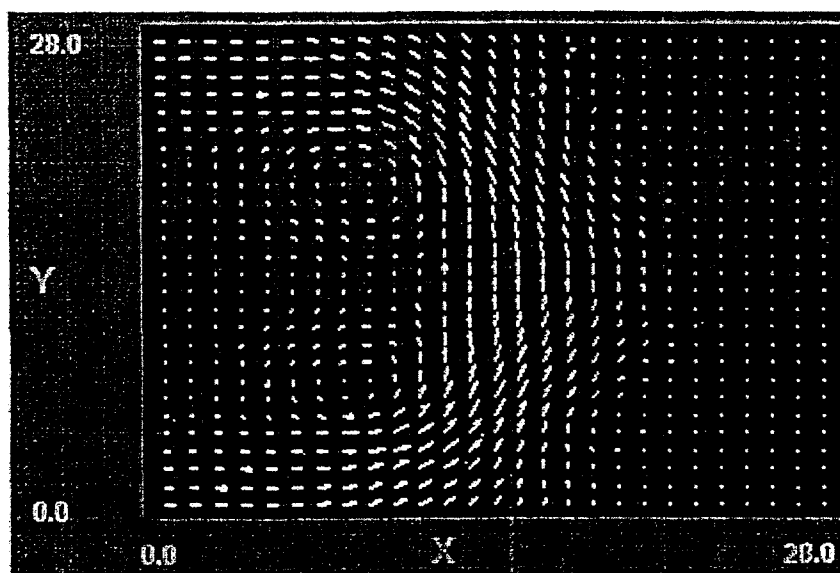


(b)

Fig. 7.7 (a) The  $E_z$  field surface plot and (b) the  $H$  field vector plot at time step 280.

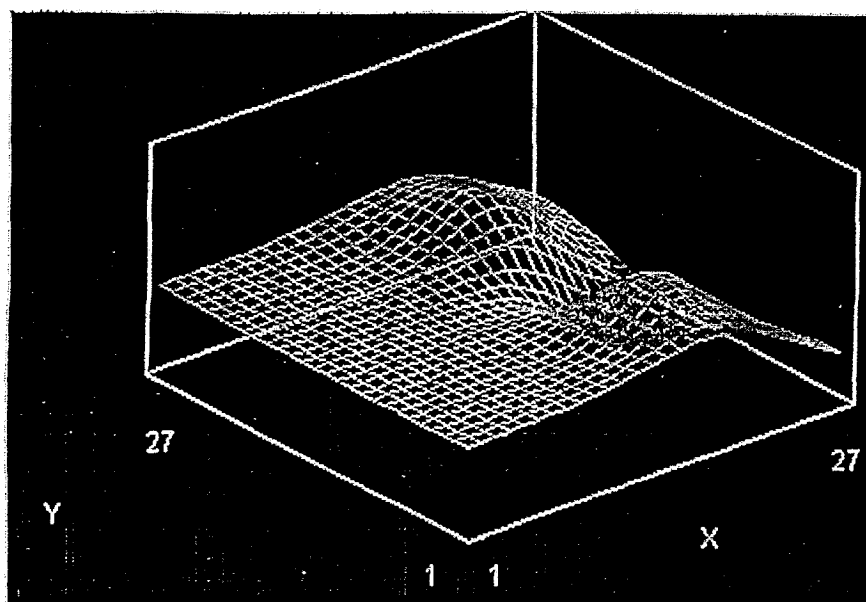


(a)

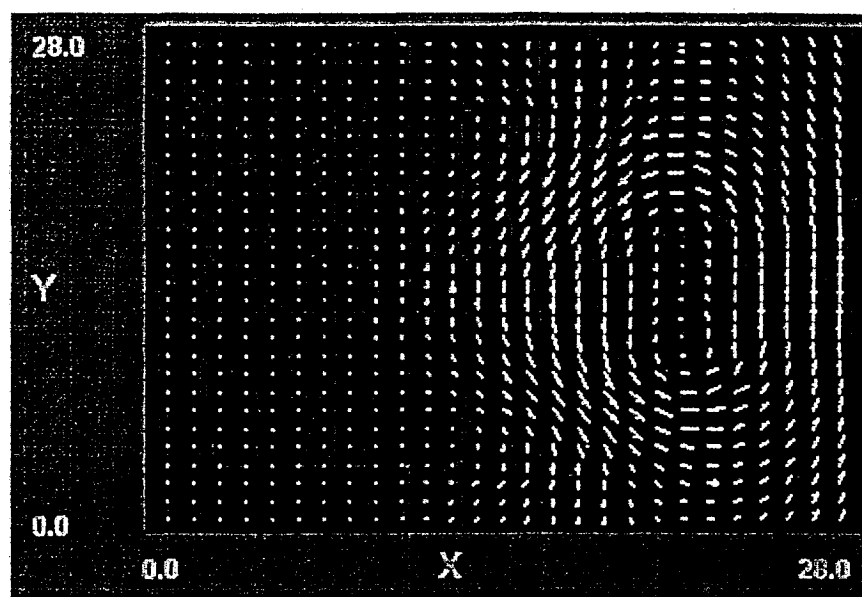


(b)

Fig. 7.8 (a) The  $E_z$  field surface plot and (b) the  $H$  field vector plot at time step 320.



(a)



(b)

Fig. 7.9 (a) The  $E_z$  field surface plot and (b) the  $H$  field vector plot at time step 360.

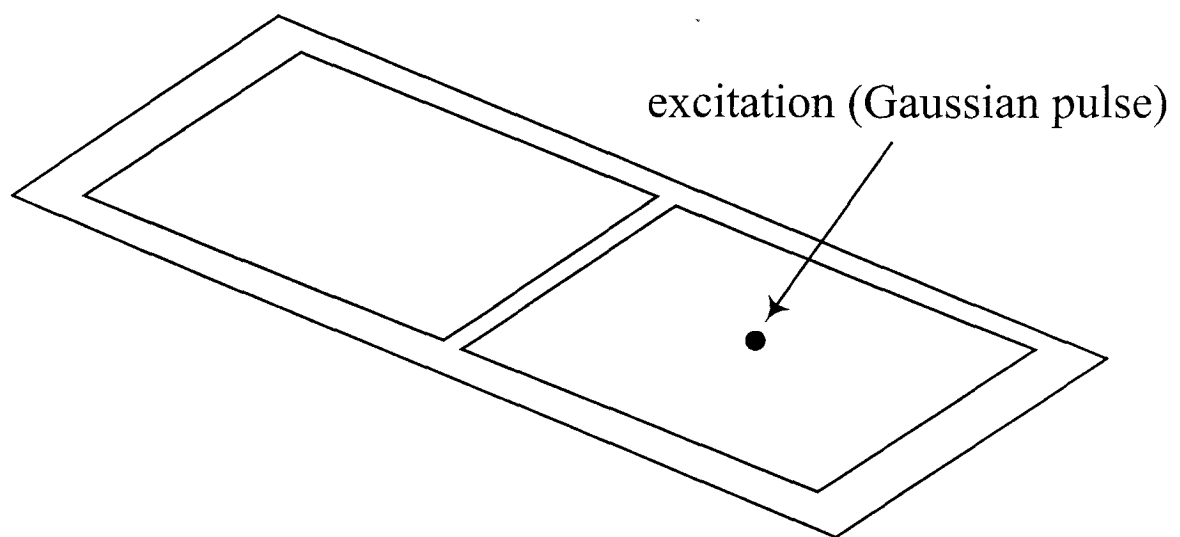
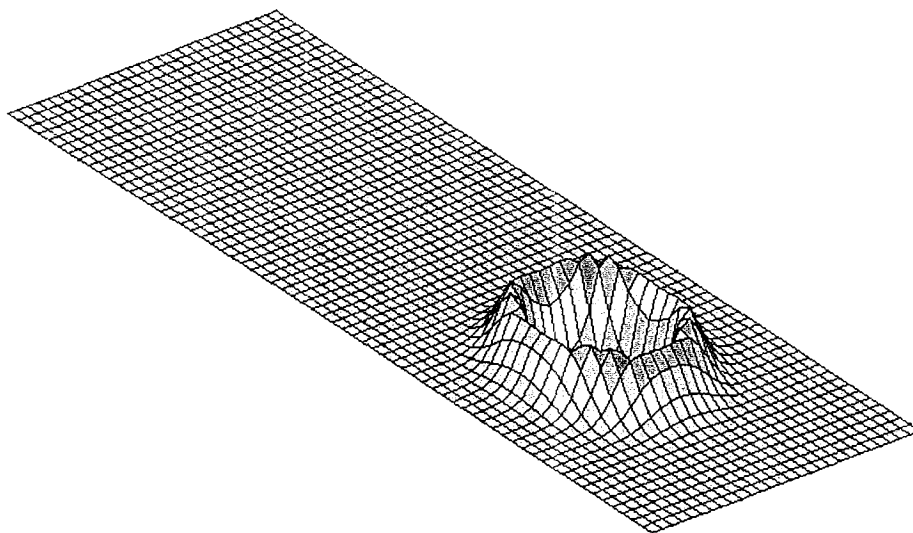
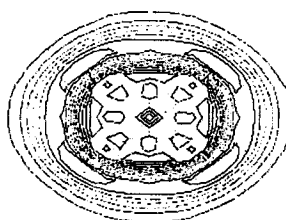


Fig. 7.10 Isolation islands used for visualization.

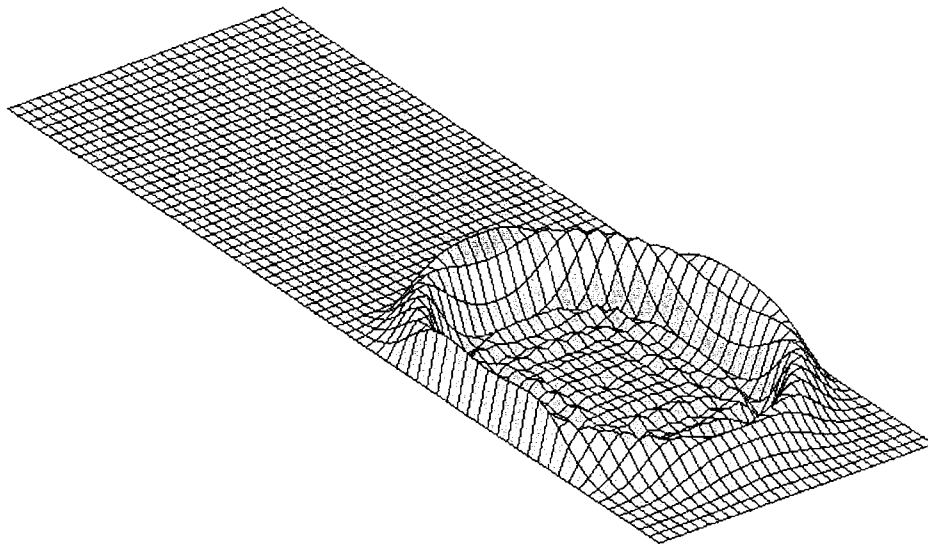


(a)

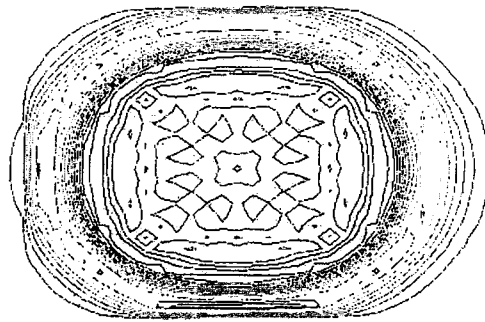


(b)

Fig. 7.11 (a) The  $E_z$  field surface plot and (b) contour plot at time step 100.



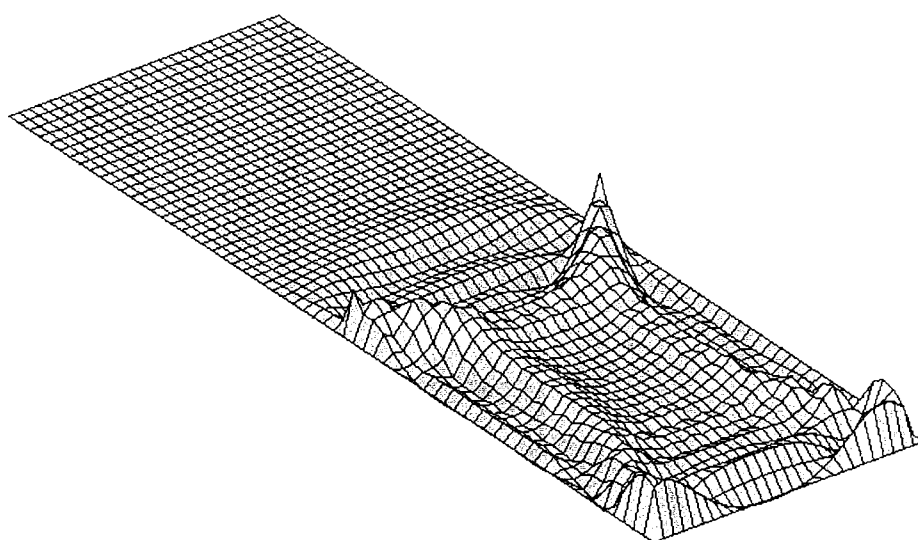
(a)



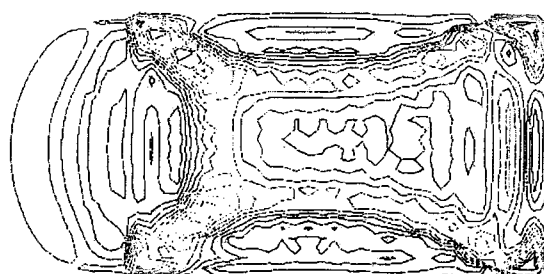
(b)

Fig. 7.12 (a) The  $E_z$  field surface plot and (b) contour plot at time step 150.



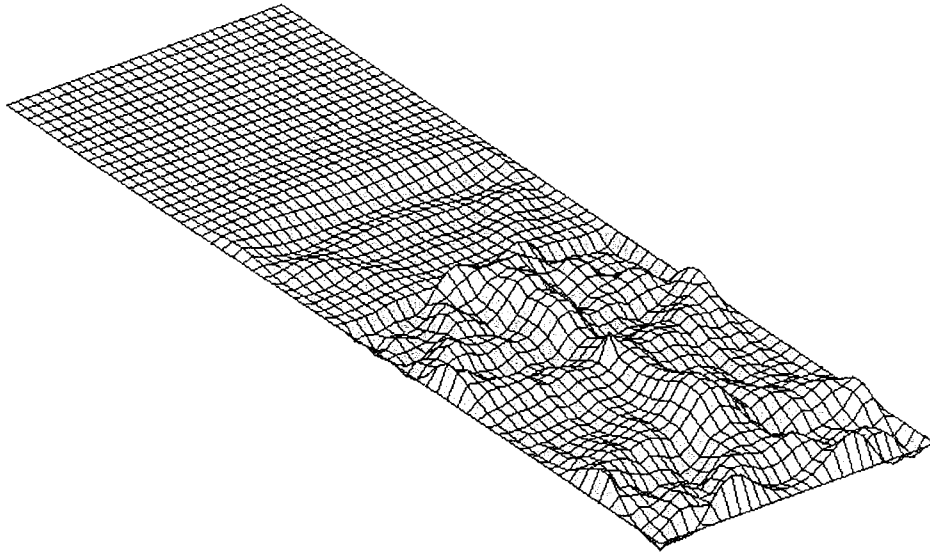


(a)

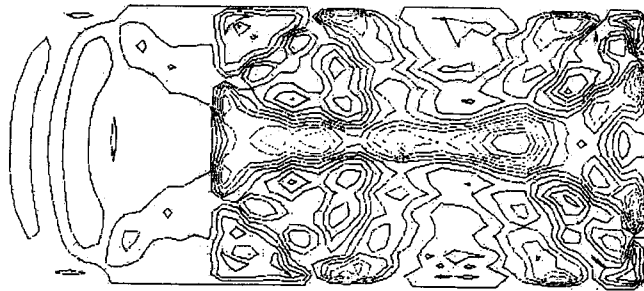


(b)

Fig. 7.13 (a) The  $E_z$  field surface plot and (b) contour plot at time step 200.

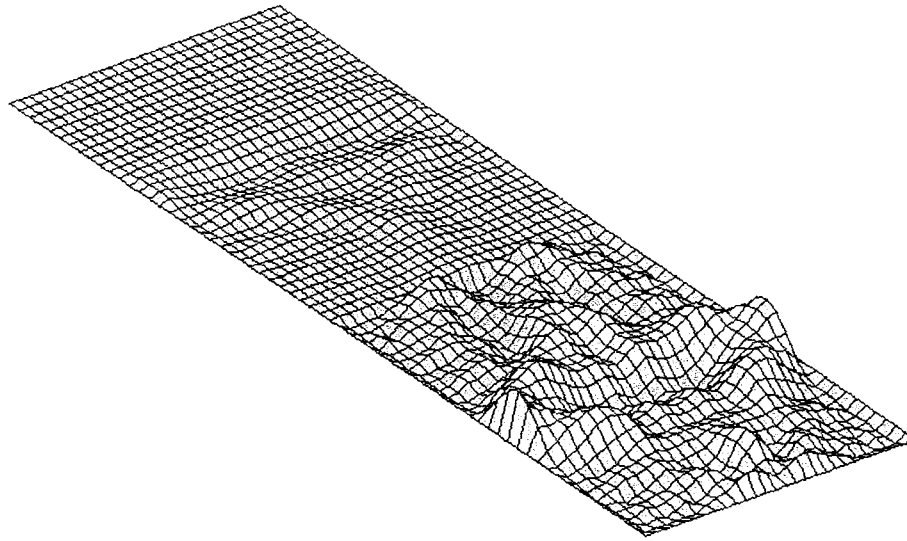


(a)

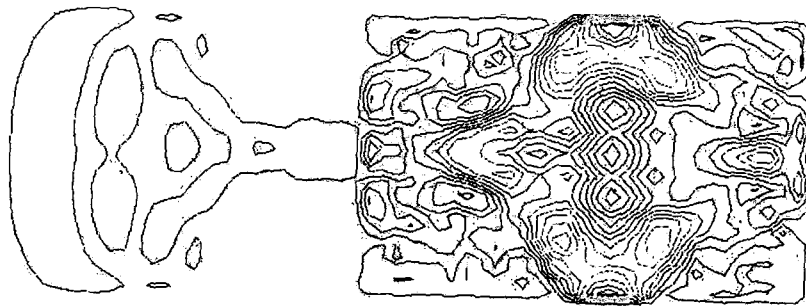


(b)

Fig. 7.14 (a) The  $E_z$  field surface plot and (b) contour plot at time step 250.

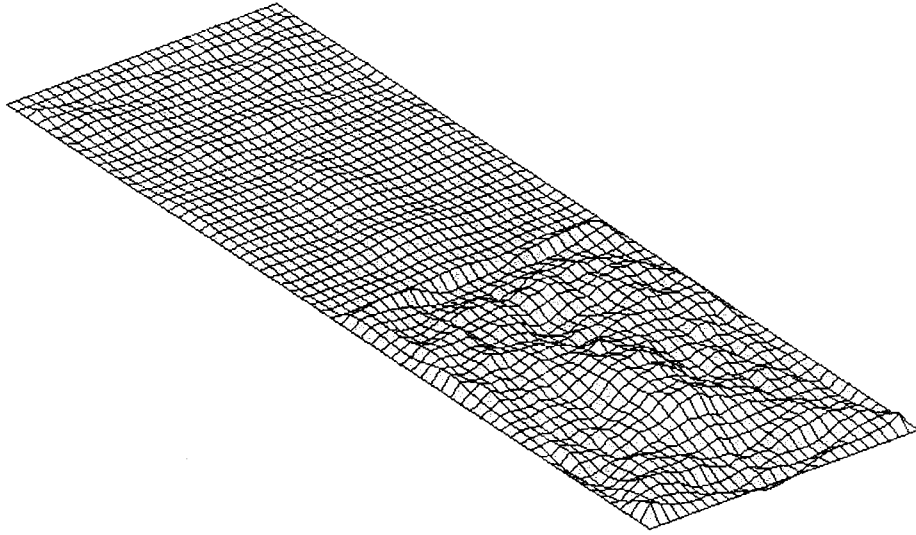


(a)

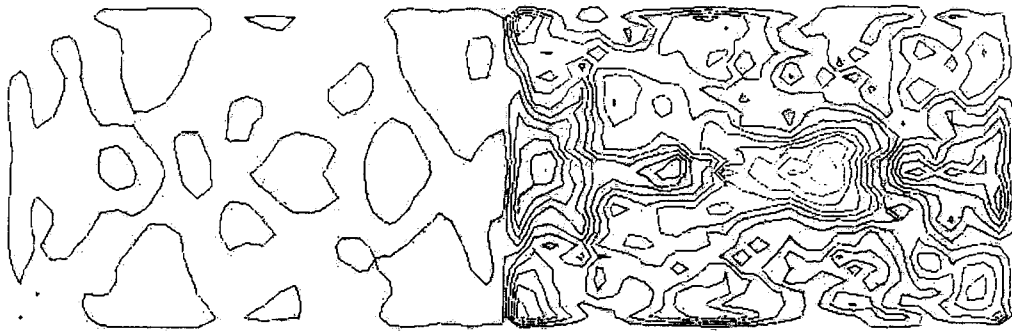


(b)

Fig. 7.15 (a) The  $E_z$  field surface plot and (b) contour plot at time step 300.



(a)



(b)

Fig. 7.16 (a) The  $E_z$  field surface plot and (b) contour plot at time step 500.

## Chapter 8

### Conclusions

The prism-gridded FEM is proposed and has been successfully incorporated with conventional FDTD method to deal with planar circuits with transversely curved boundary. This approach has been applied to characterize problems such as vias in packaging interconnections and transition between different transmission lines. In essence, it can also be generalized to deal with various structures such as planar circuits, waveguides with step transition and whatever can be longitudinally divided into several building layers. Owing to the flexibility provided by FEM, the present scheme can easily model structures with objects of arbitrary aspect ratio in shape which is hard of access by conventional FDTD.

The additional computational load of the present method in comparison with the conventional FDTD method has been analyzed both theoretically and numerically. In theory, the overhead of FEM in memory and CPU time requirement is inversely proportional to the division number per direction  $N_{\Delta}$  and thus negligible for fine mesh. In practice, simulation results depicts that the present method remains very efficient with computational overhead smaller 15% for most applications.

The hybrid FE/FDTD method suffers from the late-time instability. The mechanism of this instability is found to be the field imbalance in FEM and FDTD region due to the inconsistent bases for FEM and FDTD methods. A novel finite element basis to circumvent this problem is therefore proposed. It is the perfect match in not only the mesh but also the field basis that totally eliminate the numerical instability due to the interface of the two time-domain analyses. The basis has been successfully applied to deal with two-dimensional scattering problems of dielectric cylinders, and its generalization to three-dimensional problems deserves further study.

The two-dimensional FDTD method is also applied in analyzing the electromagnetic problems of high-speed circuit. With a newly derived thin-slot formalism, the fields around the slot are analytically solved to prevent the increase of FDTD mesh due to the thin structure. The efficiency and the practicability of FDTD method can then be improved. The method has been applied to transmission lines involving thin slots, and the numerical results are compared with those by traditional FDTD method and other thin-slot formalisms. It is verified that the proposed method is easy to implement, numerically efficient and accurate. Although only the case of

thin-slot structures is studied, the same idea can be applied to other thin structures analyzed by FDTD method.

A new modeling approach is also proposed in the application of signal integrity issues in nowadays' PCB. In a simple multi-layered structure with split power plane, the signal line and slot are analyzed by the corresponding telegrapher's equations, and the region between the power plane and ground plane is analyzed by two-dimensional FDTD method. The ground bounce due to the coupling from a single slot is simulated and measured. Both show that the induced electromagnetic wave may result in significant coupled noise on distant quiet signal and may not be ignored.

To analyze the signal integrity issues between isolation islands due to the radiation coupling from the edges, a novel method that combines two-dimensional FDTD and time-domain integral equation is proposed. Favorable agreement between numerical and experimental results has demonstrated the accuracy of this method. Although the coupled noise caused by radiation is less than 2%, the effects may severely deteriorate the signal integrity of other islands at some resonant frequencies.

Finally, the visualization of electromagnetic fields distribution is demonstrated. With the help of either web-based visualization environment or the commercial visualization tool, numerical results, such as the fields distribution, can be graphically present to the user. The visualization system can provide researchers with easier and more intuitive way in understanding the complicated phenomena of the electromagnetic wave.

## Reference

- [1] K. S. Yee, "Numerical solution of initial boundary value problems in isotropic media," *IEEE Trans. Antennas Propagat.*, vol. 14, pp. 302-307, May 1966.
- [2] A. Taflove, *Computational Electrodynamics: The Finite-Difference Time-Domain Method*, MA: Artech House Inc., 1995.
- [3] R. Holland, "Finite-difference solutions of Maxwell's equations in generalized nonorthogonal coordinates," *IEEE Trans. Nucl. Sci.*, vol. 30, pp. 4589-4591, Dec. 1983.
- [4] T. G. Jurgens, A. Taflove, K. Umashanker, and T. G. Moore, "Finite-difference time-domain modeling of curved surfaces," *IEEE Trans. Antennas Propagat.*, vol. 40, pp. 357-366, Apr. 1992.
- [5] C. H. Thng and R. C. Booton, "Edge-element time-domain method for solving Maxwell's equations," *IEEE MTT-S Int. Microwave Symp. Dig.*, June 1994, pp. 693-696.
- [6] S. S. Zivanovic, K. S. Yee, and K. K. Mei, "A subgridding method for the time-domain finite-difference method to solve Maxwell's equations," *IEEE Trans. Microwave Theory Tech.*, vol. 39, pp. 471-479, Mar. 1991.
- [7] D. T. Prescott and N. V. Shuley, "A method for incorporating different sized cells into the finite-difference time-domain analysis technique," *IEEE Microwave Guided Wave Lett.*, vol. 2, pp. 434-436, Nov. 1992.
- [8] K. S. Yee, J. S. Chen, and A. H. Chang, "Conformal finite-difference time-domain (FD-TD) with overlapping grid," *IEEE Trans. Antennas Propagat.*, vol. 40, pp. 1068-1075, Sept. 1992.
- [9] R. B. Wu and T. Itoh, "Hybridizing FD-TD analysis with unconditionally stable FEM for objects of curved boundary," *IEEE MTT-S Int. Microwave Symp. Dig.*, May 1995, pp. 833-836.
- [10] R. B. Wu and T. Itoh, "Hybrid finite-difference time-domain modeling of curved surfaces using tetrahedral edge elements," *IEEE Trans. Antennas Propagat.*, vol. 45, pp. 1302-1309, Aug. 1997.
- [11] S. Gedney and F. Lansing, "Full wave analysis of printed microstrip devices using a generalized Yee algorithm," *IEEE AP-S Int. Symp. Dig.*, June 1993, pp. 1179-1182.
- [12] D. J. Riley and C. D. Turner, "VOLMAX: A solid-model based, transient volumetric Maxwell solver using hybrid grids," *IEEE Antennas Propagat. Mag.*, vol. 39, pp. 20-33, Feb. 1997.

- [13] S. Palaniswamy, W. F. Hall, and V. Shankar, "Numerical solution to Maxwell's equations in the time domain on nonuniform grids," *Radio Sci.*, vol. 31, pp. 905-912, July/Aug. 1996.
- [14] J. S. Shang and R. M. Fithen, "A comparative study of characteristic-based algorithms for the Maxwell equations," *J. Comput. Phys.*, vol. 125, pp. 378-394, 1996.
- [15] J. Gilbert and R. Holland, "Implementation of the thin-slot formalism in the finite-difference EMP code *THREDII*," *IEEE Trans. Nucl. Sci.*, vol. NS-28, pp. 4269-4274, Dec. 1981.
- [16] A. Taflove, K. R. Umashankar, B. Berker, F. Harfoush, and K. S. Yee, "Detailed FD-TD analysis of electromagnetic fields penetrating narrow slots and lapped joints in thick conducting screens," *IEEE Trans. Antennas Propagat.*, vol. 36, pp. 247-257, Feb. 1988.
- [17] D. J. Riley and C. D. Turner, "Hybrid thin-slot algorithm for the analysis of narrow apertures in finite-difference time-domain calculations," *IEEE Trans. Antennas Propagat.*, vol. 38, pp. 1943-1950, Dec. 1990.
- [18] B. Z. Wang, "Enhanced thin-slot formalism for the FDTD analysis of thin-slot penetration," *IEEE Microwave Guided Wave Lett.*, vol. 5, pp. 142-143, May 1995.
- [19] J. Fan, Y. Ren, J. Chen, D. M. Hockanson, H. Shi, J. L. Drewniak, T. H. Hubing, T. P. V. Doren, and E. DuBroff, "RF isolation using power islands in dc power bus design," *IEEE Int. Symp. Electromagn. Compat.*, 1999, pp. 838-843.
- [20] H. J. Liaw and H. Merkelo, "Signal integrity issues at split ground and power planes," *Proceedings of 46<sup>th</sup> IEEE Electronic Comp. Technol. Conf.*, 1996, pp. 752-755.
- [21] H. J. Liaw and H. Merkelo, "Crossing the planes at high speed," *IEEE Circuit & Devices Mag.*, vol. 13, pp. 22-26, Nov. 1997.
- [22] C. Schuster and W. Fichtner, "Parasitic modes on printed circuit boards and their effects on EMC and signal integrity," *IEEE Trans. Electromagn. Compat.*, vol. 43, pp. 416-425, Nov. 2001.
- [23] D. D. Zutter, "The FDTD-method for EMC-problems with application to electrostatic discharge and delta-I noise calculations", *IEEE Int. Symp. Electromagn. Compat.*, 1997, pp. 226-230.
- [24] S. Van Den Berghe, F. Olyslager, D. De Zutter, J. De Moerloose, and W. Temmerman, "Study of the ground bounce caused by power plane resonance," *IEEE Trans. Electromagnet. Compat.*, vol. 40, pp. 111-119, May 1998.



- [25] D. J. Riley and C. D. Turner, "Interfacing unstructured tetrahedron grids to structured-grid FDTD," *IEEE Microwave Guided Wave Lett.*, vol. 5, pp. 284-286, Sept. 1995.
- [26] P. Mezzanotte, L. Roselli, and R. Sorrentino, "A simple way to model curved metal boundaries in FDTD algorithm avoiding staircase approximation," *IEEE Microwave Guided Wave Lett.*, vol. 5, pp. 267-279, Aug. 1995.
- [27] W. K. Gwarek, "Analysis of an arbitrarily-shaped planar circuit- a time-domain approach," *IEEE Trans. Microwave Theory Tech.*, vol. 33, pp. 1067-1072, Oct. 1985.
- [28] A. C. Cangellaris, C. C. Lin, and K. K. Mei, "Point-matched time domain finite element methods for electromagnetic radiation and scattering," *IEEE Trans. Antennas Propagat.*, vol. 35, pp. 1160-1173, Oct. 1987.
- [29] M. Righi, J. L. Herring, and W. J. R. hoefer, "Efficient hybrid TLM/mode-matching analysis of packaged components," *IEEE Trans. Microwave Theory Tech.*, vol. 45, pp. 1715-1724, Oct. 1997.
- [30] R. B. Wu, "A wideband waveguide transition design with modified dielectric transformer using edge-based tetrahedral finite element analysis," *IEEE Trans. Microwave Theory Tech.*, vol. 44, pp. 1024-1031, July 1996.
- [31] J. Jin, *The Finite Element Method in Electromagnetics*, New York: John Wiley & Sons, 1993, sec. 2.1, sec. 4.3, sec. 8.1.
- [32] D. Koh, H. B. Lee, and T. Itoh, "A hybrid full-wave analysis of via hole grounds using finite difference and finite element time domain methods," *IEEE MTT-S Int. Microwave Symp. Dig.*, June 1997, pp. 89-92.
- [33] K. J. Bathe and E. L. Wilson, *Numerical Methods in Finite Element Analysis*, N. J.: Prentice-Hall, 1976, sec. 7.2.4.
- [34] R. J. Collins, "Bandwidth reduction by automatic renumbering," *Int. J. Num. Meth. Engr.*, vol. 6, pp. 345-356, 1973.
- [35] G. Mur, "Absorbing boundary conditions for the finite-difference approximation of the time-domain electromagnetic-field equations," *IEEE Trans, Electromagn. Compat.*, vol. 23, pp. 377-382, Nov. 1981.
- [36] K. K. Mei and J. Fang, "Superabsorption- a method to improve absorbing boundary conditions," *IEEE Trans. Antennas Propagat.*, vol. 40, pp. 1001-1010, Sept. 1992.
- [37] R. Sorrentino, F. Alessandri, M. Mongiardo, G. Avitabile, and L. Roselli, "Full-wave modeling of via hole grounds in microstrip by three-dimensional mode matching technique," *IEEE Trans. Microwave Theory Tech.*, vol. 40, pp. 2228-2234, Dec. 1992.

- [38] S. Maeda, T. Kashiwa, and I. Fukai, "Full wave analysis of propagation characteristics of a through hole using the finite-difference time-domain method," *IEEE Trans. Microwave Theory Tech.*, vol. 39, pp. 2154-2159, Dec. 1991.
- [39] S. G. Hsu and R. B. Wu, "Full wave characterization of a through hole via in multi-layered packaging," *IEEE Trans. Microwave Theory Tech.*, vol. 43, pp. 1073-1081, May 1995.
- [40] H. K. Chiou, C. Y. Chang, and H. H. Lin, "Balun design for uniplanar broad band double balanced mixer," *Electron. Lett.*, vol. 31, pp. 211-212, Nov. 1995.
- [41] S. G. Mao, C. T. Hwang, R. B. Wu, and C. H. Chen, "Analysis of coplanar waveguide-to-coplanar stripline transitions," *IEEE Trans. Microwave Theory Tech.*, vol. 48, pp. 23-29, Jan. 2000.
- [42] C. T. Hwang and R. B. Wu, "Treating late time instability of hybrid finite element/finite difference time domain method," *IEEE Trans. Antennas Propagat.*, vol. 47, pp. 227-232, Feb. 1999.
- [43] K. M. Krishnaiah and C. J. Railton, "Passive equivalent circuit of FDTD: An application to subgridding," *Electron. Lett.*, vol. 33, pp. 1277-1278, July 1997.
- [44] C. J. Railton, I. J. Craddock, and J. B. Schneider, "Improved locally distorted CPFDTD algorithm with provable stability," *Electron. Lett.*, vol. 31, pp. 1586-1587, 1995.
- [45] C. D. Tuner and L. D. Bacon, "Evaluation of a thin-slot formalism for finite-difference time-domain electromagnetic codes," *IEEE Trans. Electromagn. Compat.*, vol. 30, pp. 523-528, Nov. 1988.
- [46] K. P. Ma, Min Li, J. L. Drewniak, T. H. Hubing, and T. P. Van Doren, "Comparison of FDTD algorithms, for subcellular modeling of slots in shielding enclosures," *IEEE Trans. Electromagn. Compat.*, vol. 39, pp. 147-155, May 1997.
- [47] W. R. Smythe, *Static and Dynamic Electricity*, 3<sup>rd</sup> ed., McGraw-Hill, 1968, chap. 5.
- [48] L. K. Warne and K.C. Chen, "Equivalent antenna radius for narrow slot apertures having depth," *IEEE Trans. Antennas Propagat.*, vol. 37, pp. 824-834, July 1989.
- [49] A. P. Zhao and A.V. Räisänen, "Application of a simple and efficient source excitation technique to the FDTD analysis of waveguide and microstrip circuits," *IEEE Trans. Microwave Theory Tech.*, vol. 44, pp. 1535-1538, Sept. 1996.
- [50] W. Cui, J. Fan, H. Shi, and J. L. Drewniak, "DC power bus noise isolation with power islands," *IEEE Int. Symp. Electromagn. Compat.*, 2001, pp. 899-903.
- [51] H. Shi, J. Fan, J. L. Drewniak, T. H. Hubing, and T. P. Van Doren, "Modeling multi-layered PCB power-bus design using an MPIE based circuit extraction technique," *IEEE Int. Symp. Electromagn. Compat.*, 1998, pp. 147-151.

- [52] Y. Chen, Z. Wu, A. Agrawal, Y. Liu, and J. Fang, "Modeling of delta-I noise in digital electronic packaging," 1994 *IEEE Multi-Chip Module Conf.*, pp. 126-131, Santa Cruz, CA, March 15-17.
- [53] W. T. Weeks, "Calculation of coefficients of capacitance of multi-conductor transmission lines in the presence of a dielectric interface," *IEEE Trans. Microwave Theory Tech.*, vol. 18, pp. 35-43, Jan. 1970.
- [54] Z. Wu, Y. Chen, and J. Fang, "Modeling and simulation of integral decoupling capacitors in single and multichip module electronics packaging," 1994 *IEEE Multi-Chip Module Conf.*, pp. 945-948, Santa Cruz, CA, March 15-17.
- [55] A. E. Ruehli and A. C. Cangellaris, "Application of the partial element equivalent circuit (PEEC) method to realistic printed circuit board problem," *IEEE Int. Symp. Electromagn. Compat.*, 1998, pp. 182-187.
- [56] B. Archambeault and A. E. Ruehli, "Analysis of power/ground-plane EMI decoupling performance using the partial-element equivalent circuit technique," *IEEE Trans. Electromagn. Compat.*, vol. 43, pp. 437-445, Nov. 2001.
- [57] S. W. Leung, L. Wang, and C. M. Ip, "Modeling of the ground bounce effect on PCBs for high speed digital circuits," *IEEE Int. Symp. Electromagn. Compat.*, 1999, pp. 110-115.
- [58] S. H. Chen, *User's Guide for the Internet-Based PSE*, National Center for High-Performance Computing, 1999.
- [59] *MATFOR Getting Started Guide*, <http://www.ancad.com>.

## Appendix A: Publications Supported under this Project

- C. T. Hwang and R. B. Wu, "Treating late time instability of hybrid finite element/finite difference time domain method," *IEEE Transactions on Antennas and Propagation*, vol. 47, pp. 227-232, Feb. 1999.
- S. G. Mao, C. T. Hwang, R. B. Wu, and C. H. Chen, "Analysis of coplanar waveguide-to-coplanar stripline transitions," *IEEE Transactions on Microwave Theory and Techniques*, vol. 48, pp. 23-29, Jan. 2000.
- C. T. Hwang, S. G. Mao, R. B. Wu, and C. H. Chen, "Partially prism-gridded FDTD analysis for layered structures of transversely curved boundary," *IEEE Transactions on Microwave Theory and Techniques*, Vol. 48, pp. 339-346, March 2000
- S. M. Lin and R. B. Wu, "Composite effects of reflections and ground bounce for signal line through a split power plane," *IEEE 10<sup>th</sup> Topical Meeting on Electrical Performance of Electronic Packaging*, pp. 89-92, Cambridge, Massachusetts, U.S.A., Oct. 2001.
- S. M. Lin and R. B. Wu, "Composite effects of reflections and ground bounce for signal vias in multiplayer environment," *2001 Asia Pacific Microwave Conference*, pp. 1127- 1130, Taipei, Taiwan, Dec. 2001.
- C. T. Wu, G. H. Shiue, S. M. Lin, and R. B. Wu, "Composite effects of reflections and ground bounce for signal line through a split power plane," *IEEE Transactions on Advanced Packaging*, Vol.25, pp. 297-301, May 2002.
- C. T. Wu and R. B. Wu, "Two-dimensional finite-difference time-domain method combined with open boundary for signal integrity issues between isolation islands," *IEEE 11<sup>th</sup> Topical Meeting on Electrical Performance of Electronic Packaging*, pp. 283-286, Monterey, CA, Oct. 2002.
- C. T. Wu, Y. H. Pang, and R. B. Wu, "An improved formalism for FDTD analysis of thin-slot problems by conformal mapping technique," to appear on *IEEE Transactions on Antennas and Propagation*, Aug. 2003.

# Two-Dimensional Finite-Difference Time-Domain Method Combined with Open Boundary for Signal Integrity Issues between Isolation Islands

Chun-Te Wu and Ruey-Beei Wu

Dept. of Electrical Engineering and Graduate Institute of Communication Engineering,  
National Taiwan University, Taipei, Taiwan, 10617, R.O.C.  
Tel: +886-2-23635251 x 340 Fax: +886-2-23638247  
E-mail: rbwu@ew.ee.ntu.edu.tw

## Abstract

*A novel method is proposed to take into account radiation effects due to the open boundary of PCB on ground bounce between isolated power/ground planes by the 2D-FDTD method hybridized with integral equation formulation for the exterior field. An efficient simulation procedure is established by casting equivalent inductances and capacitances with phase retardation into 2D-FDTD. Simulation results for the radiation effects due to open boundary or among isolated power/ground planes are presented and validated by measured data.*

## 1 Introduction

Isolated power or ground areas, so called voltage "islands", are commonly used in PCB to distribute multiple power sources or separate noisy circuit areas. Conventionally, investigation of signal integrity issues at split ground and power planes should be resorted to three-dimensional FDTD method [1]. A lot of computer memory and CPU time is required to perform the simulation. In a PCB, the electric field between ground/power planes is uniform in the longitudinal direction except near the edge due to the fringing effects. A more efficient approach should be based on 2D-FDTD. However, such an approach usually puts perfect magnetic conductor (PMC) on the edge and neglects the radiation effects. A radiation boundary condition suitable for 2D-FDTD has never been proposed before in the literature.

In this paper, a new radiation boundary suitable for 2D-FDTD is developed to solve the signal integrity issues between isolation islands. Through comparison between simulated and measured data, it has been proven to be accurate and efficient.

## 2 Theory

Consider a patch shown in Fig. 1 in which the ground plane is infinite. The field outside the patch can be expressed by putting equivalent magnetic source  $\vec{M} = \vec{E} \times \hat{n}$  along the edge of the patch. If the ground plane is large enough to apply image theory, the ground plane can be replaced by doubling the magnetic current, which is illustrated in Fig. 2. The scattering magnetic field outside the patch due to the magnetic current can be expressed as

$$\vec{H}^s = \frac{\nabla \nabla \cdot \vec{F} + k^2 \vec{F}}{j\omega\mu} \quad (1)$$

$$\vec{F} = \int_{\Gamma} \frac{e^{-jkR}}{4\pi R} 2\vec{M}(\vec{r}') d\vec{r}' \quad (2)$$

where  $R$  is the distance between field and source points,  $k$  is propagation constant,  $\vec{F}$  is magnetic vector potential, and  $\Gamma$  presents the surface along the edge.

Assume that  $\vec{M}(\vec{r}')$  is modeled by roof-top bases, as illustrated in Fig. 3. The magnetic currents can be expressed as

$$\vec{M}(\vec{r}') = \sum_j V_j \vec{B}_j(\vec{r}') \quad (3)$$

---

This work was jointly supported under the Grants 89-E-Fa06-2 by Ministry of Education, and NSC 89-2213 E002-197 by National Science council, Republic of China.

where  $\bar{B}_j(\bar{r}')$  is the roof-top basis on the area of cells  $Ce_{j-\frac{1}{2}}$  and  $Ce_{j+\frac{1}{2}}$  as illustrated in Fig. 4, and the corresponding unknown coefficient  $V_j$  denotes the voltage at the branch  $S_j$ .

After some deduction of mathematics, an equivalent circuit model can be obtained. Figure 5 shows the equivalent circuit for updating the voltage at branch  $S_i$ . The equivalent circuit equations for this method is given by

$$(C_{FDTD} + C_H) \frac{dV_i}{dt} = I_i^{inc} - I_i^+ + I_i^- - I_i^g - I_{i,i+1} + I_{i-1,i} \quad (5)$$

where  $C_H = \varepsilon \int_{\Gamma_i} \int_{\Gamma_j} \frac{e^{-jkR}}{2\pi R} \bar{B}_i(\bar{r}') \cdot \bar{B}_j(\bar{r}') d\bar{r}' d\bar{r}$ , and

$$I_i^+ = \sum_{j \neq i} I_{i+\frac{1}{2}, j+\frac{1}{2}} = \sum_{j \neq i} \frac{L_{i+\frac{1}{2}, j+\frac{1}{2}}^{-1}}{L_{j-\frac{1}{2}, j-\frac{1}{2}}^{-1}} I_{j,j+1} e^{j(\frac{|\bar{s}_{i+\frac{1}{2}} - \bar{s}_{j+\frac{1}{2}}|}{c})}$$

$$I_i^- = \sum_{j \neq i} I_{i-\frac{1}{2}, j-\frac{1}{2}} = \sum_{j \neq i} \frac{L_{i-\frac{1}{2}, j-\frac{1}{2}}^{-1}}{L_{j-\frac{1}{2}, j-\frac{1}{2}}^{-1}} I_{j-1,j} e^{j(\frac{|\bar{s}_{i-\frac{1}{2}} - \bar{s}_{j-\frac{1}{2}}|}{c})}$$

$$I_i^g = \sum_{j \neq i} j\omega C_{ji} V_j = \sum_{j \neq i} C_{ji} \frac{d}{dt} V_j e^{j(\frac{|\bar{s}_i - \bar{s}_j|}{c})}$$

The governing equation for  $I_{i,i+1}$  is

$$L_{i+\frac{1}{2}, i+\frac{1}{2}}^{-1} \frac{d}{dt} I_{i,i+1} = V_i - V_{i+1} \quad (6)$$

where  $L_{i+\frac{1}{2}, i+\frac{1}{2}}^{-1}$  is the average of  $\frac{e^{-jkR}}{2\pi\mu R}$  over cells  $Ce_{i+\frac{1}{2}}$  and  $Ce_{j+\frac{1}{2}}$ .

The physical meaning of coupling capacitance  $C_{ji}$  is the capacitive coupling from branch voltage  $V_j$  to branch voltage  $V_i$ ,  $C_H$  is the self-capacitance for the branch  $V_i$ , and  $L_{i+\frac{1}{2}, i+\frac{1}{2}}^{-1}$  is the self-inductance at cell  $Ce_{i+\frac{1}{2}}$ . In time domain, the effects of  $C_{ji}$  and  $L_{i+\frac{1}{2}, i+\frac{1}{2}}^{-1}$  happens at  $\frac{|\bar{s}_i - \bar{s}_j|}{c\Delta t}$  time steps later, due to the phase retardation term  $e^{jkR}$ , where  $\bar{s}_i$  means the position vector at the center of  $S_i$ .

### 3 Simulation Results

A structure of two isolation power islands is fabricated to investigate the coupling between islands. As in Fig. 6, the separation of the two isolation is 1mm, the thickness of substrate is 1.2mm, and the dielectric constant of substrate  $\varepsilon_r = 4.2$ . The whole structure is symmetric. There are no vias or transmission lines between these two patches. The noise, if generated, could be contributed to the other island.

In the experiment, a ramped step pulse of about amplitude 0.25 volts and rise time 100ps is used as the excitation on port 1. The TDR and TDT signals at point 1 and 2, respectively, are measured by Tektronix 11801C. The measured input waveform is used as the excitation signal in numerical simulation. Figures 7 shows the results at TDR port by simulation and experiment. In the case of PMC boundary, the RC time constant is found to be approximate 1162ps, if the capacitance is calculated from

patch area  $A$  and substrate thickness  $d$  by parallel-plate formula  $C = \varepsilon \frac{A}{d} \approx 23.24 pF$ , and the resistance

$R$  is internal resistor of 50 ohm. The RC time constant is larger in the present method, since the fringing effect enlarges the effective area of patch. It is noted from the figure that the RC time constant of

experiment is even longer due to the loss of measurement system and PCB.

As for TDT shown in Fig. 8, the coupling noise level at port 2 is measured to be 4mV as compared to the simulated value of 5.3mV by the present method. In other words, the generated coupled noise by isolation islands in the present case may achieve about 2% of the input level. The over-estimation in the simulated level can be contributed to the negligence of substrate and conductor loss.

Figure 9 shows the power spectrum density of the measured and simulated waveforms. Due to the position of excitation, the first two peaks should occur at  $TM_{10}$  at 2.375GHz, and  $TM_{20}$  at 4.714GHz. The agreement between measurement and simulation demonstrates the accuracy of the present method.

#### 4 Conclusions

A new methodology is presented in this paper to simulate the signal integrity issues between isolation islands due to radiation coupling. The methodology can be cast into 2D-FDTD to analyze the radiation problems of PCB. Numerical and experimental results have both demonstrated the accuracy of this method. Although the coupled noise caused by radiation is less than 2%, the effects may severely deteriorate the signal integrity of other islands at some resonant frequencies.

#### 5 References

- [1] H. J. Liaw and H. Merkelo, "Signal integrity issues at split ground and power planes," *Proceedings of 46<sup>th</sup> IEEE Electronic Components and Technology Conference*, 1996, pp. 752 –755.

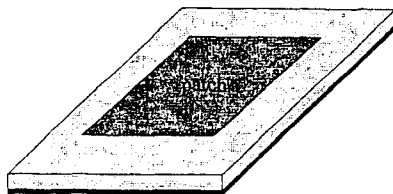


Figure 1 A patch on a large substrate and ground plane.

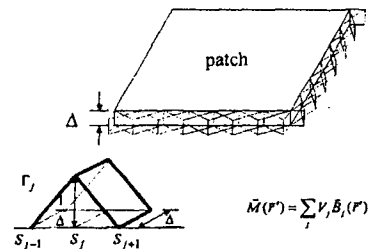


Figure 3 Using roof-top bases to expand magnetic currents.

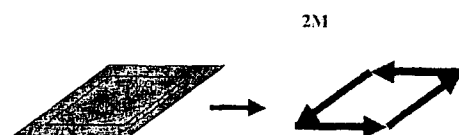


Figure 2 Applying equivalent principle and image theory to the boundary of edges

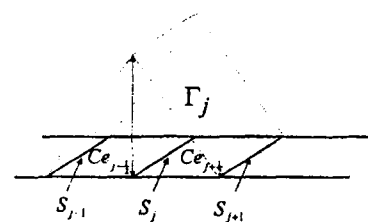


Figure 4 An illustration to explain the branch  $Br_j$  and cell  $Ce_{j+1/2}$ .

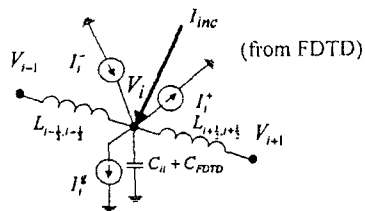


Figure 5 Equivalent circuit for updating the voltage at branch  $Br_i$ .

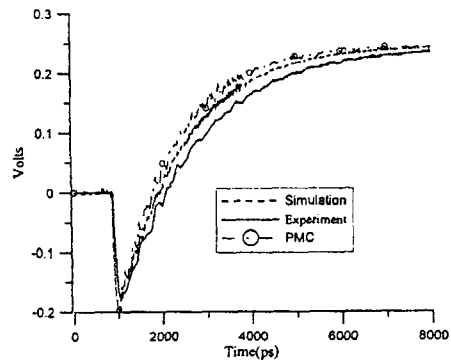


Figure 7 Measured and simulated waveforms of the TDR signal on port 1.

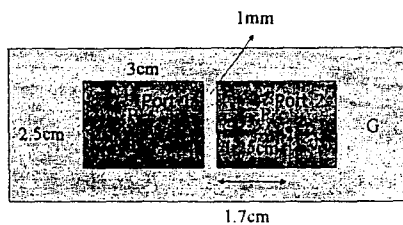


Figure 6 A test PCB of isolation power plane used for experiment and simulation.

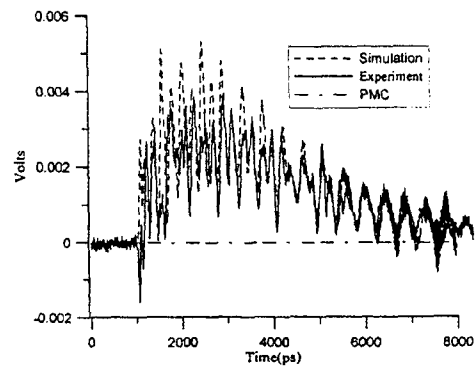


Figure 8 Measured and simulated waveforms of the TDT signal on port 2.

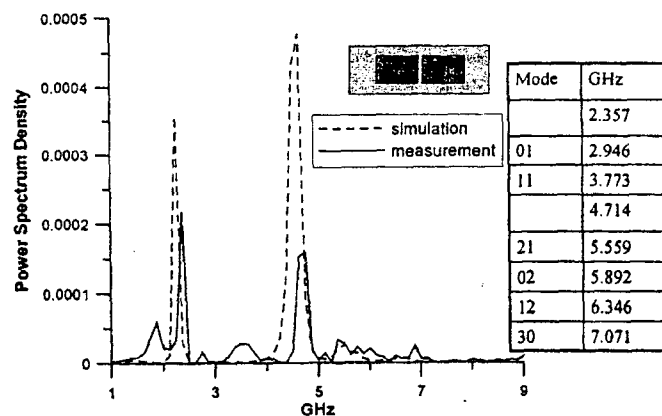


Figure 9 Power spectrum density of TDT for simulated and measured



# Composite Effects of Reflections and Ground Bounce for Signal Line through a Split Power Plane

Sheng-Mou Lin and Ruey-Beei Wu

Dept. of Electrical Engineering and Graduate Institute of Communication Engineering,  
National Taiwan University, Taipei, Taiwan, 10617, R.O.C.  
Tel: +886-2-23635251 x 340 Fax: +886-2-23638247  
E-mail: rbwu@ew.ee.ntu.edu.tw

## Abstract

*The signal propagating along a microstrip line over a slot on the power plane will suffer from composite effects of reflected noise by a discontinuity in signal return path and ground bounce between power/ground planes. A new equivalent circuit model is proposed and simulations are performed for a three-layer structure to characterize ground bounce coupling.*

## 1 Introduction

In a multi-layer printed circuit board (PCB) or multi-chip module (MCM), it is common practice to cut a slot in ground or power plane. For example, cutting a power plane into several areas provides multiple power distribution. Another is an isolated power or ground plane area, called island, to isolate a noisy or sensitive circuit from other circuits. However, signal lines have to cross the slots in order to communicate between different areas. Hence incurred are two major signal integrity concerns; the reflection due to the discontinuity in signal return path and the ground bounce which is the voltage fluctuations between power and ground planes.

Traditionally considered to be mainly due to the electric current along vias, the ground bounce can be caused as well by the equivalent magnetic current flowing through the slot on the power or ground planes. As ground bounce noise generated either by other vias or slots in power/ground planes propagate across the slots, it will in turn induce noise voltage on slot and then couple into signal lines. To accurately model the propagation characteristics of signal traces over slot, the composite effects of signal reflection and ground bounce must be taken into account in view of the increasing complexity of the routing and the necessity of multiple power distribution.

The isolation of island has been discussed using the three-dimensional finite-difference time-domain (FDTD) method [1], but signal lines are not included and this method need long computation time and large computer memory. In another point of view, the microstrip/slot coupled has been discussed using transmission line model and mode conversion [2], but neglecting the presence of ground bounce between power and ground planes. This paper proposed a new efficient analysis scheme which consists of the two-dimensional FDTD method for the propagation of ground bounce, the transmission line theory for the signal propagation along microstrip and slot line, and especially, an equivalent circuit for the coupling between the ground bounce and signals along the slot. The 2D FDTD and transmission line simulations can be performed separately and linked together at each computation time step. The effects of the slot on signal propagation are thus characterized.

## 2 Theory and Circuit Modelling

Consider a multi-layer structure shown in Fig. 1 in which the power plane is cut with a finite slot. The whole structure can be divided into two parts, region 1: the microstrip line and slotline, and region 2: the parallel plates with a split on one plane. Since the separation between two metal planes is typically much smaller than the wavelength and the size of the planes, the fields between the two metal planes can be assumed to be uniform along the vertical direction. Consequently, the electromagnetic fields between

---

※ This work was jointly supported in part under the Grant 89-E-FA06-2 by Ministry of Education and under the Grant 88-S-32 by AnCad Technology Inc.

two metal planes are two-dimensional and consist of  $E_z$ ,  $H_x$ , and  $H_y$  only. They can be solved by the two-dimensional FDTD method.

Microstrip line and slotline can be modelled as transmission lines. Given the propagation constant and characteristic impedance, they are approximated by equivalent LC ladder circuits and the signal propagation is simulated by telegrapher's equation using central difference discretization. Without loss of generality, assume that the slotline is positioned along  $x = (i_0 + \frac{1}{2})\Delta x$  while the microstrip line is along  $y = j_0\Delta y$ .

At region 1, the equivalent circuit at the cross section of microstrip line and slotline is similar to that described in [2], as shown in Fig. 2, i.e.,

$$\begin{cases} C_{\text{microstrip}} \Delta x \frac{\partial}{\partial t} V_{\text{microstrip}}(i\Delta x, t) = I_{\text{microstrip}}((i - \frac{1}{2})\Delta x, t) - I_{\text{microstrip}}((i + \frac{1}{2})\Delta x, t) \end{cases} \quad (1a)$$

$$\begin{cases} L_{\text{microstrip}} \Delta x \frac{\partial}{\partial t} I_{\text{microstrip}}((i + \frac{1}{2})\Delta x, t) = V_{\text{microstrip}}(i\Delta x, t) - V_{\text{microstrip}}((i + 1)\Delta x, t) - V_{\text{slot}}(j_0\Delta y, t)\delta_{i,i_0} \end{cases} \quad (1b)$$

Under the consideration of ground bounce coupling, the telegrapher's equation for slotline can be written as

$$\begin{cases} C_{\text{slot}} \Delta y \frac{\partial}{\partial t} V_{\text{slot}}(j\Delta y, t) = -H_y((i_0 + \frac{1}{2})\Delta x, j\Delta y, t)\Delta y - I_{\text{slot}}((j + \frac{1}{2})\Delta y, t) + I_{\text{slot}}((j - \frac{1}{2})\Delta y, t) \\ \quad + I_{\text{microstrip}}(i_0\Delta x, t)\delta_{j,j_0} \end{cases} \quad (2a)$$

$$\begin{cases} L_{\text{slot}} \Delta y \frac{\partial}{\partial t} I_{\text{slot}}((j + \frac{1}{2})\Delta y, t) = V_{\text{slot}}(j\Delta y, t) - V_{\text{slot}}((j + 1)\Delta y, t) \end{cases} \quad (2b)$$

Here,  $L_{\text{slot}}$  and  $C_{\text{slot}}$  are the per-unit-length inductance and capacitance of slotline in the presence of power/ground planes,  $I_{\text{slot}}$  and  $V_{\text{slot}}$  are the current and voltage on slotline, and  $H_y$  is the magnetic field in  $y$  direction under slotline in the power/ground planes. Similar definitions hold for  $L_{\text{microstrip}}$ ,  $C_{\text{microstrip}}$ ,  $I_{\text{microstrip}}$ , and  $V_{\text{microstrip}}$ .

At region 2, the FDTD mesh inclusive of slotline is shown in Fig. 3. The voltage on slotline will couple into power/ground plane so that the updating for magnetic field in  $y$  direction must be rewritten as

$$\mu \frac{\partial}{\partial t} H_y((i + \frac{1}{2})\Delta x, j\Delta y, t)\Delta x \cdot d = [E_x((i + 1)\Delta x, j\Delta y, t) - E_x(i\Delta x, j\Delta y, t)]d + V_{\text{slot}}(j\Delta y, t)\delta_{i,i_0} \quad (3)$$

The time marching can be briefly described as follows. The voltages  $V_{\text{microstrip}}$  and  $V_{\text{slot}}$  can be updated from  $I_{\text{microstrip}}$ ,  $I_{\text{slot}}$ , and  $H_y$  by (1a) and (2a). In the next half time step,  $I_{\text{microstrip}}$ ,  $I_{\text{slot}}$ , and  $H_y$  can be updated from  $V_{\text{microstrip}}$ ,  $V_{\text{slot}}$ , and  $E_x$  with the help of (1b), (2b), and (3). Hence, the coupled effects between slotline and power/ground planes is addressed. The composite effects of reflection and ground bounce among the whole structure can be modelled.

### 3 Simulation Results

Take the structure of a 10cm x 10cm PCB shown in Fig. 1 as an example. The heights of signal layer and power/ground planes are 635  $\mu\text{m}$  and 150  $\mu\text{m}$ , respectively, and the dielectric constant is both 9.7. The widths of microstrip line and slotline are 570  $\mu\text{m}$  and 50  $\mu\text{m}$ , respectively, and the length of slotline is 4cm. The signal voltage source is a Gaussian pulse generator in series with an internal resistance of 50ohm. On the other end of the signal line is connected a matched load. The top view of Fig. 1 is shown in Fig. 4.

The voltages at points A and B are monitored and the waveforms are shown in Fig. 5(a), while the voltages at points a, b, and c in Fig 5(b) and the ground bounce beneath slotline in Fig. 5(c). In Fig. 5(b), as the voltage propagates along the slot, it decays continually due to the energy coupling onto power/ground planes. At late time, the ground bounce that reflected by edge couples into slotline and then causes small noise on microstrip line as shown in Fig. 5(a). Now, the separation of power/ground planes is changed to  $300\ \mu\text{m}$  and  $500\ \mu\text{m}$  and voltage at point A are shown in Fig. 6. As the separation increases, energy coupled into power/ground planes will decrease and the noise on microstrip line will increase.

#### 4 Conclusions

In this paper, a new model is proposed to simulate a signal line flowing above a split power or ground plane. Although ground bounce caused by slot coupling is only 5% of input signal, the effects can not be ignored as multi-trace signal flows through the slot simultaneously.

#### References

- [1] Daniel De Zutter, "The FDTD-method for EMC-problems with application to electrostatic discharge and delta-I noise calculations", *IEEE International Symposium on Electromagnetic Compatibility*, 1997, pp. 226–230.
- [2] H. J. Liaw and H. Merkelo, "Signal integrity issues at split ground and power planes," *Proceedings of 46<sup>th</sup> IEEE Electronic Components and Technology Conference*, 1996, pp. 752–755.

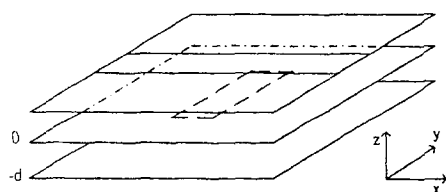


Fig. 1 A simple a multi-layer structure with split power plane.

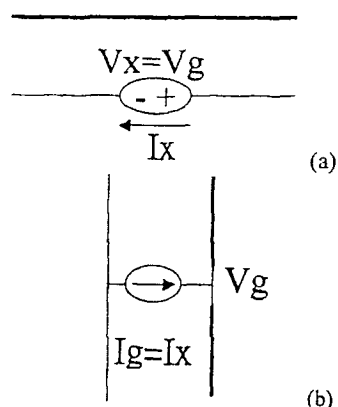


Fig. 2 Equivalent circuit at cross section of microstrip line and slotline.

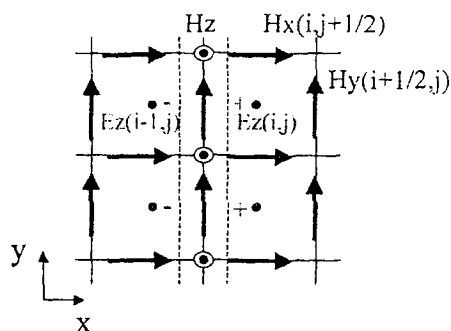


Fig. 3 FDTD mesh inclusive of slotline

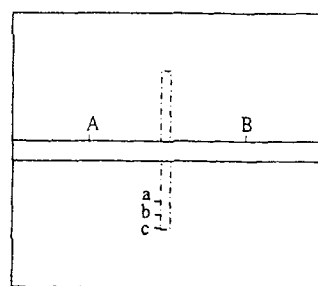
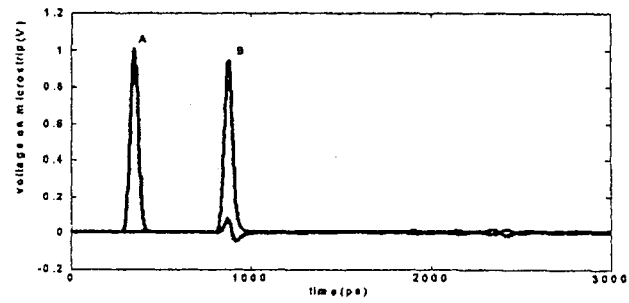
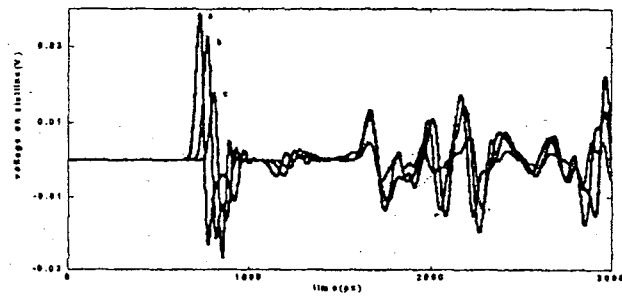


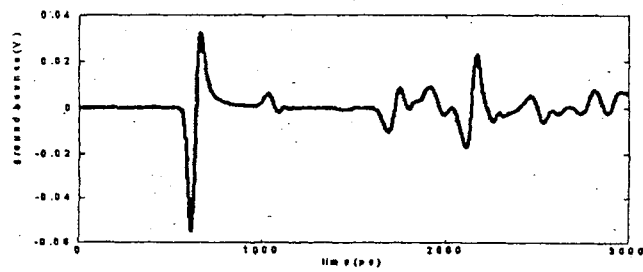
Fig. 4 Top view of Fig. 1



(a)



(b)



(c)

Fig. 5(a) Voltages at A, B, (b) voltages at a, b, c, and (c) ground bounce near slotline

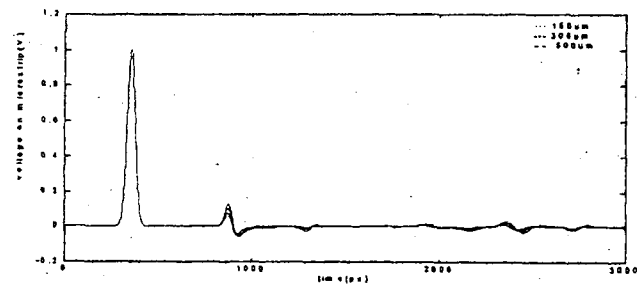


Fig. 6 Comparison of voltage at A with different separation of power/ground planes.